

**NUMERICAL ANALYSIS OF STRAIN LOCALIZATION  
IN CEMENTED AGGREGATE MIXTURES**

**NUMERICAL ANALYSIS OF STRAIN LOCALIZATION  
IN CEMENTED AGGREGATE MIXTURES**

**by**

**GUANGDOU XU, B.Eng, M.Eng**

**A THESIS**

**Submitted to the School of Graduate Studies  
in Partial Fulfilment of the Requirements  
for the Degree  
Doctor of Philosophy**

**McMaster University**

**(c) Copyright by Guangdou Xu, October 1995**

**DOCTOR OF PHILOSOPHY**  
**(Civil Engineering)**

**McMASTER UNIVERSITY**  
**Hamilton, Ontario,**  
**Canada**

**TITLE:**                   **Numerical Analysis of Strain Localization**  
**in Cemented Aggregate Mixtures**

**AUTHOR:**               **Guangdou Xu**  
**B. Eng. (Hohai University, Nanjing, P.R. China)**  
**M. Eng. (Hohai University, Nanjing, P.R. China)**

**SUPERVISORS:**       **Professors S. Pietruszczak and F.M. Mirza**

**NUMBER OF PAGES:**   **xvii, 158**

## ABSTRACT

This thesis deals with the numerical analysis of strain localization in cemented aggregate mixtures. The main objective is to develop a framework for describing localization phenomenon and to implement it in a finite element algorithm. An attempt is also made to establish a formulation for the description of the localized deformation in saturated cemented materials.

The proposed framework combines a plasticity formulation (for homogeneous deformation), bifurcation criterion and homogenization technique (for localized deformation). The formulation of the homogenization technique is derived by estimating the average mechanical properties of a medium intercepted by the strain localization zone (shear band). The mechanical response of the homogenized system depends on the properties of the constituents (matrix and interface) and the respective volume fractions. The constitutive model for the interface is established by incorporating the degradation of both asperities orientation and cohesion.

The implementation of the proposed framework in a finite element code requires an appropriate definition of an internal length parameter as well as a proper integration procedure and solution technique. These aspects are covered in the second part of this thesis. A number of numerical examples are provided

for illustrating the performance of the proposed formulation. First, a series of problems involving compression-shear as a predominant failure mode are analyzed. The emphasis is placed on studies with regard to mesh-sensitivity and the influence of boundary constraints. Subsequently, the problems involving tension-shear fracture mode are studied. These include the analysis of notched specimens under tension and three-point bending. The predicted trends are, in general, consistent with experimental observation.

The mathematical description of localized deformation in saturated cemented materials is also presented. The onset of localization results in the generation of an excess pore pressure gradient in the constituents (matrix and interface). An appropriate formulation for the description of deformation coupled with pore fluid diffusion is proposed. This coupling effect is studied through the analysis of three limited cases, involving: exchange of fluid between the matrix and interface, undrained response in both constituents and drained response of the interface.

## ACKNOWLEDGEMENTS

I would like to express my sincere and deep appreciation to my co-supervisor, Prof. S. Pietruszczak for his constant guidance, criticism and encouragement throughout the research and preparation of this thesis. I would also like to thank, my co-supervisor the late Prof. F.A. Mirza for his guidance during this research. I want to extend this appreciation to Profs. J.D. Embury and D.F. Stolle for their interests and suggestions.

The financial assistance from the Department of Civil Engineering, the School of Graduate Studies of McMaster University, the Natural Science and Engineering Research Council of Canada are gratefully acknowledged.

I want to thank Dr. M. Pastor( CETA-CEDEX, Madrid) , Profs. J.H. Qian and S.S. Lu (Hohai Univ., Nanjing) for their guidance during my previous research. I also want to thank the Technician K. Peter for his help.

Finally, this thesis is dedicated to my family in appreciation of their support. I am especially grateful to my wife, Xilin, for her patience and understanding throughout the duration of this study.

## TABLE OF CONTENTS

ABSTRACT	iii
ACKNOWLEDGEMENTS	v
TABLE OF CONTENTS	vi
LIST OF FIGURES	xi
LIST OF TABLES	xvii
CHAPTER 1 INTRODUCTION	1
1.1    General remarks	1
1.2    Numerical analysis of strain localization	2
1.3    The scope of the thesis	7
CHAPTER 2 A CONSTITUTIVE MODEL FOR DESCRIBING STRAIN LOCALIZATION IN CONCRETE	11
2.1    Introduction	11
2.2    Fracture characteristics of concrete	13
2.3    Description of stable response	16
2.4    Transition to brittle response as a bifurcation problem	20

2.4.1	Bifurcation theory	20
2.4.2	Bifurcation analysis for the elastic-plastic model of concrete	22
2.5	Description of localized damage	23
2.5.1	Formulation incorporating a homogenization technique	23
2.5.2	An Alternative formulation of the homogenization technique	27
2.6	Constitutive model for the interface	32
2.6.1	Assumptions embedded in the interface model	32
2.6.2	Formulation of the interface model	33
2.6.3	Numerical simulations for the interface	37
2.7	Modelling of brittle response of concrete subjected to plane strain uniaxial compression	38
2.7.1	Implementation of the framework	38
2.7.2	Numerical simulations	39
<b>CHAPTER 3 FINITE ELEMENT ANALYSIS OF STRAIN LOCALIZATION IN CONCRETE STRUCTURES UNDER COMPRESSION</b>		<b>52</b>
3.1	Introduction	52
3.2	General description of nonlinear finite element analysis	53
3.2.1	Finite element implementation	53
3.2.2	Numerical algorithm for solving non-linear equations	56

3.3	Numerical integration of the constitutive equations	58
3.3.1	Numerical implementation of constitutive model before bifurcation	59
3.3.2	Numerical integration of constitutive equations after the onset of localization	62
3.4	Comments on sensitivity of the solution to discretization	65
3.4.1	Conventional strain-softening formulations	66
3.4.2	Solution based on the homogenization technique	67
3.5	Finite element analysis of concrete fracture in compression	69
CHAPTER 4 FINITE ELEMENT ANALYSIS OF STRAIN LOCALIZATION IN CONCRETE STRUCTURES UNDER TENSION		87
4.1	Introduction	87
4.2	Constitutive model for the interface	88
4.2.1	Assumptions embedded in the interface model	88
4.2.2	Formulation of the interface model	89
4.2.3	Comments on the degradation law for cohesion	93
4.3	Modelling of brittle response of concrete specimens subjected to plane strain uniaxial tension	94
4.4	Finite element analysis of notched specimens	95
4.3.1	Edge-notched tension tests	95
4.3.2	Three-point bending tests	96
4.3.3	Simulation of size effect	97

CHAPTER 5	DESCRIPTION OF LOCALIZED DEFORMATION IN SATURATED CEMENTED MATERIALS	105
5.1	Introduction	107
5.2	Homogenous deformation of saturated concrete	109
	5.2.1 Application to elastoplastic material	109
5.3	Transition to localized deformation as a bifurcation problem	111
	5.3.1 Localization in fluid-infiltrated elastoplastic cemented materials	112
	5.3.2 Bifurcation analysis of localization in saturated concrete	113
5.4	Mathematical description of undrained localized deformation in saturated cemented materials	114
	5.4.1 Formulation for undrained localized deformation	114
	5.4.2 Limited case I ( $C_d=0$ )	119
	5.4.3 Limited case II ( $C_d=\infty$ )	120
	5.4.4 Numerical simulations and discussions	122
	5.4.5 Comparison with the response of granular soil involving localized deformation	125
CHAPTER 6	CONCLUSIONS AND RECOMMENDATIONS	135
6.1	Summary and conclusions	135
6.2	Recommendations for future research	139
APPENDIX	A	141

APPENDIX B	142
APPENDIX C	145
APPENDIX D	146
APPENDIX E	149
BIBLIOGRAPHY	152

## LIST OF FIGURES

FIGURE		PAGE
2.1	Influence of the specimen height on fracture characteristics in uniaxial compression (after Van Mier 1984). (a) stress-strain curve and corresponding fracture pattern; (b) post-peak stress-displacement curve.	41
2.2	Influence of boundary constraints on the load-displacement behaviour and fracture pattern in uniaxial compression (after Kotsovos 1983).	42
2.3	Nominal stress versus axial strain curves obtained in displacement controlled standard triaxial compression tests (after Jamet et al 1984).	42
2.4	Stress-deformation curves for specimens under plane strain conditions at various levels of confinement (after Van Mier 1984).	43
2.5	Classification of fracture modes (after Van Mier 1984).	43
2.6	Failure surface in (a) principle stress space; (b) meridional plane; (c) deviatoric plane(after Jiang 1988).	44
2.7	Plastic potential surface in meridional plane(after Jiang 1988).	44

2.8	Numerical simulation of a ductile-brittle transition in plane strain uniaxial compression	45
	(a) initial confining pressure 0, 5 and 25 MPa;	
	(b) initial confining pressure 50, 100 and 150 MPa.	
2.9	Strain localization mechanism.	46
2.10	Interface with asperities.	46
2.11	Response of hard-formed gypsum joints subjected to direct shear	47
	(a) deviatoric characteristics; (b) volumetric characteristics.	
2.12	Influence of the convective term in the expression for the velocity discontinuity on the volumetric characteristics	48
2.13	Numerical simulations of unstable response for a series of plane strain uniaxial compression tests.	49
	(a) deviatoric characteristics; (b) volumetric characteristics.	
2.14	Influence of the height of the sample on average mechanical characteristics.	
	(a) deviatoric response; (b) Volumetric characteristics	50
	(c) distortion characteristics.	51
3.1	Analysis of a one-dimensional tension tests	74
	(a) discretization; (b) assumed local stress-strain relationship;	
	(c) possible global response for different discretization schemes.	
3.2	Finite element analysis of a strip foundation problem (after Pietruszczak and Stolle, 1985)	75

	(a) the geometry of the problem;	
	(b) the influence of discretization on load-displacement characteristics.	
3.3	Response of a concrete specimen with initial imperfections, subjected to plane strain uniaxial compression	
	(a) geometry of the problem;	
	(b) load-displacement characteristics;	76
	(c) and (d) deformed meshes for grids I and III, respectively.	77
3.4	Results for a concrete specimen with symmetrical imperfections	78
	(a) deformed mesh; (b) load-displacement characteristics.	
3.5	Influence of boundary constraint on deformation characteristics	79
	(a) deformed mesh; (b) mechanical characteristics.	
3.6	Influence of initial confining pressure on deformation characteristics	80
	(a) deformed mesh; (b) load-displacement characteristics.	
3.7	Influence of the height of sample on deformation characteristics	
	(a) geometry and the deformed mesh for sample 2.5x2.5;	
	(b) sample with the height of 1.25m and the width of 2.5m;	81
	(c) load-displacement characteristics.	82
3.8	Results of the analysis of a vertical cut problem	
	(a) discretization and the boundary conditions;	83
	(b) load-displacement characteristics; (c) and (d) deformed meshes for grid I and grid II, respectively.	84
3.9	Numerical analysis of failure mechanism of pillars under compression	
	(a) geometry, boundary conditions and discretization;	

	(b) load-displacement characteristics.	85
3.10	Deformation characteristics of pillars under compression	86
	(a) deformed mesh for pillar I at last loading stage;	
	(b) deformed mesh for pillar III at last loading stage.	
4.1	Numerical simulation of height effect in plane strain uniaxial tension	
	(a) stress-strain characteristics; (b) distortion characteristics.	99
4.2	Simulations of tension tests on edge-notched samples	
	(a) geometry and the boundary conditions;	
	(b) load-displacement characteristics.	100
4.3	Deformed meshes corresponding to simulations in Fig.4.2	
	(a)-(c) samples with $d=38\text{mm}$ , $76\text{mm}$ , and $152\text{mm}$ , respectively.	101
4.4	Simulations of three-point bending tests	
	(a) geometry and the boundary conditions;	
	(b) load-displacement characteristics.	102
4.5	Deformed meshes corresponding to simulations in Fig.4.4	
	(a)-(c) samples with $d=76\text{mm}$ , $152\text{mm}$ , and $308\text{mm}$ , respectively.	103
4.6	Plots of nominal strength at failure against the dimension $d$	104
5.1	Numerical simulations of a transition to localized deformation in saturated cemented material	
	(a) deviatoric characteristics;	
	(b) evolution of the excess pore pressure.	127

5.2	Comparison of localized response corresponding to $C_d=0$ and $C_d \rightarrow \infty$ (a) Deviatoric characteristics; (b) evolution of excess pore pressure.	128
5.3	Localized response corresponding to drained condition in the interface (a) deviatoric characteristics; (b) evolution of excess pore pressure.	129
5.4	Comparison of deviatoric characteristics for both saturated and dry samples	130
5.5	The influence of the height of the sample on the mechanical response ( $C_d=0$ ) (a) deviatoric characteristics; (b) evolution of excess pore pressure.	131
5.6	The influence of the height of the sample on mechanical response ( $C_d \rightarrow \infty$ ) (a) deviatoric characteristics; (b) evolution of excess pore pressure.	132
5.7	Influence of the height of the sample on mechanical response corresponding to drained conditions in the interface (a) deviatoric characteristics; (b) evolution of excess pore pressure.	133
5.8	The undrained characteristics of a cohesionless granular soil in the presence of shear band (after Pietruszczak 1995)	

(a) deviatoric characteristics;

(b) evolution of excess pore pressure.

134

## LIST OF TABLES

TABLE	PAGE
2.1 Results of bifurcation analysis for plane strain uniaxial compression tests	51

## CHAPTER 1

### INTRODUCTION

#### 1.1 General remarks

For the prediction of structural failures, two classical theories: plasticity and fracture mechanics, are well established. In plasticity theory, the failure is distributed over a plastic zone penetrating the interior of the structure. In fracture mechanics theory, the material failure is concentrated in a very narrow fracture zone propagating through the domain. Recently it became clear that the prediction of failure of various modern structures necessitates a combined theory in which the material failure first begins over a large zone but later localizes into a relatively small zone that propagates throughout the structure. This transitional type of failure is characterized by progressive development of material damage, usually in the form of distributed cracking which coalesces into a distinct fracture toward the end of the failure process ( cf. Mazars and Bazant, 1989 ). The materials which exhibit this type of failure mechanism are various brittle heterogenous materials, including cement-based aggregate composites (such as concrete), rocks, various modern toughened ceramics, many types of fibre and particle composites and, to some extent, even certain metals. The physical mechanisms responsible for triggering the onset of strain localization vary widely for the different materials. In the last few decades, the mathematical treatment of

the brittle failure has been the object of intensive research and a general review of various numerical techniques adopted, is provided below.

## 1.2 Numerical analysis of strain localization

Through the last decades, many approaches for numerical analysis of strain localization have emerged. All these approaches deal with the strain localization problem in three different ways: (a) material modelling including both distributed damage and localized damage; (b) special finite element techniques; and (c) development of solution techniques for equilibrium equation with non-positive definite coefficient matrix. It should be emphasized that material modelling is the essential part for numerical analysis of strain localization. Even with appropriate finite element techniques and numerical solution algorithms, the material modelling of localized damage has to be considered in order to maintain the mesh objectivity.

Finite element techniques include the introduction of special finite elements with embedded strain localization mode (Belytschko et al., 1988) (Ortiz et al., 1987) and adaptive remeshing technique (Pastor et al., 1991). It has been shown that, in order to maintain the mesh objectivity, both of these approaches should be combined with appropriate material modelling of localized damage. In order to solve the equilibrium equations with non-positive definite coefficient matrix, which is generally associated with strain localization, various numerical techniques, like arc-length control (Crisfield, 1983), indirect displacement control (de Borst, 1987) and total strain control (Chen and Schreyer, 1990), have been developed. Arc-length control was originally proposed for geometrically non-

linear problems. Indirect displacement control, involving some degrees of freedom, may be more suitable for strain localization analysis (de Borst, 1987). Regardless of which solution strategy is adopted, the problem of loss of mesh objectivity, exists if these techniques are used without considering material modelling of localized damage (Chen and Schreyer, 1990).

Material modelling has been developed at three different levels, i.e. micro-level, meso-level and macro-level. At the micro-level, the details of the microstructure of a material are considered. An example of such an approach is the model developed by Roelfstra (1989), in which the internal structure of concrete is represented by a computer generated composite. There are two main advantages of the micro-model. First, the crack formation, and its propagation and the strain localization phenomenon can be automatically modelled because of the structural heterogeneity. Second, the influence of the microstructural properties, such as the shape of aggregate grains, aggregate volume content and etc. on the material response can be studied. Although the micro-model is the best choice to describe material behaviour, it is very difficult to identify all material parameters involved and to apply the formulation in structural analysis. At the meso-level, the main characteristics of the microstructural, such as big pores, pre-existing cracks and inclusions are considered (Nemat-Nasser and Obata, 1988) (Horii et al., 1988) (Krajcinovic, 1988). If the distribution of pre-existing cracks and the direction of crack propagation are known, it is advantageous to choose this kind of model. However, in real structural analysis, it is usually impossible to know *a priori* how cracks would propagate. Consequently, the most widely-used models for structural analysis involving localization are continuum models at the macro-level.

For continuum models, the mathematical formulation of the strain localization problem generally involves two aspects. The first one relates to the establishment of an appropriate criterion governing the inception of the localized mode. The second involves the description of the non-homogenous deformation associated with a localized pattern. When the solid is modelled as rate-independent elasto-plastic material, the inception of strain localization is commonly considered as a bifurcation problem (Rudnicki and Rice, 1975). It should be noted that the quantitative assessment of the critical conditions governing the onset of localization is sensitive to the elastoplastic constitutive law (Ortiz, 1987). After the bifurcation, the deformed solid can no longer be considered as homogenous. The description of non-homogenous localized deformation is still a challenge to researchers. It is well-known that the standard rate-independent continuum theories cannot adequately model the localized damage. In a typical formation, the measured force-displacement response is simply converted to a stress-strain relation ignoring the inhomogeneous nature of the deformation process. As a result, the material parameters cannot be uniquely determined since the experimental response depends explicitly on the geometry of the specimen. In mathematical terms, the elliptic character of the set of governing differential equation for pseudo-static problems is lost and the numerical analysis suffers from spurious mesh sensitivity.

In order to overcome these deficiencies the classical continuum formations must be enriched by incorporating additional terms which reflect the evolution of the microstructure associated with the localized damage. In the last decades, several conceptually different approaches have emerged, e.g.

- (1) approach derived within the context of a polar(Cosserat) medium with

couple stresses which arise as a result of local rotation of microstructure (de Borst, 1991)(de Borst, 1993);

(2) non-local theories, first introduced within the context of elasticity and subsequently extended to localization problems (Bazant et al., 1988);

(3) concept of gradient limiters as applied to large deformation problems—the approach consists of adding a second-order gradient term to the expression for the strain energy density which leads to equilibrium equations which remain elliptic (Muhlhaus and Aifantis, 1991) (de Borst and Muhlhaus, 1992);

(4) viscoplastic regularization procedure, in which the rate independent elastoplastic response is regularized by viscoplasticity (Needleman, 1988) (Loret and Prevost, 1990).

(5) 'smeared shear band' approach, based on estimation of average mechanical properties of an initially homogenous system intercepted by shear band (Pietruszczak and Mroz, 1981).

There are numerous arguments concerning the validity and applicability of each of these formulations (Pietruszczak and Xu, 1995). In Cosserat continuum the generalized stress/strain components include couple-stress and micro-curvatures. The formulation incorporates an internal length scale, rendering the numerical solutions to be virtually independent of the details of discretization. A significant advantage of this formulation, as compared to other non-standard approaches, is that the framework can be implemented in finite element algorithms using standard plasticity procedures for deriving the tangent operators. A distinct drawback is the fact that the rotational degrees of freedom cannot be activated in pure tension. Consequently, for problems in which Mode-I failure is the predominant mechanism, the analysis may still suffer from deficiencies

pertinent to classical models.

In gradient theories, which may be considered as a sub-set of non-local theories, the functional form of the yield surface incorporates higher order gradients of inelastic strain. While non-local models require special numerical strategies, the gradient formulations are computationally more efficient (de Borst, 1993). Both these formulations however invoke non-standard boundary conditions. The presence of an internal length scale, once again, ensures the solutions are not affected by the discretization and thus remain objective, in a numerical sense. One of the major problems when dealing with higher order continua (as well as Cosserat medium) is the question of identification of material parameters. In general, these parameters cannot be measured or derived from elementary material tests. The only alternative seems to be fitting of experimental results of boundary-value problems by means of numerical simulations. This however is not only inefficient but also quite ambiguous, particularly in the case when a number of material parameters is involved. A similar problem arises within the context of a viscoplastic regularization, whereby it is difficult to differentiate between the effects of rate sensitivity of the material itself and the influence of inertial forces.

The 'smeared shear band' approach, which is adopted in this thesis, was originally proposed within the context of soil mechanics (Pietruszczak and Mroz, 1981). In concrete research, a similar concept of a 'smeared crack' has been used (Bazant and Oh, 1983). The formulations for both smeared shear band approach and smeared crack approach are conceptually similar. In the former, the total strain is decomposed into elastic strain in the intact material and the localized plastic strain in shear band. In the latter, the total strain is decomposed into

uncracked concrete strain and cracked strain. It should be pointed out that the static/kinematic constraints have not been adequately introduced in both original formulations. Only recently, the smeared shear band approach has been extended to incorporate this aspect and implemented in the finite element analysis of some geotechnical problems (Pietruszczak and Niu, 1993) and concrete structures (Pietruszczak and Xu, 1995).

### 1.3 The scope of the thesis

In this thesis, a constitutive model for describing strain localization in concrete is developed. The model is subsequently implemented in a finite element algorithm to solve a number of structural problems. Subsequently, a mathematical formulation is provided for describing the phenomenon of strain localization in saturated concrete.

In the development of a constitutive model, it is emphasized that the standard rate-independent continuum theories cannot adequately model the localized damage and must be enriched by incorporating additional terms to introduce an internal length parameter. The formulation based on a homogenization technique may be considered as such a non-standard continuum approach. In order to estimate the average mechanical properties of an initially homogeneous system intercepted by the strain localization zone, the evolution of the localized damage needs to be defined under various stress conditions. The proposed framework combines strain-hardening plasticity formulation, bifurcation criterion and the homogenization technique. The implementation of the proposed framework within the finite element algorithm requires an appropriate procedure

for the integration of the constitutive model and a suitable solution technique for equilibrium equations with a strongly nonsymmetric coefficient matrix. Finally, a proper formulation for the analysis of coupling between deformation and pore water diffusion is required to describe the localized deformation in saturated concrete. This coupling effect is studied through the analysis of three different limited cases. The description of localized deformation is also based on the homogenization technique, considering different formula for the pore pressure development.

In Chapter 2 the fracture characteristics of concrete under various stress states are first discussed. Subsequently, a constitutive model for describing the mechanical response of concrete and similar cemented aggregate mixtures is presented. The stable response, associated with the growth of microcracks, is described by a phenomenological plasticity framework. The transition to unstable response, invoking localized deformation, is considered as a bifurcation problem. In the localized mode, the mechanical behaviour is modelled by estimating, through a homogenization technique, the average mechanical properties of a medium intercepted by a macrocrack. The strain softening behaviour is the result of unstable response along the interface, triggered by a progressive degradation of surface asperities. The mathematical framework is illustrated by some numerical examples. The strain localization criterion, derived from conditions of stability of the constitutive relation governing the homogeneous deformation mode, is applied to determine the bifurcation point and the orientation of the macrocrack in a series of plane strain tests. The simulations of unstable response are also provided illustrating the effect of the size of the sample on average mechanical characteristics.

The implementation of the constitutive model in the finite element method is described in Chapter 3. First, the general description of non-linear finite element analysis of strain localization is presented. This includes the basic formulation of finite element model, the general solution algorithm for non-linear system and the numerical implementation of the framework for both stages; i.e. stable and unstable response, the latter associated with strain localization. The sensitivity of the solution to finite element discretization is studied through one-dimensional formulation and two-dimensional numerical analysis. Subsequently, the proposed framework is applied to analyze a series of structural boundary value problems, including stability of a vertical cut and plane strain compression of concrete pillars.

The interface model discussed in Chapter 3 is limited to the compressive shear fracture. In order to analyze the tension crack problem, the above approach is extended in Chapter 4. First, the interface model for both compressive shear fracture and tension failure is developed. Subsequently, modelling of brittle response of concrete specimens subjected to plane strain uniaxial tension is discussed. Finally, the performance of the model is illustrated by a numerical analysis of notched specimen under tension.

The mathematical description of localized deformation in saturated concrete is formulated in Chapter 5. The stable response is described based on a stress decomposition, which is different from Terzaghi's effective stress principle. The transition to localized deformation is considered as a bifurcation problem. The mathematical description of undrained localized deformation is derived based on a homogenization technique. The mathematical framework is

illustrated by the simulation of three limited cases, including (i) exchange of water between the matrix and the interface, (ii) undrained response of both constituents, and (iii) drained response of the interface. Comparison between these cases and the response of a dry sample is provided.

Conclusions drawn from this study and recommendation for future research are presented in Chapter 6.

## CHAPTER 2

### A CONSTITUTIVE MODEL FOR DESCRIBING STRAIN LOCALIZATION IN CONCRETE

#### 2.1 Introduction

Cemented aggregate mixtures are plastic-brittle materials. For such materials, the deformation process consists initially of nucleation and growth of microcracks. For certain stress paths, however, the subsequent damage may become confined to discrete failure planes. Formation of such a mechanism is usually associated with an unstable (strain softening) response. The objective of this chapter is to propose a methodology for describing both stages of the deformation process. The work described here is an extension of research reported earlier by Pietruszczak et al. (1988). In this reference, a constitutive model for concrete, built with the framework of rate-independent theory of plasticity, is presented. Although the material description includes the unstable response, the formulation of the problem is not rigorous. That is, the inception of strain softening, corresponding to formation of a macrocrack, is governed by a path-independent criterion which is imposed *a priori* and the mathematical formulation incorporates some empirically-based functions correlating the rate of strain-softening with geometrical aspects. In this chapter, a more rigorous approach is pursued. The ductile-brittle transition is considered as a bifurcation

problem which reflects the loss of stability of the constitutive equation governing the homogeneous deformation. The strain softening behaviour is attributed to a non-homogeneous mode resulting from macroscopic fracturing and subsequent sliding along asperities. The response in the unstable regime is defined by following the procedure similar to that proposed by Pietruszczak & Niu (1993), i.e., estimating the average mechanical properties of a heterogeneous medium consisting of an interface and the adjacent intact material.

This chapter is divided into six main parts. In the first part, a brief discussion on the fracture characteristics of concrete under different stress states is provided in order to set up a physical background for a subsequent mathematical description of the behaviour. In the second part, a constitutive model for the description of the distributed damage, associated with a stable response, is briefly outlined. In the third part, the bifurcation theory is reviewed and subsequently applied to investigate the inception of strain localization, i.e. the formation of a macrocrack. Numerical examples include the simulation of a series of plane strain uniaxial compression tests performed at different initial confining pressures. In particular, the sensitivity of the ductile-brittle transition and that of the orientation of the macrocrack to the initial test conditions are investigated. The predicted qualitative trends are consistent with the existing experimental data discussed in the first part of the chapter and those reported by Palaniswamy and Shah (1974). In the fourth part, a homogenization technique for dealing with localized deformation mode is reviewed (after Pietruszczak and Niu, 1993). Then, an alternative formulation for the homogenization procedure is developed, which is believed to be more efficient within the context of numerical integration. In order to complete the formulation, a constitutive model for the interface is

proposed in the fifth part. The complete formulation is then applied to study the average response of non-homogeneous samples in the unstable region. In particular, the sensitivity to geometrical effects is investigated. It is shown that the results are again consistent with the experimental data discussed in the first part of this chapter.

## 2.2 Fracture characteristics of concrete

The tensile behaviour of concrete has long been considered to be of minor importance to failure analysis. This is due to the fact that concrete is a material that is most suitable to withstand compressive rather than tensile stresses. With the introduction of fracture mechanics, however, it becomes clear that the tensile properties play a dominant role in the failure of concrete structures. The stress-deformation relation for tensile loading can be represented by the pre-peak region, peak value and post-peak region. In the pre-peak region, existing microcracks start to grow and/or new microcracks develop due to debonding between the coarse aggregates and the matrix. With increasing deformation, the microcracks coalesce, finally resulting in a single macrocrack at the peak strength. After the formation of a continuous macrocrack the stress transferring capacity only exists for sliding friction between the crack surfaces. The behaviour of a structure is seldom confined to pure tension mode. It is generally recognized that cracks are initiated in pure tension mode and are then transformed from a pure tension mode to a tension-shear mixed mode.

In comparison with fracture in tension, the response under compressive stresses seems to be more complicated. The uniaxial compressive behaviour can

be described by the complete stress-deformation curve, which includes again the pre-peak region, peak value and post-peak region. In the pre-peak region, the deformation is almost uniform involving a stable microcracks' growth. However, after formation of a discrete macrocrack, the deformation becomes inhomogeneous and consists predominantly of sliding along the macrocrack. The response is affected by many factors, such as geometry of the specimens and boundary constraints.

Fig. 2.1a shows the axial stress-strain curves for three specimens of different heights (after Van Mier 1984). The pre-peak response of the stress-strain curves is the same, however, in the post-peak region, the slope of the softening branch decreases with decreasing height of the specimen. When the load-displacement curve after the peak load is plotted (Fig. 2.1b), the slope of the descending branch is similar for all three specimens. It is evident that, however, that the same response in terms of average stress and strain is no longer invariant with respect to the height of the specimen. The fracture patterns, which are included in Fig.2.1a, are also affected by the geometry of the specimen.

Fig. 2.2 shows the influence of boundary constraints on the fracture behaviour of uniaxially compressed cylinders (after Kotsovos 1983). When the friction at the specimen-loading platen interface is reduced, the slope of the softening branch becomes more steep. The various observed fracture modes are shown in the same figure. Decreasing the boundary constraint leads to a decrease in the inclination of the macroscopic fracture plane.

Fig. 2.3 shows nominal stress versus axial strain diagrams obtained by

Jamet et al. (1984) for a number of standard displacement controlled triaxial compression tests at various levels of confining stress. At the lower confining stress (0-25 MPa), localized fractures (shear bands with the inclination of 25-30 degree to the axial loading direction) are observed and the post-peak response is brittle. When the confining stress is larger than 50 MPa, no visible damage is detected at the specimen surface and the plastic response remains stable. The brittle-ductile transition takes place between the confining stress of 25 and 50 MPa.

Fig. 2.4 shows a stress-deformation curve under plane strain conditions (after Van Mier 1984). The results do not show any sign of a brittle-ductile transition at the given levels of confining pressures. It is evident that the brittle-ductile transition occurs at much higher level of confining pressure for plane strain compression when compared to that corresponding to the triaxial compression.

Based on the experimental results, the classification of fracture modes can be made as shown in Fig. 2.5 (after Van Mier 1984). There are three possible fracture modes indicated in the figure: first, tensile fracture, which is characterized by a single fracture plane perpendicular to the tensile direction; second, distributed fracture in regions near the compressive meridian; and finally localized shear fracture for specimens failing with the formation of a dominant fracture surface parallel to the intermediate compressive direction.

The following conclusions could also be drawn from experimental results:

- (1) Fracture in uniaxial compression and thus also in multiaxial

compression, should be regarded as a structural property because of the pronounced influence of boundary conditions on the softening response.

(2) Similarities between compressive and tensile fracture are shown to exist. In both cases, fracture is a localized phenomenon, and is associated with non-uniform deformation in the post-peak region.

(3) Under multiaxial stress states, discrete shear bands are observed below the brittle-ductile transition, which indicates a localized mechanism similar to Mode-II cracking. Thus the frictional characteristics of the shear band must be taken into account.

### 2.3 Description of stable response

The constitutive model employed in this study is based on the phenomenological plasticity framework proposed by Pietruszczak et al. (1988). The formulation invokes the concept of a failure locus  $F(\sigma_{ij})=0$ , which is introduced *a priori* as a path-independent criterion. The progressive damage of the material due to microcracking is described in terms of evolution of the family of yield surfaces  $f(\sigma_{ij}, \xi)=0$ , where  $\xi$  is a damage parameter. The direction of plastic flow is defined using a non-associated flow rule, which involves the existence of a family of plastic potential surfaces defined in a parametric form as  $\Psi(\sigma_{ij})=\text{const}$ . The material characteristics are largely affected by the value of confining pressure. The original formulation allows for a smooth transition from a ductile (stable) to brittle (unstable) response by employing an appropriate form of strain hardening/softening function. The formulation outlined here is restricted to a stable deformation mode (strain hardening) only.

The failure locus is chosen in the form

$$F = \bar{\sigma} - g(\theta)\bar{\sigma}_c = 0 \quad (2.1)$$

where

$$\bar{\sigma}_c = \frac{-a_1 + \sqrt{(a_1^2 + 4a_2(a_3 + I/f_c))}}{2a_2} f_c \quad (2.2)$$

In above equations  $I = -\sigma_{ii}$ ,  $\sigma = (1/2 s_{ij} s_{ij})^{1/2}$ ,  $\theta = 1/3 \sin^{-1} (3\sqrt{3} J_3 / 2 \sigma^3)$  and  $J_3 = 1/3 s_{ij} s_{jk} s_{ki}$  are stress invariants. Moreover, the parameters  $a_1$ ,  $a_2$  and  $a_3$  represent dimensionless material constants and  $f_c$  denotes the uniaxial compressive strength of concrete. It should be noted that in the principal stress space, eq. (2.1) describes an irregular cone with smooth curved meridians and a non-circular convex cross-section, defined by  $g(\theta)$  (Fig. 2.6). The functional form of  $g(\theta)$  is assumed to be affected by the value of confining pressure. A number of possible representations for this function have been provided by Jiang and Pietruszczak (1988) and the following simple form is adopted

$$g(\theta) = \frac{(\sqrt{1+a} - \sqrt{1-a})K}{K\sqrt{1+a} - \sqrt{1-a} + (1-K)\sqrt{(1-a)\sin 3\theta}} \quad , \quad a \rightarrow 1 \quad (2.3)$$

In eq.(2.3), the parameter  $K$  is defined as the ratio of the maximum deviatoric stress intensity in extension and compression domains and is assumed to be a function of confining pressure. The following simple function describing the variation of  $K$  is selected

$$K = 1 - K_0 \exp\left(-K_1 \left(a_3 + \frac{I}{f_c'}\right)\right) \quad (2.4)$$

where  $K_0$  and  $K_1$  are material constants. It should be noted that according to eq. (2.3) and eq. (2.4) the shape of the  $\pi$ -plane section changes from a curvilinear triangle for low confining pressures to a nearly circular at high pressures (Fig.2.6).

The yield surface is chosen in a functional form, similar to that of eq.(2.1), as,

$$f = \bar{\sigma} - \beta(\xi)g(\theta)\bar{\sigma}_c \quad (2.5)$$

where  $\beta(\xi)$  represents a hardening function. The internal variable  $\xi$  is related to the history accumulated plastic distortions

$$\xi = \int d\xi, \quad d\xi = \frac{(de_{ij}^p de_{ij}^p)^{1/2}}{\bar{\phi}} \quad (2.6)$$

where  $de_{ij}^p$  represents the deviatoric part of the plastic strain increment and  $\bar{\phi} = \text{const.}$  is defined through a parametric equation

$$\phi(I, \theta) = [g(\theta)(a_3 + I/f_c')]^2 = \bar{\phi} \quad (2.7)$$

The direction of plastic flow is governed by a non-associated flow rule and the corresponding plastic potential (see Fig.2.7) is selected in the form

$$\psi = \bar{\sigma} + m_c g(\theta) \bar{I} \ln(\bar{I}/\bar{I}_0) \quad (2.8)$$

where  $I = a_0 f_c + I$  and  $a_0$  defines the location of the apex of the current potential surface in tensile domain. In eq. (2.8)  $m_c$  represents the value of  $m = \sigma / (g(\theta) I)$  at which a transition from compaction to dilatancy takes place ( $de_{ii}^p = 0$ ). It is assumed that such transition occurs along the locus defined by

$$\bar{f} = \bar{\sigma} - \alpha g(\theta) \bar{\sigma}_c = 0 \quad (2.9)$$

in which  $\alpha$  is a material constant.

Finally, the hardening function may be chosen in a simple hyperbolic form

$$\beta = \xi / (A + B\xi) \quad (2.10)$$

where  $A$  and  $B$  are material constants. According to eq.(2.1) and eq.(2.5),  $\beta(\xi) \rightarrow 1$  implies that the yield surface asymptotically approaches the failure envelope.

Following the standard plasticity formulation procedure, the constitutive tensor could be derived as

$$D^{ep}_{ijkl} = D^e_{ijkl} - \frac{D^e_{ijkl} \frac{\partial \phi}{\partial \sigma_{pq}} \frac{\partial f}{\partial \sigma_{mn}} D^e_{mnkl}}{H_e + H_p} \quad (2.11)$$

where

$$H_e = \frac{\partial f}{\partial \sigma_{pq}} D^e_{pqrs} \frac{\partial \phi}{\partial \sigma_{rs}} ; H_p = - \frac{\partial f}{\partial \beta} \frac{d\beta}{d\xi} \frac{\left( \text{dev} \frac{\partial \phi}{\partial \sigma_{ij}} \text{dev} \frac{\partial \phi}{\partial \sigma_{ij}} \right)^{1/2}}{\bar{\phi}} \quad (2.12)$$

and  $H_p$  represents the plastic hardening modulus.

#### 2.4 Transition to brittle response as a bifurcation problem

The growth of microcracks is a fairly distributed process which is associated with a stable material response. For certain stress trajectories however, a different deformation mode may prevail consisting of a formation of discrete failure planes (macrocracks). In the later case, the mechanical response as observed on the macroscale becomes, in general, unstable. The inception of localized mode may be considered as a bifurcation problem, i.e. loss of stability of the constitutive relation governing the homogenous deformation. The conditions under which localized modes arise have been investigated by a number of researchers. Preference has been given to study the shear band formation in ductile materials like metals or soils (Rudnicki and Rice, 1975) and only limited research has been conducted within the context of brittle materials (Ortiz, 1987). Some of the basic principles underlying the theory follow from early studies on elastic stability, extended later to inelastic materials (Hill, 1958; Thomas, 1961).

##### 2.4.1 Bifurcation theory

Consider a homogeneous sample undergoing uniform deformation and

establish conditions under which an alternative mode of deformation invoking existence of a plane of strain discontinuity becomes possible. Let  $\mathbf{n}$  denote the normal to the incipient plane of a discontinuity. The compatibility condition requires a jump in the velocity gradients of the form

$$[[\dot{u}_{ij}]] \equiv \dot{u}_{ij}^+ - \dot{u}_{ij}^- = \dot{g}_i n_j = \dot{g} m_i n_j \quad (2.13)$$

where the superscripts 'plus' and 'minus' refer to the two sides of the plane of the discontinuity and  $\mathbf{m}$  is the unit vector along  $\mathbf{g}$ . The corresponding strain jump is defined as

$$[[\dot{\epsilon}_{ij}]] = \frac{1}{2}(\dot{g}_i n_j + n_i \dot{g}_j) = \frac{1}{2}(m_i n_j + m_j n_i) \dot{g} \quad (2.14)$$

Equilibrium across the discontinuity planes requires the traction to be continuous

$$[[t_j]] = [[n_i \dot{\sigma}_{ij}]] = n_i [[\dot{\sigma}_{ij}]] \quad (2.15)$$

The incremental stress-strain relation takes the form

$$\dot{\sigma}_{ij} = D_{ijkl} \dot{\epsilon}_{kl} \quad (2.16)$$

where  $D_{ijkl}$  is the elastoplastic tangent stiffness tensor. By assuming the plastic loading on both sides of the discontinuity plane at the bifurcation point, eq.(2.15), eq.(2.16) and eq.(2.14) can be combined to yield

$$n_i D_{ijkl} [[\dot{\epsilon}]] = \frac{1}{2} n_i D_{ijkl} (m_k n_l + n_l m_k) \dot{g} \quad (2.17)$$

Considering  $D_{ijkl}=D_{jik}$ , the condition for the inception of strain localization takes the form

$$\det B_{jk}=0 \quad , \quad B_{jk}=n_i D_{ijkl} n_l \quad (2.18)$$

Equation (2.18) represents the necessary condition for localization. The solution defines the normal to the possible plane of strain discontinuity. The geometry of the localized mode is fully determined by  $\mathbf{n}$  and the corresponding zero eigenvectors  $\mathbf{m}$  of the acoustic tensor  $B_{jk}$ . In numerical terms, the problem reduces to a constrained minimization problem for  $f(\mathbf{n}_i)=\det B_{jk}$  under  $n_i n_i = 1$  (Appendix A).

#### 2.4.2 Bifurcation analysis based on the elastic-plastic model of concrete

The above approach has been applied to study the onset of localization using the constitutive model summarized in the previous section. In particular, a series of plane strain uniaxial compression tests have been simulated assuming the following parameters:

$$E=35,000 \text{ MPa}, \nu=0.20, f_c=50 \text{ MPa}, f_t=5 \text{ MPa}, A=0.000085, B=0.95$$

The main objective was to investigate the sensitivity of the inception of the localized mode to the initial confining pressure. The constitutive relation for concrete has been integrated using a forward-Euler explicit algorithm and imposing mixed boundary conditions, i.e.  $\epsilon_{22} < 0$  ( $\epsilon_{i3}=0$ ,  $i=1,2,3$ ) under  $\sigma_{11}=0$ . At each integration step the constitutive tensor  $D_{ijkl}$  was computed and the localization conditions checked.

The results are presented in Fig. 2.8. The figure shows the deviatoric

characteristics corresponding to different initial confining pressures ranging from 0 to 150 MPa. Table 2.1 gives the numerical details pertaining to the detection of the bifurcation point and the orientation of the failure plane. It is clear that the inception of localized mode is delayed by increasing the initial confining pressure. At low initial confining pressures, from 0 to 25 MPa, the transition to localized mode takes place at axial strain intensities within a range of 0.5 percent. As the confining pressure increases, the stable mode associated with formation and growth of microcracks becomes predominant. At high pressure, larger than 100 MPa, the discrete failure planes can only form at strain levels which are practically not attainable within the context of typical boundary-valued problems, implying that the failure mode involves primarily the distributed damage. These results are in agreement with the experimental observation (Fig. 2.3 and Fig. 2.4). The initial conditions also affect the orientation of the failure plane. In particular, the inclination of the plane with respect to the major principle stress progressively decreases with the increasing initial confining pressure.

## 2.5 Description of localized damage

### 2.5.1 Formulation incorporating a homogenization technique

Consider a volume of the material adjacent to a strain localization zone, i.e., shear band or macrocrack which intercepts this region (Fig 2.9). Let  $\dot{\sigma}^{(i)}$ ,  $\dot{\epsilon}^{(i)}$  ( $i=1,2$ ) denote the average stress/strain rates in the constituents involved; i.e. within the intact material and the medium confined to the strain localization zone. Both of these tensorial fields are considered to be homogenous within themselves. Assume that the constituents are perfectly bonded and denote by  $\dot{\sigma}$  and  $\dot{\epsilon}$  the

volume averages of stress/strain rates in this element. Both of these rates are defined through the volume averaging procedure (Hill, 1963)

$$\dot{\sigma} = \mu_1 \dot{\sigma}^{(1)} + \mu_2 \dot{\sigma}^{(2)} \quad ; \quad \dot{\epsilon} = \mu_1 \dot{\epsilon}^{(1)} + \mu_2 \dot{\epsilon}^{(2)} \quad (2.19)$$

where  $\mu$ 's are the respective volume fractions. It should be emphasized that  $\sigma$  and  $\epsilon$  refer to the macroscopic stress and the deformation of the constituents and are not intended as measures of stresses and the deformation process at the microscopic level. For the discussion that follows, eq. (2.19) are supplemented by a set of kinematic and static constraints

$$k_j(\dot{\epsilon}^{(1)}, \dot{\epsilon}^{(2)}) = 0 \quad ; \quad s_j(\dot{\sigma}^{(1)}, \dot{\sigma}^{(2)}) = 0 \quad (2.20)$$

where the  $k$ 's and  $s$ 's are scalar-valued functions and  $j$  specifies the number of constraints. Eq. (2.19) and eq. (2.20), together with the corresponding constitutive relations, form a set of differential equations which is complete; i.e. the response of the composite is uniquely defined in terms of the properties of the constituents and respective volume fractions. It should be noted that the constraints of eq. (2.20), which are frequently used to estimate the properties of fibre-reinforced (Dvorak and Bahei-El-Din, 1982) and layered composites (Sawicki, 1983), are restrictive. Rigorous formulation requires, in general, that the kinematic compatibility and static constraints be specified in terms of velocities and traction along the interface between the constituents. This is a rather strong assumption which has to eventually be relaxed in order to render a feasible solution.

Within the context of an inhomogeneity in the form of a shear band,

constraints eq.(2.20) can be expressed in the form (three-dimensional formulation)

$$\begin{aligned} \dot{\epsilon}_{11} = \dot{\epsilon}_{11}^{(1)} = \dot{\epsilon}_{11}^{(2)}; \quad \dot{\epsilon}_{33} = \dot{\epsilon}_{33}^{(1)} = \dot{\epsilon}_{33}^{(2)}; \quad \dot{\gamma}_{13} = \dot{\gamma}_{13}^{(1)} = \dot{\gamma}_{13}^{(2)} \\ \dot{\sigma}_{22} = \dot{\sigma}_{22}^{(1)} = \dot{\sigma}_{22}^{(2)}; \quad \dot{\sigma}_{12} = \dot{\sigma}_{12}^{(1)} = \dot{\sigma}_{12}^{(2)}; \quad \dot{\sigma}_{23} = \dot{\sigma}_{23}^{(1)} = \dot{\sigma}_{23}^{(2)} \end{aligned} \quad (2.21)$$

Here the coordinate system has been chosen in such a way that  $x_2$  - axis is normal to the strain discontinuity plane (Fig. 2.9) and  $\dot{\epsilon}$  is defined as  $\dot{\epsilon} = \{\dot{\epsilon}_{11}, \dot{\epsilon}_{22}, \dot{\epsilon}_{33}, \dot{\gamma}_{12}, \dot{\gamma}_{13}, \dot{\gamma}_{23}\}^T$ . For two-dimensional formulation, the components associated with index three should be omitted.

The thickness of the strain localization zone is assumed to be negligible compared to the other physical dimensions involved. Thus, it can be formally be eliminated from macroscopic considerations by expressing the local deformation field in terms of velocity discontinuities  $\dot{\mathbf{g}}$  rather than strain rates  $\dot{\epsilon}^{(2)}$ . Denoting  $\dot{\mathbf{g}}$  as  $\dot{\mathbf{g}} = \{\dot{g}_2, \dot{g}_1, \dot{g}_3\}^T$ , where  $\dot{g}_2$  is the normal component and  $\dot{g}_1$  and  $\dot{g}_3$  the tangential components of the velocity discontinuity, the strain decomposition in eq.(2.19), combined with the kinematic constraint in eq.(2.21), reduces to

$$[\delta]\dot{\epsilon} = [\delta]\dot{\epsilon}^{(1)} + \mu\dot{\mathbf{g}} \quad (2.22)$$

where

$$[\delta] = \begin{bmatrix} 0 & 1 & 0 & 0 & 0 & 0 \\ 0 & 0 & 0 & 1 & 0 & 0 \\ 0 & 0 & 0 & 0 & 0 & 1 \end{bmatrix} \quad (3-D); \quad [\delta] = \begin{bmatrix} 0 & 1 & 0 \\ 0 & 0 & 1 \end{bmatrix} \quad (2-D)$$

In eq.(2.22),  $\mu$  defines the ratio of the cross-sectional area of the failure plane to the volume of the representative element. Thus,  $\mu^{-1}$  has the dimension of length and may be considered as an internal length parameter.

Assume that both constituents involved, i.e. matrix (1) and interface material (2), represent elastoplastic media and the mechanical response can be defined by incremental relations

$$\dot{\sigma}^{(1)} = [D]\dot{\epsilon}^{(1)} \quad ; \quad \dot{\sigma}^{(2)} = [K]\dot{g} \quad (2.23)$$

It is apparent that the problem is mathematically determinate. Indeed, the stress decomposition in eq.(2.19), together with eq.(2.21), eq.(2.22) and eq.(2.23) provides the set of 27 equations for 27 unknowns in a three-dimensional problem and 17 equations for 17 unknowns in a two-dimensional problem. Combining the above equations results (Appendix B), after some algebraic manipulations, in a relation between the overall strain rate and the strain rate in the matrix as well as the velocity discontinuity

$$\dot{\epsilon}^{(1)} = [S_1]\dot{\epsilon} \quad ; \quad \dot{g} = [S_2]\dot{\epsilon} \quad (2.24)$$

Considering that the components of the stress rates in both constituents are comparable, the following approximation may be employed

$$\dot{\sigma} \approx \dot{\sigma}^{(1)} = [D][S_1]\dot{\epsilon} \quad (2.25)$$

Eq. (2.25), supplemented by relations eq.(2.23) and eq.(2.24), provides a complete mathematical solution, i.e. defines the overall response as well as the stress/strain rates in both constituents. The overall response, due to the presence

of the inhomogeneity, is strongly anisotropic. The mechanical properties do not explicitly depend on the thickness of strain localization zone (this effect is however implicitly included in the stress-displacement relation), but are affected by its orientation and the dimension  $\mu$ , defined in eq.(2.22).

It should be noted that the above formulation is derived in local coordinates attached to the interface, so that a transformation to the global coordinate system is required. The transformation matrixes are provided in Appendix C. It should be noted that under the monotonic loading condition, the intact material will commonly undergo unloading after onset of strain localization while the interface will experience an active loading process.

#### 2.5.2 An alternative formulation of the homogenization technique

The numerical integration of eq.(2.25) requires some, *a priori*, assumptions pertaining to the deformation mode of constituents. This can result in serious numerical problems when the integration is carried out within the context of a boundary-valued problem. In order to overcome this deficiency, an alternative formulation, which is similar to the approach used in plasticity with multiple yield surfaces, is proposed. The proposed formulation is based on the following decomposition of the total strain rates, which is derived from eq. (2.22)

$$\dot{\epsilon} = \dot{\epsilon}^e + \dot{\epsilon}^p + \eta N^T \dot{g} \quad (2.26)$$

where N is a transformation matrix (Appendix C). The plastic strain rates for the matrix material are defined as,

$$\dot{\epsilon}^p = \dot{\lambda}^{(1)} \frac{\partial Q^{(1)}}{\partial \sigma} \quad (2.27)$$

where  $Q^{(1)}$  is the plastic potential and  $\dot{\lambda}^{(1)}$  is a non-negative multiplier, which can be determined from the consistency condition

$$\frac{\partial f^{(1)T}}{\partial \sigma} \dot{\sigma} + H_p^{(1)} \dot{\lambda}^{(1)} = 0 \quad (2.28)$$

where  $H_p^{(1)}$  is the plastic modulus and  $f^{(1)}$  is the yield function for the matrix material.

Thus, the stress and strain rates are related through

$$\dot{\sigma} = D \dot{\epsilon}^e = D \left[ \dot{\epsilon} - \dot{\lambda}^{(1)} \frac{\partial Q^{(1)}}{\partial \sigma} - \eta N \dot{g} \right] \quad (2.29)$$

Similarly, the velocity discontinuity  $\dot{g}$  could be derived from the plastic potential  $Q^{(2)}$  for the interface

$$\dot{g}^p = \dot{\lambda}^{(2)} \frac{\partial Q^{(2)}}{\partial \sigma} \quad (2.30)$$

with  $\dot{\lambda}^{(2)}$  being a non-negative multiplier, which can be determined from consistency condition

$$\frac{\partial f^{(2)T}}{\partial \sigma} \dot{\sigma} + H_p^{(2)} \dot{\lambda}^{(2)} = 0 \quad (2.31)$$

where  $H_p^{(2)}$  is plastic modulus and  $f^{(2)}$  is the yield function for the interface.

Thus, a stress rate and the velocity discontinuity relation can be expressed as

$$N^T \dot{\sigma} = K^e \dot{g}^e = K^e \left[ \dot{g} - \dot{\lambda}^{(2)} \frac{\partial Q^{(2)}}{\partial \sigma} \right] \quad (2.32)$$

Multiplying eq.(2.29) by  $N^T$  and invoking (2.32), one obtains

$$N^T D^e \frac{\partial Q^{(1)}}{\partial \sigma} \dot{\lambda}^{(1)} + [K^e + \eta N^T D^e N] \dot{g} - K^e \frac{\partial Q^{(2)}}{\partial \sigma} \dot{\lambda}^{(2)} = N^T D^e \dot{\epsilon} \quad (2.33)$$

Solving for  $\dot{g}$  from eq. (2.33) and substituting into eq. (2.29), yields the following constitutive relation:

$$\dot{\sigma} = D^e \dot{\epsilon} - D^e \frac{\partial Q^{(1)}}{\partial \sigma} \dot{\lambda}^{(1)} - D_K^e \frac{\partial Q^{(2)}}{\partial \sigma} \dot{\lambda}^{(2)} \quad (2.34)$$

where

$$\begin{aligned} D^e &= D^e - \eta D^e N [K^e + N^T D^e N]^{-1} N^T D^e \\ D_K^e &= \eta D^e N [K^e + N^T D^e N]^{-1} K^e \end{aligned} \quad (2.35)$$

In order to complete the formulation, the parameters  $\dot{\lambda}^{(1)}$  and  $\dot{\lambda}^{(2)}$  have to be determined. Multiplying eq.(2.29) by  $(\partial f / \partial \sigma)$  and invoking eq (2.28) gives

$$\left[ \frac{\partial f^{(1)T}}{\partial \sigma} D^e \frac{\partial Q^{(1)}}{\partial \sigma} + H_p^{(1)} \right] \dot{\lambda}^{(1)} + \frac{\partial f^{(1)T}}{\partial \sigma} D_K^e \frac{\partial Q^{(2)}}{\partial \sigma} \dot{\lambda}^{(2)} = \frac{\partial f^{(1)T}}{\partial \sigma} D^e \dot{\epsilon} \quad (2.36)$$

Similarly, multiplying eq.(2.32) by  $(\partial f/\partial \sigma)$  and invoking eq. (2.31) gives

$$\frac{\partial f^{(2)T}}{\partial \sigma} K_D \frac{\partial Q^{(2)}}{\partial \sigma} \dot{\lambda}^{(1)} + \left[ \frac{\partial f^{(2)T}}{\partial \sigma} K^{\mathcal{E}} \frac{\partial Q^{(2)}}{\partial \sigma} + H_P^{(2)} \right] \dot{\lambda}^{(2)} = \frac{\partial f^{(2)T}}{\partial \sigma} K_D \dot{\epsilon} \quad (2.37)$$

where

$$\begin{aligned} K^{\mathcal{E}} &= K^e - K^e [K^e + N^T D^e N]^{-1} K^e \\ K_D &= K^e [K^e + N^T D^e N]^{-1} N^T D^e \end{aligned} \quad (2.38)$$

Solving now eq. (2.36) and eq. (2.37), one obtains

$$\begin{aligned} \dot{\lambda}^{(1)} &= \frac{H_{22} \frac{\partial f^{(1)T}}{\partial \sigma} D^{\mathcal{E}} - H_{12} \frac{\partial f^{(2)T}}{\partial \sigma} K_D}{H_{11} H_{22} - H_{12} H_{21}} \dot{\epsilon} \\ \dot{\lambda}^{(2)} &= \frac{H_{11} \frac{\partial f^{(2)T}}{\partial \sigma} K_D - H_{21} \frac{\partial f^{(1)T}}{\partial \sigma} D^{\mathcal{E}}}{H_{11} H_{22} - H_{12} H_{21}} \dot{\epsilon} \end{aligned} \quad (2.39)$$

with

$$\begin{aligned} H_{11} &= \frac{\partial f^{(1)T}}{\partial \sigma} D^{\mathcal{E}} \frac{\partial Q^{(1)}}{\partial \sigma} + H_P^{(1)}; & H_{12} &= \frac{\partial f^{(1)T}}{\partial \sigma} D^{\mathcal{E}} \frac{\partial Q^{(2)}}{\partial \sigma} \\ H_{21} &= \frac{\partial f^{(2)T}}{\partial \sigma} K_D \frac{\partial Q^{(2)}}{\partial \sigma} & ; & H_{22} = \frac{\partial f^{(2)T}}{\partial \sigma} K^{\mathcal{E}} \frac{\partial Q^{(2)}}{\partial \sigma} + H_P^{(2)} \end{aligned} \quad (2.40)$$

Finally, substituting eq.(2.39) into eq. (2.29) yields the following expression

$$\dot{\sigma} = \left[ D^{ef} - H_{22} \frac{D^{ef} \frac{\partial Q^{(1)}}{\partial \sigma} \frac{\partial f^{(1)T}}{\partial \sigma} D^{ef}}{H_{11}H_{22} - H_{12}H_{21}} + H_{12} \frac{D^{ef} \frac{\partial Q^{(1)}}{\partial \sigma} \frac{\partial f^{(2)T}}{\partial \sigma} K_D}{H_{11}H_{22} - H_{12}H_{21}} \right. \\ \left. - H_{11} \frac{D_K \frac{\partial Q^{(2)}}{\partial \sigma} \frac{\partial f^{(2)T}}{\partial \sigma} K_D}{H_{11}H_{22} - H_{12}H_{21}} + H_{21} \frac{D_K \frac{\partial Q^{(2)}}{\partial \sigma} \frac{\partial f^{(1)T}}{\partial \sigma} D^{ef}}{H_{11}H_{22} - H_{12}H_{21}} \right] \dot{\epsilon} \quad (2.41)$$

In eq. (2.41),  $D^{ef}$  represents the elastic properties of the composite materials. When the matrix is under elastic deformation and the interface undergoes plastic deformation, eq. (2.41) simplifies to

$$\dot{\sigma} = \left[ D^{ef} - \frac{D_K \frac{\partial Q^{(2)}}{\partial \sigma} \frac{\partial f^{(2)T}}{\partial \sigma} K_D}{H_{22}} \right] \dot{\epsilon} \quad (2.42)$$

On the other hand, when the matrix is under plastic deformation and the interface remains elastic, the following expression is obtained

$$\dot{\sigma} = \left[ D^{ef} - \frac{D^{ef} \frac{\partial Q^{(1)}}{\partial \sigma} \frac{\partial f^{(1)T}}{\partial \sigma} D^{ef}}{H_{11}} \right] \dot{\epsilon} \quad (2.43)$$

In principle, eq.(2.41) is identical to eq.(2.25), but more suitable for integration in a finite element algorithm. The details of the integration procedure are discussed in Chapter 3.

## 2.6 Constitutive model for the interface

The interface behaviour is, in general, quite different under compression and tension. The applicability of the constitutive model for the interface proposed below is restricted to the case where the normal stress is compressive. An extension to include tensile normal stress is discussed in Chapter 4.

### 2.6.1 Assumptions embedded in the interface model

Assume that the deformation in the neighbourhood of the interface results from sliding along a set of asperities with a predefined orientation, coupled with a progressive degradation of these asperities. The sliding process is described by invoking the classical elastic-perfectly plastic formulation, whereas the degradation phenomenon, attributed to accumulated discontinuities in tangential components of velocity, reduces asperities' inclination and results in an unstable material response.

In general, the interface surface may be very irregular so that a significant bias in the spatial distribution of asperities orientation occurs. Such a bias can be described by employing the mathematical representation analogous to that in Pietruszczak and Krucinski (1989); i.e. defining the directional distribution of asperities orientation as an average, continuous measure expressed in terms of an

expansion based on symmetric traceless tensors. Here, a very simple conceptual framework, similar to that of Dowding et al. (1991), will be discussed based on a rather drastic geometric idealization. Firstly, the formulation will be restricted to a two-dimensional case, in which out-of-plane motion is not accounted for. Secondly, the interface surface will be idealized as consisting of a set of sawtooth asperities with uniform (in an average sense) inclination with respect to direction of the interface. Since the orientation is said to be uniform and the sliding process is governed by the ratio of normal and tangential components of the resultant force acting along each asperity, the problem can be reduced to considering the deformation resulting from sliding along a single 'representative' asperity. Note that the orientation of this asperity, defined by  $\alpha$ , may be generally different for sliding in two opposite directions.

### 2.6.2 Formulation of the interface model

Given the above assumptions, consider now the deformation process in the neighbourhood of the idealized interface. Introduce a local frame of reference  $\bar{x}$ , such that  $\bar{x}_2$ -axis is along the normal to the asperity (Fig. 2.10). If  $F = \{F_2, F_1\}^T$  is the resultant force acting at the interface, then

$$F = [T]\bar{F} \quad ; \quad [T] = \begin{bmatrix} \cos\alpha & \sin\alpha \\ -\sin\alpha & \cos\alpha \end{bmatrix} \quad (2.40)$$

where  $\bar{F} = \{\bar{F}_2, \bar{F}_1\}^T$  is the force transmitted through the asperity of orientation  $\alpha$ . A similar transformation rule applies to the displacement discontinuity vector  $g = \{g_2, g_1\}^T$ .

The sliding along the asperity is described in terms of an elastic-perfectly plastic formulation, in which the yield and plastic potential functions are selected as

$$f(\bar{F}) = |\bar{F}_1| + \eta \bar{F}_2 = 0 \quad ; \quad Q = |\bar{F}_1| = \text{const.} \quad (2.41)$$

with  $\eta = \text{const.}$  The consistency conditions reads

$$\dot{f} = \left( \frac{\partial f}{\partial \bar{F}} \right) \dot{\bar{F}} \quad ; \quad \dot{\bar{F}} = [T]^T \dot{F} + \left( \frac{\partial}{\partial \alpha} [T]^T F \right) \dot{\alpha} \quad (2.42)$$

Assume now that the flow rule and the evolution law for the asperities orientation take the form

$$\dot{\bar{g}}^p = \dot{\lambda} \frac{\partial Q}{\partial \bar{F}} \quad ; \quad \alpha = \alpha(\bar{g}_1^p) \quad (2.43)$$

Since, according to eq. (2.43), the degradation of asperities is affected only by irreversible deformations, the response in the elastic range can be defined as

$$\dot{F} = [k^e] (\dot{g} - \dot{g}^p) \quad ; \quad [k^e] = \begin{bmatrix} k_N & 0 \\ 0 & k_T \end{bmatrix} \quad (2.44)$$

where  $k_N$  and  $k_T$  represent the normal and shear elastic stiffnesses, respectively.

Substituting eq.(2.44) and eq.(2.43) in the consistency condition, eq.(2.42), and noting that

$$\dot{\alpha} = \frac{\partial \alpha}{\partial \bar{g}_1^P} \text{sign}(\bar{F}_1) \dot{\lambda}; \quad \dot{g}^P = [T] \dot{\bar{g}}_1^P + \left( \frac{\partial}{\partial \alpha} [T] \right) \bar{g}^P \dot{\alpha} \quad (2.45)$$

one obtains, after some transformations

$$\dot{\lambda} = \left( \frac{\partial f}{\partial F} \right)^T [T]^T [k^e] \dot{g} / H \quad (2.46)$$

where

$$H = H_1 + H_2; \quad H_1 = \left( \frac{\partial f}{\partial F} \right)^T [T]^T [k^e] [T] \frac{\partial Q}{\partial F}$$

$$H_2 = \left( \frac{\partial f}{\partial F} \right)^T [T]^T [k^e] \left( \frac{\partial}{\partial \alpha} [T] \right) \bar{g}^P \frac{\partial \alpha}{\partial \bar{g}_1^P} \text{sign}(\bar{F}_1) - \left( \frac{\partial f}{\partial F} \right)^T \left( \frac{\partial}{\partial \alpha} [T]^T \right) F \frac{\partial \alpha}{\partial \bar{g}_1^P} \text{sign}(\bar{F}_1) \quad (2.47)$$

It should be noted that since  $\partial \alpha / \partial \bar{g}_1^P < 0 \Rightarrow H < 0$  which leads to a locally unstable material response. Following a standard plasticity procedure, i.e. substituting eq. (2.43), eq. (2.45) and eq. (2.46) into eq. (2.44) and rearranging, one obtains

$$\dot{F} = [K] \dot{g}$$

$$[K] = [K^e] - \frac{[K^e] \left( [T] \frac{\partial Q}{\partial F} + \frac{\partial}{\partial \alpha} [T] \bar{g}^P \frac{\partial \alpha}{\partial \bar{g}_1^P} \text{sign}(\bar{F}_1) \right) \left( \frac{\partial f}{\partial F} \right)^T [T]^T [K^e]}{H} \quad (2.48)$$

where  $[K]$  is the elastoplastic stiffness ( $\det[K] < 0$ ) whose components are defined, in explicit terms, as

$$k_{11} = k_N - \frac{k_N^2}{H} (\eta \cos \alpha \operatorname{sign}(\bar{F}_1) + \sin \alpha) \left( \sin \alpha + g_1^P \frac{\partial \alpha}{\partial \bar{g}_1^P} \right) \quad (2.49a)$$

$$k_{12} = -\frac{k_N k_T}{H} (-\eta \sin \alpha \operatorname{sign}(\bar{F}_1) + \cos \alpha) \left( \sin \alpha + g_1^P \frac{\partial \alpha}{\partial \bar{g}_1^P} \right) \quad (2.49b)$$

$$k_{21} = -\frac{k_N k_T}{H} (\eta \cos \alpha \operatorname{sign}(\bar{F}_1) + \sin \alpha) \left( \sin \alpha - g_2^P \frac{\partial \alpha}{\partial \bar{g}_1^P} \right) \quad (2.49c)$$

$$k_{22} = k_T - \frac{k_T^2}{H} (-\eta \sin \alpha \operatorname{sign}(\bar{F}_1) + \cos \alpha) \left( \cos \alpha - g_2^P \frac{\partial \alpha}{\partial \bar{g}_1^P} \right) \quad (2.49d)$$

Finally, the degradation law for the orientation of asperities is assumed to be in a simple exponential form

$$\alpha = \alpha_0 \exp(-C \bar{g}_1^P) \quad (2.50)$$

where  $\alpha_0$  is the initial orientation and  $C$  is a material constant.

The constitutive law, presented above, relates the material rates of the resultant force acting at the interface to that of the displacement discontinuity. It

is apparent that given the unit cross-sectional area of the interface, eq.(2.48) can be expressed in the functional form consistent with eq.(2.23), thereby completing the mathematical formulation of the problem. It should be pointed out here that the material characteristics of the interface are, in general, identifiable from elementary material tests. Perhaps the most appropriate procedure is to fail an initially homogeneous sample in pure tension mode and subsequently identify the interface properties from a direct shear test.

### 2.6.3 Numerical simulations for the interface

In order to illustrate the performance of the model, the constitutive relation has been applied to simulate the results of a series of direct shear tests as reported by Schneider(1976). The tests have been conducted on hard-formed gypsum samples displaying natural joint morphology typical of a tension joint in granite. Based on experimental data, the following parameters have been selected  $\eta=0.82$ ,  $k_N = 40,000 \text{ MN/m}^3$ ,  $k_T = 50,000 \text{ MN/m}^3$

where  $k_N$  and  $k_T$  define the elastic moduli per unit cross-sectional area of the interface. The average inclination of the asperities was estimated ( based on the profiles provided in Schneider, 1976) as  $\alpha=9^\circ$ , whereas  $C=25 \text{ m}^{-1}$  was chosen to obtain the best fit approximation to the experimental characteristics.

The results of numerical simulations are presented in Fig. 2.11. Fig. 2.11a shows the shear stress-deformation curves corresponding to two different values of normal stress, whereas Fig. 2.11b gives the respective dilatancy profiles. The predictions appear to be in reasonable agreement with the experimental data, particularly with regard to the load-deformation characteristics.

It is interesting to note that, in the present formulation, the dilation reduces progressively to zero as the asperities degrade. On the other hand, if the convective term in the expression for the velocity discontinuity eq. (2.45) is dropped, which is equivalent to referring the flow rule to the global frame of reference, then the dilation approaches a constant value. This is shown in Fig. 2.12 which provides the respective volumetric characteristics. For both the cases, the shear characteristics (shown in Fig. 2.11b) remains identical.

## 2.7 Modelling of brittle response of concrete subjected to plane strain uniaxial compression

### 2.7.1 Implementation of the framework

For the implementation of the framework in point integration, two parameters, i.e. internal length parameter  $\mu$  and the interface strength parameter  $\eta$ , must be defined. The use of homogenization technique, viz, eq (2.22), implies that the macroscopic response of the sample is sensitive to the parameter  $\mu$ , defined in eq. (2.22). Within the context of plane strain configuration, the characteristic dimension  $\mu$  could be defined as  $(h \cos \beta)^{-1}$ , where  $h$  is the height of the sample and  $\beta$  defines the orientation of interface. Thus, even though the macroscopic response is invariant with respect to the thickness of the interface, it depends explicitly on the height of the sample. It should be point out that the interface (macrocrack), once formed, constitutes a physical plane of weakness within the intact material. Thus, its orientation is assumed to be fixed upon the onset of localization. This does not preclude the possibility that for deformation histories experiencing large stress reversals, additional macrocracks may develop

within the same representative volume. Regarding the strength parameter  $\eta$ , it should be noted that it could be determined directly from the bifurcation analysis.

### 2.7.2 Numerical simulations

The complete formulation has been applied to extend the predictions of plane strain uniaxial compression tests (Fig. 2.8) to the post-localized regime (Fig. 2.13). The simulations have been carried out using the following set of interface parameters:

$$k_T = 40,000 \text{ MN/m}^3, k_N = 50,000 \text{ MN/m}^3, \alpha = 10^\circ, C = 200 \text{ m}^{-1}.$$

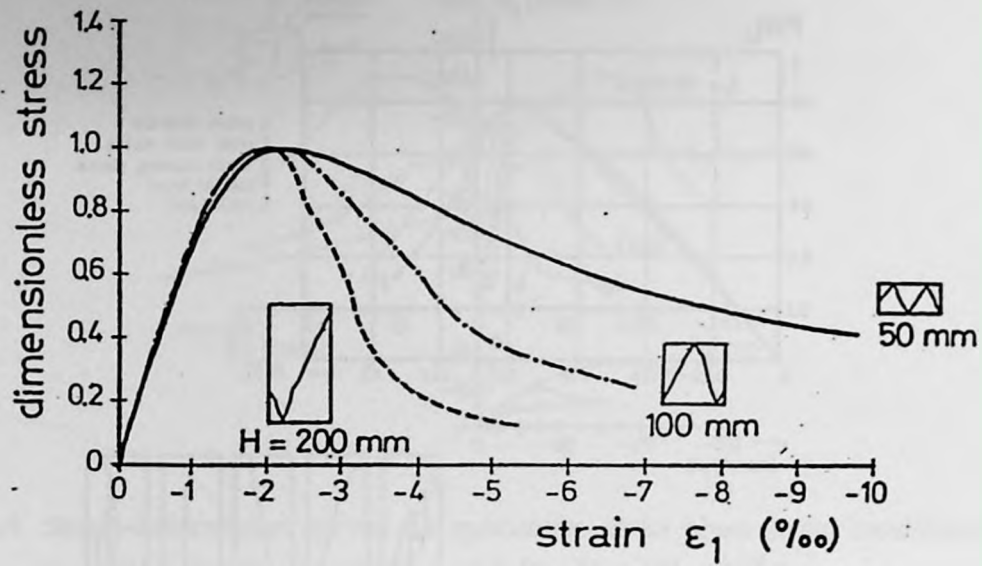
The above choice is again arbitrary as no adequate experimental data is available. Thus, the objective here is to investigate the qualitative trends of the response as predicted by the present formulation.

The results of numerical analysis are presented in Fig. 2.13a and Fig. 2.13b. The rate of strain softening, Fig. 2.13a, is virtually insensitive to the initial confining pressure. This is a rather debatable issue. It should be noted, however, that such a sensitivity, if indeed present, can be easily accounted for by a simple modification of the degradation law eq.(2.50) (i.e., assuming that the value  $C$  is affected by  $F_2$ ). Overall, the qualitative aspects, including the nature of volumetric profiles, appear to be consistent with experimental data in Fig. 2.4. Finally, Fig. 2.14 presents the mechanical characteristics for two samples of  $h=0.1\text{m}$  and  $h=0.2\text{m}$  subjected to the same loading history. In particular, the average rate of strain softening progressively increases with the height of the specimen, which is consistent with experimental data in Fig. 2.1. The deformation mode, as observed macroscopically, is strongly anisotropic, i.e. the

reduction in the vertical stress is accompanied by significant distortions, which is evident from Fig. 2.14c.

In general, the proposed framework gives a reasonable description of localized deformation, including the inception of localized mode, orientation of discontinuity plane and the unstable post-peak response. In particular, the height effect and the anisotropy of the deformation process can be accounted for.

(a)



(b)

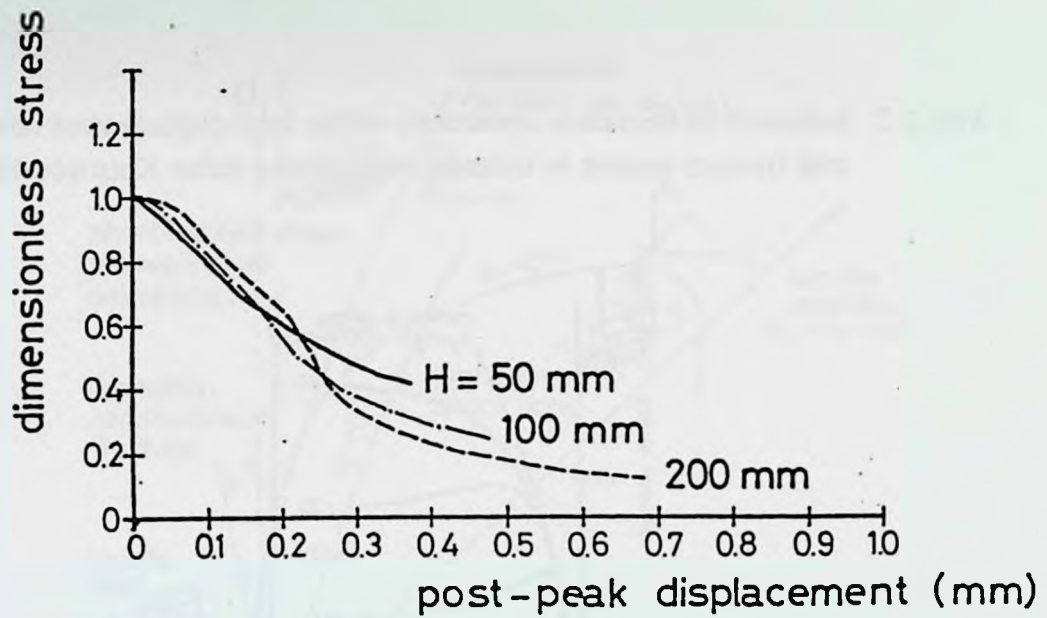


Fig. 2.1 Influence of the specimen height on fracture characteristics in uniaxial compression (after Van Mier, 1984)

(a) stress-strain curve and corresponding fracture pattern;

(b) post-peak stress-displacement curve.

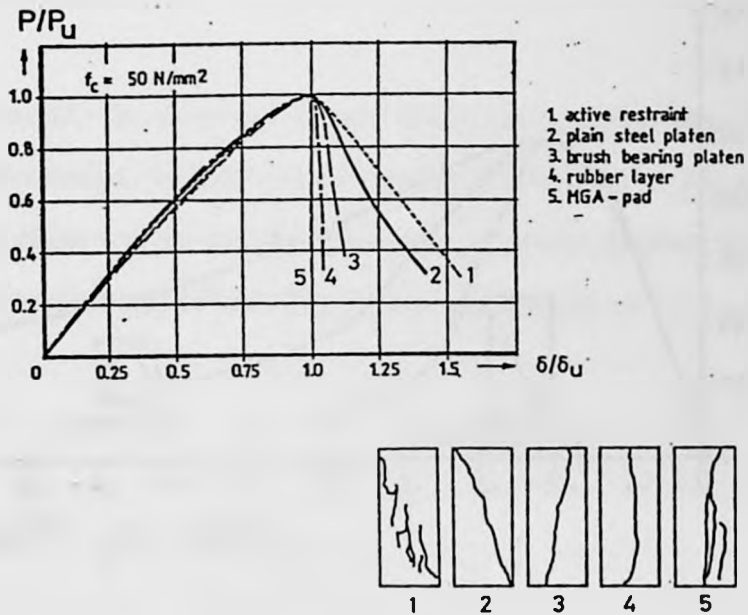


Fig. 2.2 Influence of boundary constraints on the load-displacement behaviour and fracture pattern in uniaxial compression (after Kotsovos 1983)

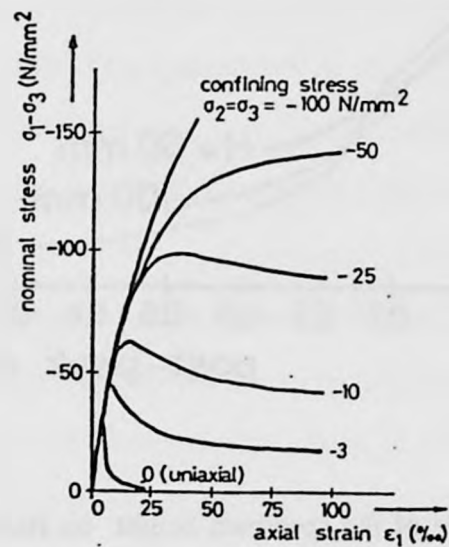


Fig. 2.3 Nominal stress versus axial strain curves obtained in displacement controlled standard triaxial compression tests (after Jamet et al. 1984)

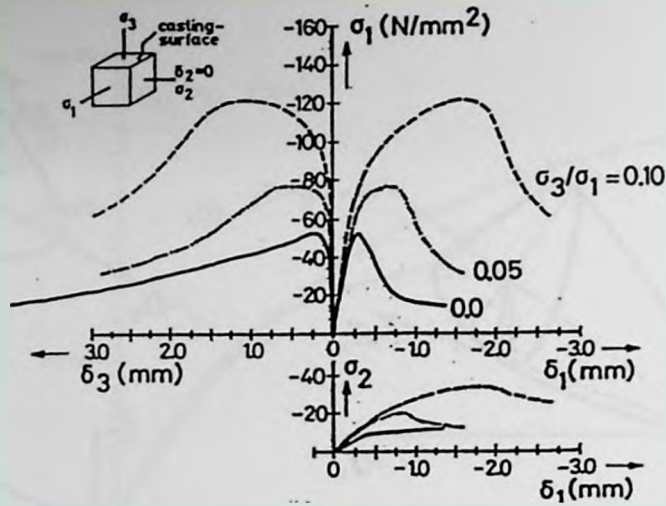


Fig.2.4 Stress-deformation curves for specimens under plane strain conditions at various levels of confinement (after Van Mier 1984)

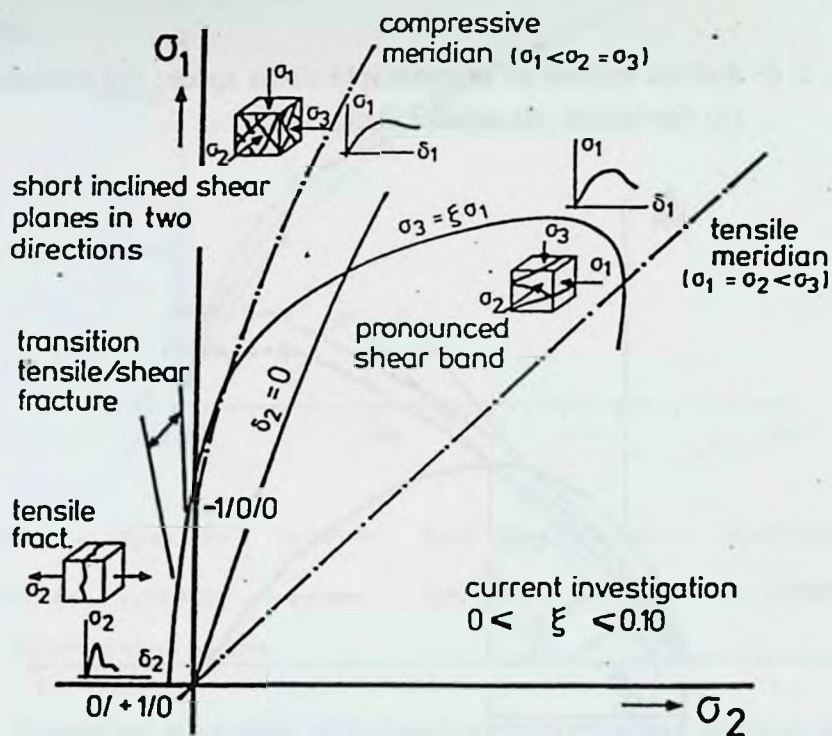


Fig. 2.5 Classification of fracture modes (after Van Mier 1984)

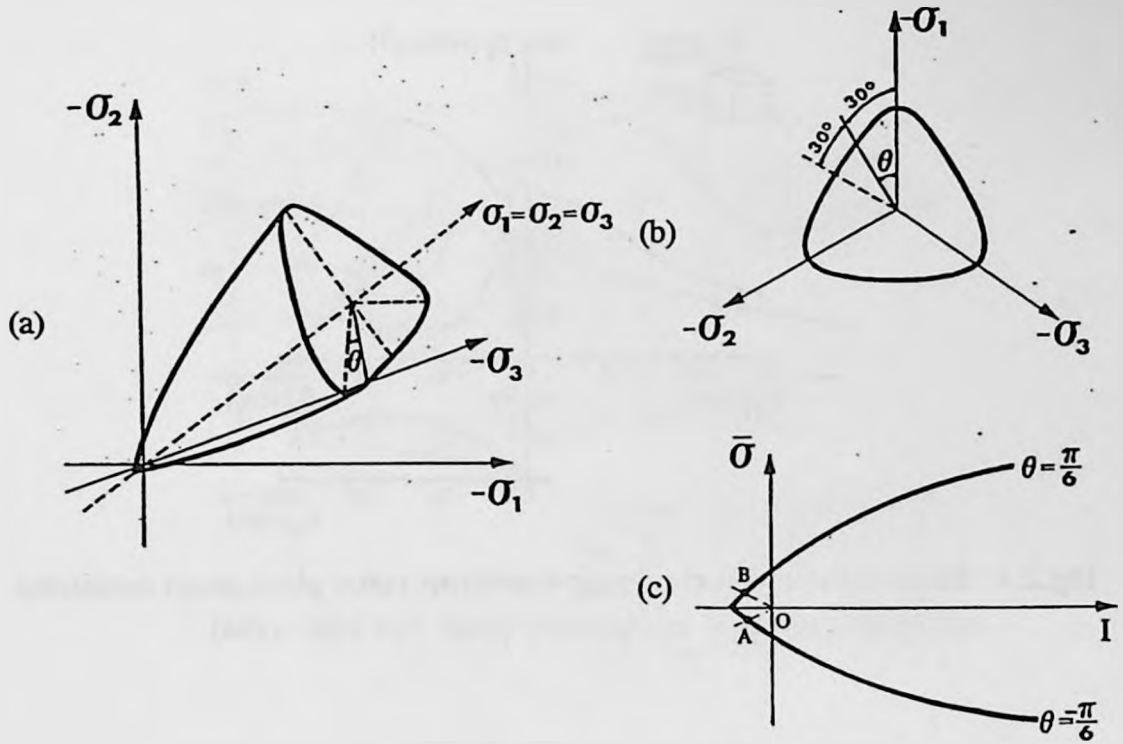


Fig. 2.6 Failure surface in (a) principle stress space; (b) meridional plane; (c) deviatoric plane(after Jiang 1988).

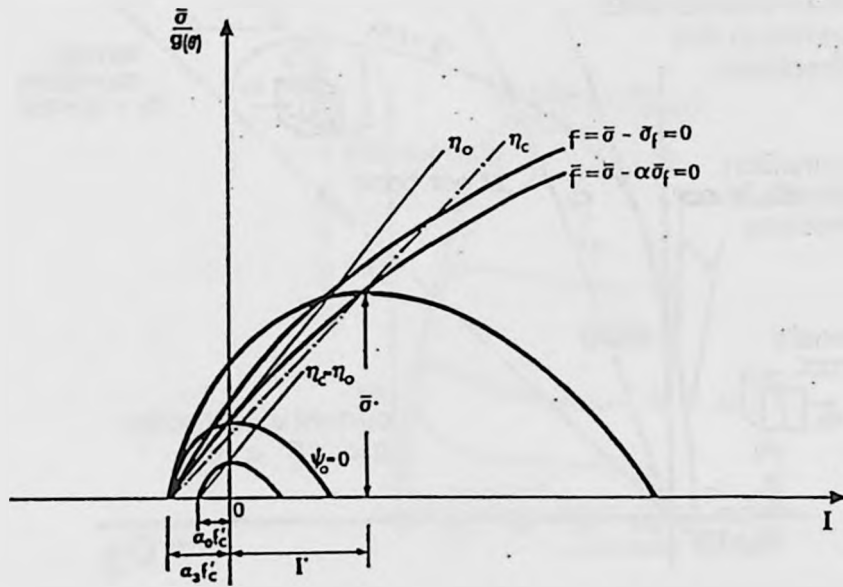


Fig. 2.7 Plastic potential surface in meridional plane(after Jiang 1988)

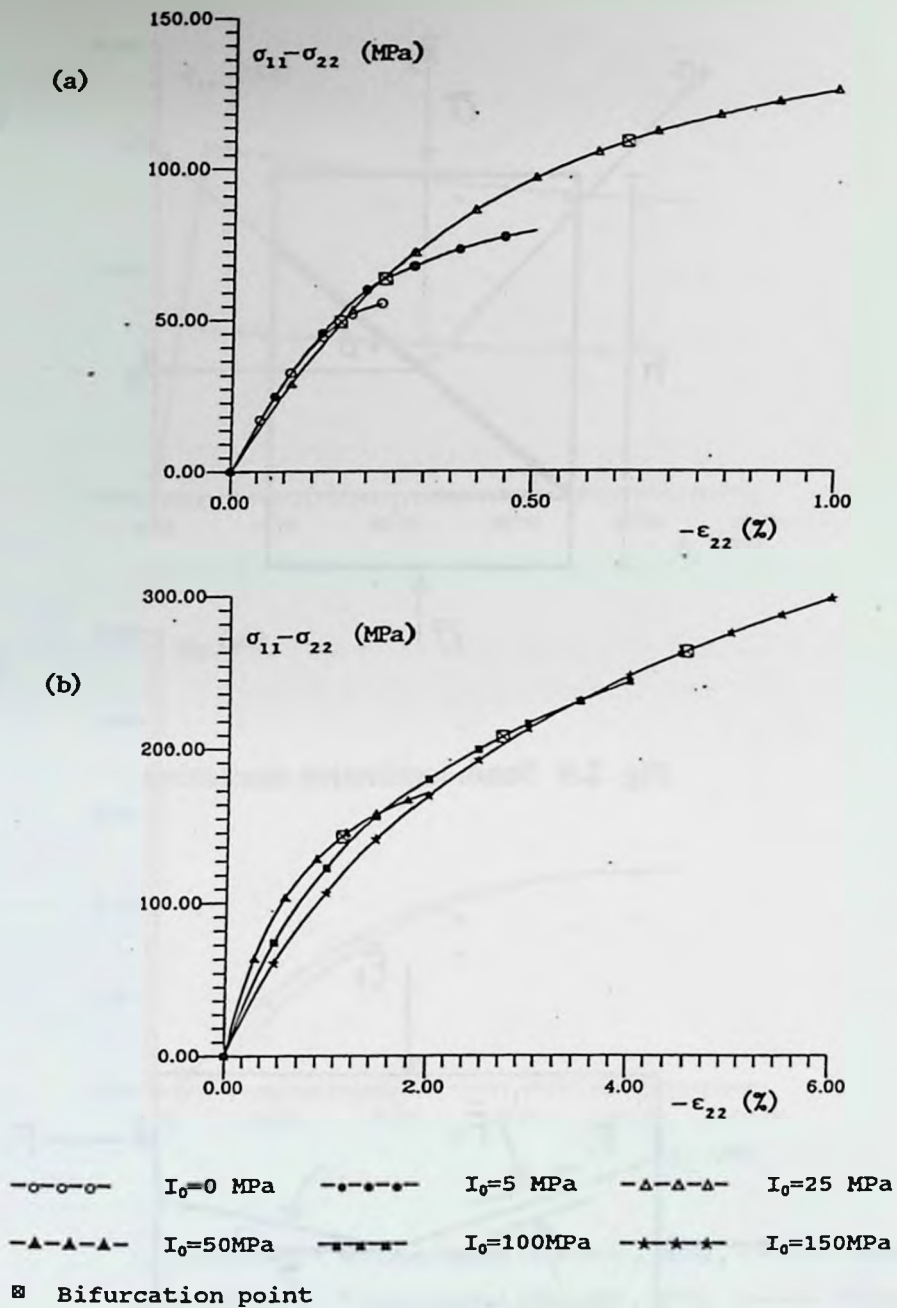


Fig. 2.8 Numerical simulation of a ductile-brittle transition in plane strain uniaxial compression (a) Initial confining pressure 0, 5 and 25 MPa; (b) Initial confining pressure 50, 100 and 150 MPa.

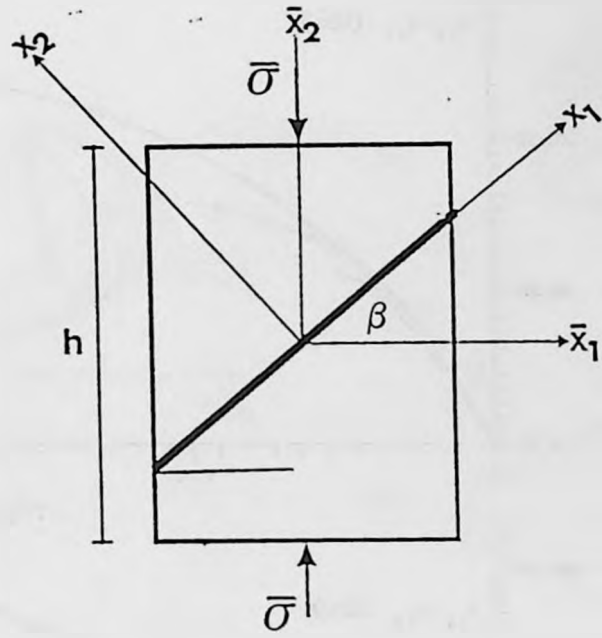


Fig. 2.9 Strain localization mechanism

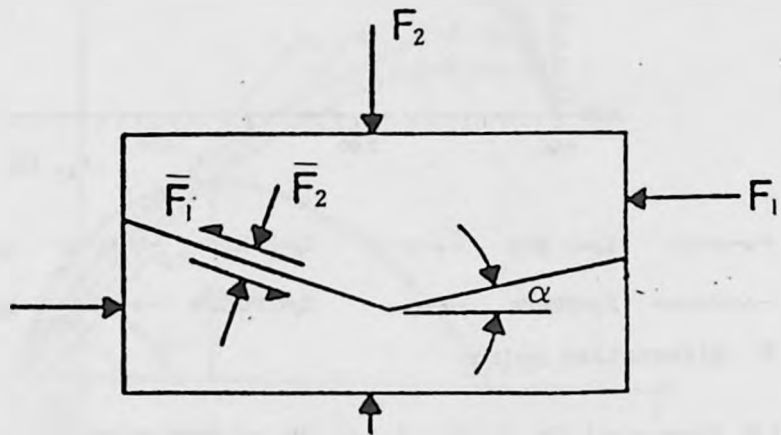


Fig. 2.10 Interface with asperities

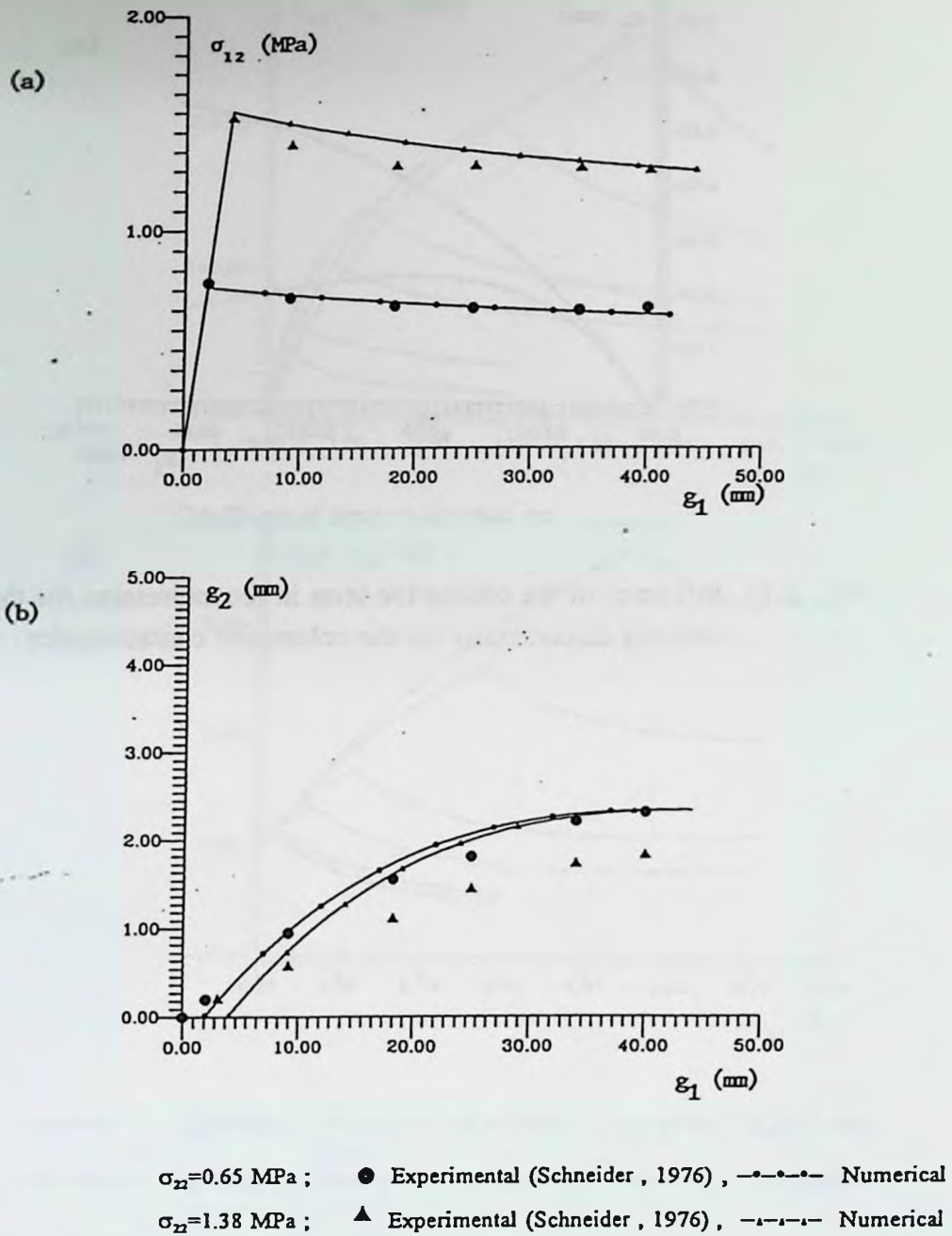


Fig. 2.11 Response of hard-formed gypsum joints subjected to direct shear  
 (a) shear characteristics; (b) volumetric characteristics.

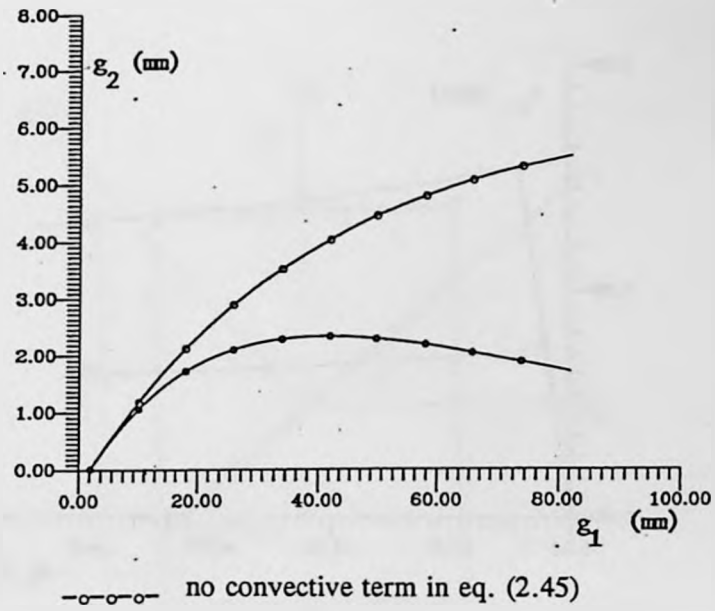


Fig. 2.12 Influence of the convective term in the expression for the velocity discontinuity on the volumetric characteristics

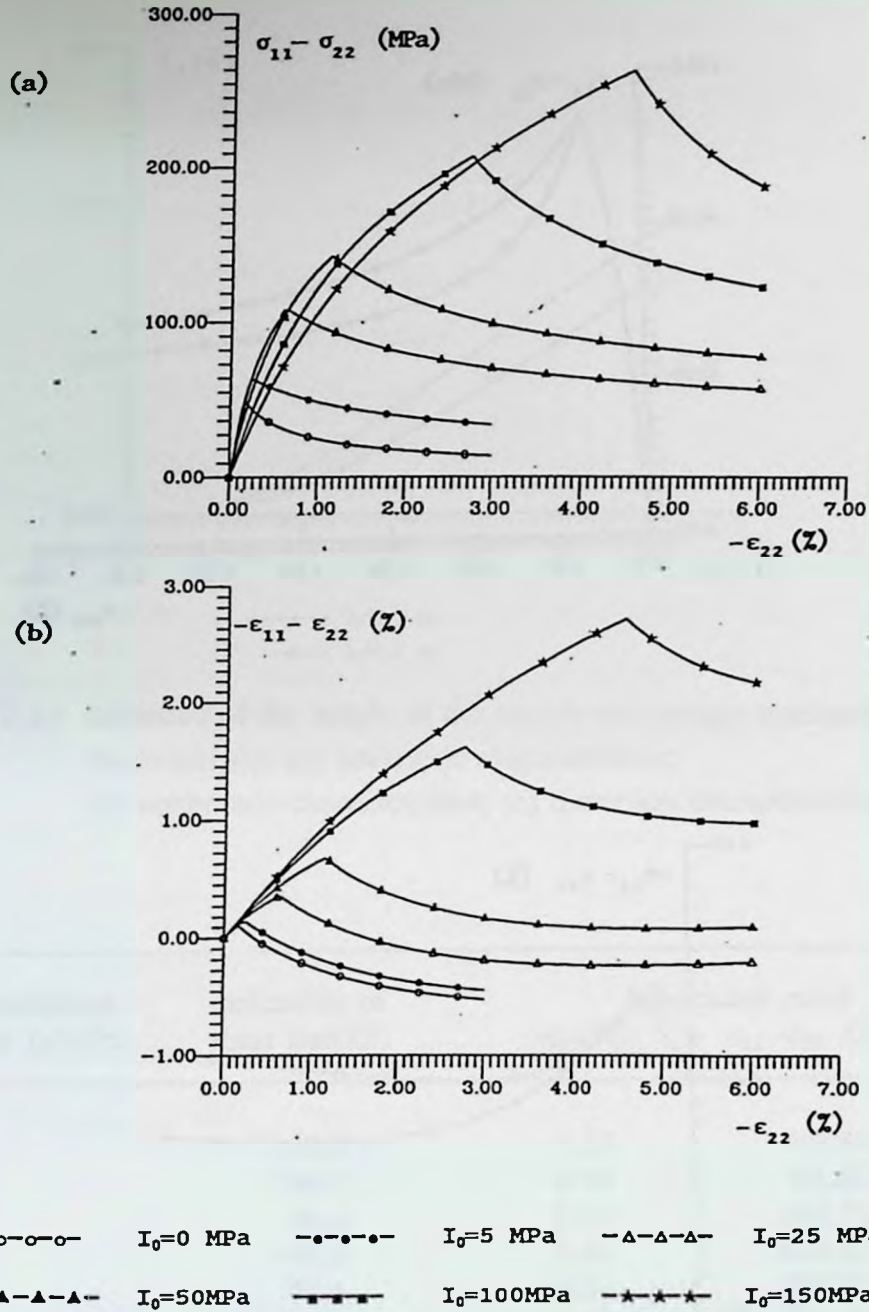
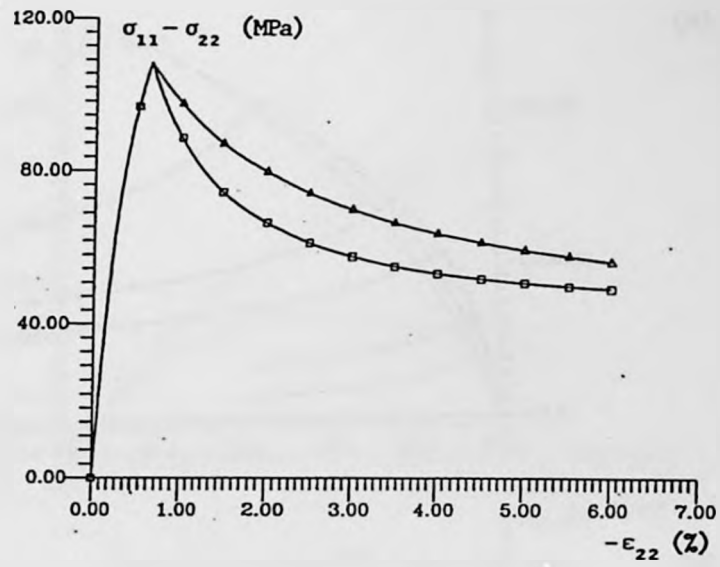
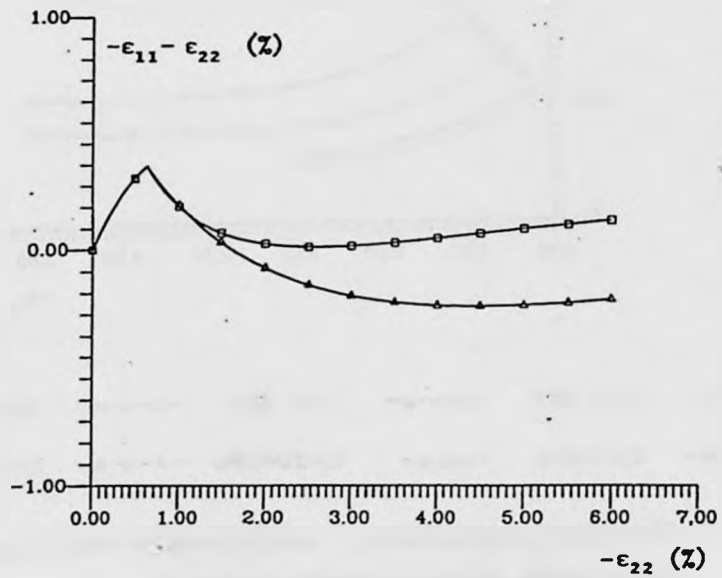


Fig. 2.13 Numerical simulations of unstable response for a series of plane strain uniaxial compression tests  
 (a) deviatoric characteristic; (b) volumetric characteristics.

(a)



(b)



(c)

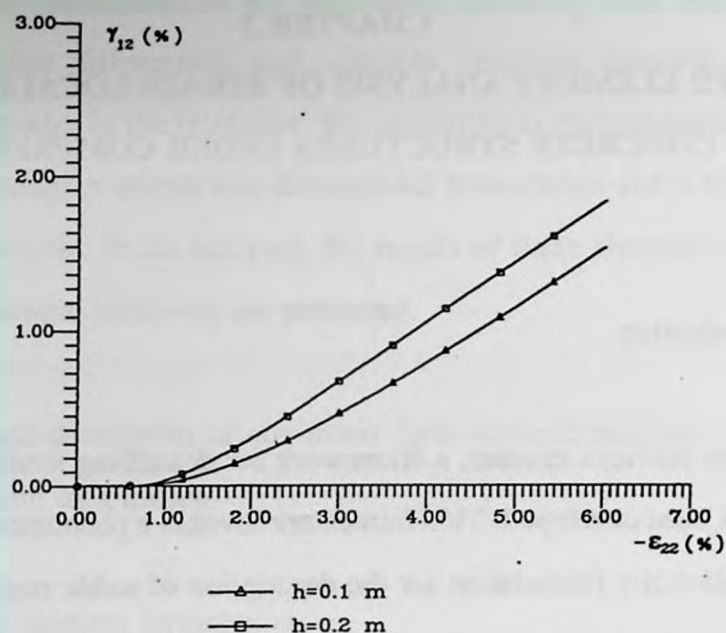


Fig. 2.14 Influence of the height of the sample on average mechanical characteristics (a) deviatoric characteristics; (b) volumetric characteristics; (c) distortion characteristics.

initial confining pressure $I_0$ (MPa)	inclination of shear band( $\beta$ )	bifurcation point	
		$-\epsilon_{22}$ (%)	$\sigma_{11} - \sigma_{22}$ (MPa)
0	56.2	0.18	49.38
5	54.2	0.26	63.63
25	50.0	0.65	108.71
50	48.0	1.16	142.61
100	46.5	2.74	207.21
150	45.5	4.54	263.10

Table 2.1 Results of bifurcation analysis for plane strain uniaxial compression tests

**CHAPTER 3**  
**FINITE ELEMENT ANALYSIS OF STRAIN LOCALIZATION**  
**IN CONCRETE STRUCTURES UNDER COMPRESSION**

3.1 Introduction

In the previous chapter, a framework for describing strain localization in concrete has been developed. This framework invokes a phenomenological strain-hardening plasticity formulation for the description of stable response associated with the growth of microcracks, a path-dependent bifurcation criterion for the transition to unstable response and a non-standard continuum formulation for localized deformation based on a homogenization technique.

In order to analyze a boundary value problem, the proposed framework needs to be implemented within a finite element algorithm. The objectives of this chapter are to describe the main features of the implementation procedure and to apply this approach for the analysis of some structural problems involving compression-shear as a predominant failure mode.

This chapter is divided into four parts. The first part presents the general description of non-linear finite element analysis of strain localization, which includes the basic formulation of the finite element method and the general

solution algorithm for a non-linear system. The second part describes the numerical implementation of the framework including both stages, i.e. stable response before bifurcation and unstable response associated with strain localization mode. In the third part, the sensitivity to finite element discretization is studied through a simple one-dimensional formulation and a two-dimensional numerical analysis. In the last part, the results of finite element simulations of a series of structural problems are presented.

### 3.2 General description of non-linear finite element analysis of strain localization

#### 3.2.1 Finite element formulation

The finite element formulation is commonly derived based on the principle of virtual work. Consider the solid, in which the stresses  $\sigma_{ij}$ , the distributed body forces  $b_i$  and boundary tractions  $t_i$  form an equilibrating field. Let the body undergo virtual displacements  $\delta u_i$  which result in compatible strains  $\delta \epsilon_{ij}$ . Then the principle of virtual work (Zienkiewicz, 1989) requires that

$$\int_{\Omega} \sigma_{ij} \delta \epsilon_{ij} d\Omega = \int_{\Omega} b_i \delta u_i d\Omega + \int_{\Gamma_t} t_i \delta u_i d\Gamma_t \quad (3.1)$$

where  $\Omega$  is the domain of interest,  $\Gamma = \Gamma_t + \Gamma_u$ , where  $\Gamma_t$  is that part of the boundary on which boundary tractions are prescribed and  $\Gamma_u$  is a part of the boundary on which boundary displacements are given. In a matrix form, eq. (3.1) becomes

$$\int_{\Omega} \{ \delta \epsilon \}^T \{ \sigma \} d\Omega = \int_{\Omega} \{ \delta u \}^T \{ b \} d\Omega + \int_{\Gamma_t} \{ \delta u \}^T \{ t \} d\Gamma, \quad (3.2)$$

The normal finite element discretization procedure leads to the following relations between the displacements  $\{u\}$  and the displacement vector  $\{U\}$  of nodal points

$$\{ u \} = [N] \{ U \} \quad ; \quad \{ \delta u \} = [N] \{ \delta U \} \quad (3.3)$$

where  $[N]$  is the usual matrix of the displacement interpolation (shape) functions.

For a geometrically linear analysis, the strains can be defined as

$$\begin{aligned} \{ \epsilon \} &= [L] \{ u \} = [L] [N] \{ U \} = [B] \{ U \} \\ \{ \delta \epsilon \} &= [B] \{ \delta U \} \quad ; \quad [B] = [L] [N] \end{aligned} \quad (3.4)$$

where  $[L]$  is the differential operator matrix and  $[B]$  is the strain-displacement matrix. Substituting eqs. (3.3) and (3.4) into eq. (3.2), gives

$$\int_{\Omega} \{ \delta U \}^T [B]^T \{ \sigma \} d\Omega = \int_{\Omega} \{ \delta U \}^T [N]^T \{ b \} d\Omega + \int_{\Gamma_t} \{ \delta U \}^T [N]^T \{ t \} d\Gamma, \quad (3.5)$$

where the integrations are the sums of the individual element contributions. Since the expression eq.(3.5) must hold true for arbitrary virtual displacements, the following governing equations are obtained

$$\int_{\Omega} [B]^T \{ \sigma \} d\Omega = \int_{\Omega} [N]^T \{ b \} d\Omega + \int_{\Gamma_t} [N]^T \{ t \} d\Gamma, \quad (3.6)$$

or

$$\int_{\Omega} [B]^T \{ \sigma \} d\Omega - \{ R \} = 0 \quad (3.7)$$

Where  $\{R\}$  is the equivalent external force acting at the nodal points.  
Alternatively,

$$\{ R \} = \int_{\Omega} [N]^T \{ b \} d\Omega + \int_{\Gamma_t} [N]^T \{ t \} d\Gamma, \quad (3.8)$$

Since the proposed constitutive relation is path dependent, an incremental analysis is required. Assuming that the solution has been reached at the (m)th step, corresponding to the load increment  ${}^{m+1}\{\Delta R\}$  at (m+1)th step, one has

$$\begin{aligned} {}^{m+1}\{ R \} &= {}^m\{ R \} + {}^{m+1}\{ \Delta R \} \\ {}^{m+1}\{ U \} &= {}^m\{ U \} + {}^{m+1}\{ \Delta U \} \\ {}^{m+1}\{ \sigma \} &= {}^m\{ \sigma \} + {}^{m+1}\{ \Delta \sigma \} \end{aligned} \quad (3.9)$$

Thus, eq. (3.7) becomes

$$\begin{aligned} {}^{m+1}\{ F \} &= {}^{m+1}\{ R \} \\ {}^{m+1}\{ F \} &= \int_{\Omega} [B]^T {}^{m+1}\{ \sigma \} d\Omega \end{aligned} \quad (3.10)$$

where  $\{F\}$  is the equivalent force acting at the nodal points, or

$$\int_{\Omega} [B]^T {}^{m+1}\{ \Delta \sigma \} d\Omega = {}^{m+1}\{ R \} - \int_{\Omega} [B]^T {}^m\{ \sigma \} d\Omega \quad (3.11)$$

Two separate algorithms are required for solving eq. (3.11) (Bathe, 1982) (Chen, 1988). One is the algorithm used for solving a system of non-linear simultaneous equations, which is discussed in the following. Another is the numerical scheme for integration of the constitutive equation, i.e. for determining the stress increment  $\{\Delta\sigma\}$  corresponding to strain increment  $\{\Delta\epsilon\}$  for a given stress state and deformation history. This will be briefly described in section 3.3.

### 3.2.2 Numerical algorithm for solving non-linear equations

Many algorithms, such as initial stiffness method, (modified) Newton-Raphson method, the quasi-Newton method, etc., have been developed for solving a system of non-linear simultaneous equations. There are various arguments concerning the limitations and numerical efficiency of each of these algorithms, especially for the case of strain softening. Given the fact that the tangential stiffness operator may become singular or ill-conditioned, one may argue that the initial stiffness method or the quasi-Newton algorithm are more suitable than the Newton-Raphson technique. This may be true for the case of standard constitutive laws, with associated flow, incorporating some explicitly defined strain softening functions. However, the proposed formulation is derived based on the average mechanical response of a composite material (matrix and interface), which remains strongly anisotropic. Thus, the initial stiffness algorithm may numerically diverge soon after bifurcation, since the actual tangential stiffness is far from the trial isotropic elastic operator. At the same time, the quasi-Newton method is efficient only when the tangential stiffness is symmetric (Borja and Lee, 1990, Borja, 1991). Therefore, the Newton-Raphson technique seems to be the most appropriate for the implementation of the proposed

constitutive model. The relevant details of this approach are given below.

Considering that the stress  $\{\sigma\}$  is a non-linear function of the displacement  $\{U\}$ , eq. (3.10) can be rewritten as

$$\Psi(\{U\}) = F(\{U\}) - \{R\} \quad (3.12)$$

The solution to eq.(3.12) may be obtained using an iterative scheme. Assume that the  $(i-1)$ th approximation,  $\{U\}^{(i-1)}$ , to the displacement  $\{U\}$  is known. Expanding  $\Psi(\{U\})$  using the Taylor series expansion at  $\{U\}^{(i-1)}$  and neglecting all higher-order terms, one obtains

$$\Psi(\{U\}^{(i-1)}) + \frac{\partial \Psi}{\partial U} \bigg|_{\{U\}^{(i-1)}} (\{U\} - \{U\}^{(i-1)}) = 0 \quad (3.13)$$

or

$$\frac{\partial F}{\partial U} \bigg|_{\{U\}^{(i-1)}} \{\Delta U\}^{(i)} + \{F\}^{(i-1)} - \{R\} = 0 \quad (3.14)$$

where

$$\begin{aligned} \{\Delta U\}^{(i)} &= \{U\}^{(i)} - \{U\}^{(i-1)} \\ \{F\}^{(i-1)} &= F(\{U\}^{(i-1)}) \end{aligned} \quad (3.15)$$

Recognizing that

$$\{K_T\}^{(i-1)} = \frac{\partial F}{\partial U} \bigg|_{\{U\}^{(i-1)}} = \int_{\Omega} [B]^T [D] [B] d\Omega \quad (3.16)$$

where  $[D]$  is the material stiffness matrix corresponding to the displacement  ${}^{m+1}\{U\}^{(i-1)}$ , and  ${}^{m+1}\{K\}^{(i-1)}$  is the tangential stiffness of the structure, the Newton-Raphson scheme is obtained as

$$\begin{aligned} {}^{m+1}[K_T]^{(i-1)} {}^{m+1}\{\Delta U\}^{(i)} &= {}^{m+1}\{R\}^{(i)} - {}^{m+1}\{F\}^{(i-1)} \\ {}^{m+1}\{U\} &= {}^{m+1}\{U\}^{(i-1)} + {}^{m+1}\{\Delta U\}^{(i)} \end{aligned} \quad (3.17)$$

It should be noted that sufficient accuracy may be achieved by using small loading increments without iteration. In that case, the above procedure can be simplified by eliminating the iteration index

$$\begin{aligned} {}^m[K_T] {}^{m+1}\{\Delta U\} &= {}^{m+1}\{R\} - {}^m\{F\} \\ {}^{m+1}\{U\} &= {}^m\{U\} + {}^{m+1}\{\Delta U\} \end{aligned} \quad (3.18)$$

### 3.3 Numerical integration of the constitutive equations

As discussed in Section 3.2, at every iteration step, the stress  ${}^{m+1}\{\sigma\}^{(i)}$  corresponding to the displacements  ${}^{m+1}\{U\}^{(i)}$  should be computed using a constitutive relation, and subsequently the equivalent force,  ${}^{m+1}\{F\}^{(i)}$ , is calculated using eq. (3.10). The integration of eq. (3.11) is then performed over each element of the structure, using the Gaussian integration technique. Thus, the stresses are computed at all Gaussian sampling points of the structure at each iteration step. Since the constitutive relation after bifurcation is different from the that before bifurcation, both cases will be considered separately.

### 3.3.1 Numerical implementation of the constitutive model before bifurcation

In a typical loading step, say the  $(m+1)$ th step, one has already obtained the converged solutions for stress and strain,  ${}^m\{\sigma\}$ ,  ${}^m\{\epsilon\}$  and the hardening parameter  ${}^m\xi$  at  $m$ th load step. At an iteration step  $i$ , in the  $(m+1)$ th load step, the  $i$ th approximation of the displacement,  ${}^{m+1}\{U\}^{(i)}$ , has also been obtained. The following procedure has been used for the stress calculation.

- (i) Compute the strain increment and the trial stress increment assuming an elastic behaviour.

$$\begin{aligned} {}^{m+1}\{\epsilon\}^{(i)} &= [B] {}^{m+1}\{U\}^{(i)} ; \quad \{\Delta\epsilon\} = {}^{m+1}\{\epsilon\}^{(i)} - {}^m\{\epsilon\} \\ \{\Delta\sigma^e\} &= [D^e] \{\Delta\epsilon\} ; \quad {}^{m+1}\{\sigma\}^{(i)} = {}^m\{\sigma\} + \{\Delta\sigma^e\} \end{aligned} \quad (3.19)$$

- (ii) Determine the loading state. Three cases should be considered:

(a) If  $f({}^{m+1}\{\sigma\}, {}^m\xi) < 0$ , only elastic deformations occur and the process is ended without further calculation of plastic deformations. Go to step (v);

(b) If  $f({}^{m+1}\{\sigma\}, {}^m\xi) > 0$  and  $f({}^m\{\sigma\}, {}^m\xi) = 0$ , the plastic deformations is said to continue;

(c) If  $f({}^{m+1}\{\sigma\}, {}^m\xi) > 0$  and  $f({}^m\{\sigma\}, {}^m\xi) < 0$ , a transition from elastic state to elastic-plastic state takes place.

For the case (c), there exists a scaling factor  $r$  such that  $f({}^m\{\sigma\} + r\{\Delta\sigma^e\}, {}^m\xi) = 0$ . The following iteration scheme is employed to estimate  $r$ . The first trial value  $r_1$  of  $r$  may be obtained by a linear interpolation in  $f$ , i.e.

$$r = r_1 = -f_0 / (f_1 - f_0) \quad (3.20)$$

A improved estimation of  $r$  can be obtained by utilizing the consistency condition. For an instantaneous position of yield surface, the change in the yield function can be expressed as

$$df = \left\{ \frac{\partial f}{\partial \sigma} \right\}^T \{ d\sigma \} \quad (3.21)$$

Assuming the following relations,

$$\{ d\sigma \} = \Delta r_1 \{ \Delta \sigma^e \} \quad ; \quad df = -f_2 \quad (3.22)$$

and substituting eq. (3.22) into eq. (3.21), leads to an improved estimation of  $r$

$$r = r_1 - \frac{f_2}{\left\{ \frac{\partial f}{\partial \sigma} \right\}^T \{ \Delta \sigma^e \}} \quad ; \quad f_2 = -\Delta r_1 \left\{ \frac{\partial f}{\partial \sigma} \right\}^T \{ \Delta \sigma^e \} \quad (3.23)$$

(iii) Compute the subincrement of strain.

$$\{ d\epsilon \} = \{ \Delta \bar{\epsilon} \} = (1-r) \{ \Delta \epsilon \} / m \quad (3.24)$$

(iv) Integrate numerically from loop subincrement one to  $m$ th and check the bifurcation criterion.

For each subincrement, the explicit technique (Euler forward method) has been employed. This consists of determining the plastic strain subincrement, then

computing the stress subincrement and finally updating stresses, strains and the hardening parameters. Since many approximations have been incorporated in the numerical integration scheme, the consistency condition is often violated. A special procedure developed by Nayak et al (1972) can be applied to bring the stresses back along the normal to the yield surface. The assumption that the stress correction is in the direction of the gradient of the yield function gives,

$$\{ \Delta \sigma \} = \zeta \left\{ \frac{\partial f}{\partial \sigma} \right\} \quad (3.25)$$

where  $\zeta$  is a scalar quantity and  $\{ \Delta \sigma \}$  is the stress correction vector. Substituting eq. (3.25) into eq. (3.21) ( i.e. consistency conditions) and noting that  $df=0-f_1$  (the value  $f$  outside the yield surface) results in

$$-f_1 = \left\{ \frac{\partial f}{\partial \sigma} \right\}^T \left\{ \frac{\partial f}{\partial \sigma} \right\} \zeta \quad (3.26)$$

Solving for  $\zeta$  from the above equation and substituting the result back to eq.(3.25) yields

$$\{ \Delta \sigma \} = - \frac{f_1 \left\{ \frac{\partial f}{\partial \sigma} \right\}}{\left\{ \frac{\partial f}{\partial \sigma} \right\}^T \left\{ \frac{\partial f}{\partial \sigma} \right\}} \quad (3.27)$$

Since the vector  $\{ \partial f / \partial \sigma \}$  is calculated based on the stress state outside the yield surface, it is not exactly normal to the yield surface. Therefore, a number of successive approximations are obtained using eq. (3.27) until the stress correction falls within a prescribed tolerance defined by absolute value of  $(df)$ .

It should be noted that, in the finite element scheme, the bifurcation criterion eq.(2.18), associated with the loss of ellipticity of the governing equilibrium equations, is assessed in a discrete sense. Thus, the bifurcation criterion is checked for every Gaussian point during the integration process. Theoretically, if eq.(2.18) is satisfied, two conjugate shear band orientations are obtained. In general, one can postulate that the direction which is compatible with the current displacement field will prevail. The mathematical criterion, as suggested by Pietruszczk and Niu (1993), is based on choosing the orientation which minimizes the product  $\mathbf{u}^T \mathbf{n}$  for all possible  $\mathbf{n}$ 's, where  $\mathbf{u}$  is the displacement vector at a given Gauss point and  $\mathbf{n}$  defines the normal to the shear band.

- (v) Update the stiffness matrix, stresses and hardening parameters and memorize the bifurcation index.

### 3.3.2 Numerical integration of constitutive equations after the onset of localization

The implementation of the homogenization technique in the finite element code requires appropriate estimates for the dimension  $\mu$  in eq.(2.22). In the displacement formulation, the stress field is assessed in a discrete manner, so that the equations of equilibrium are satisfied in an average sense only. Therefore, it is perhaps most appropriate to estimate the value of  $\mu$  in an average manner as well, especially that the precise location of the localized band within the element is unknown.

Using a typical two-dimensional numerical integration scheme, the area of the element can be partitioned according to

$$\begin{aligned}
 A &= \int_A dA \\
 &= \int_{-1}^1 \int_{-1}^1 \det[J] d\xi d\zeta = \sum_{i=1}^{NINT} \sum_{j=1}^{NINT} w_i w_j (\det[J])_{ij} = \sum_{i=1}^{NINT} \sum_{j=1}^{NINT} (A)_{ij} \quad (3.28)
 \end{aligned}$$

where  $\xi$  and  $\zeta$  are the co-ordinates of a reference co-ordinate system,  $[J]$  is the Jacobian of the transformation between the reference and the physical co-ordinate system and  $i, j$  and  $w$ 's are the integration points and weights, respectively for a particular quadrature rule. The procedure can be used for the one point, 2x2 and alternate quadrature schemes, providing the partitioned area  $(A)_{ij}$  associated with each integration point.

The estimates of  $\mu$ , for an integration point, could be established by defining a characteristic dimension of the partitioned area  $h$ . The simplest approximation is the formula employed by Pietruszczak and Mroz (1980) and Belytscho et al. (1986)

$$h = \sqrt{(A)_{ij}} \quad ; \quad (A)_{ij} = w_i w_j \det[J]_{ij} \quad (3.29)$$

In such a case  $\mu = (h \cos \beta)^{-1}$ , where  $\beta$  defines the inclination of the shear band with respect to the physical co-ordinate system chosen. It is apparent that a conceptually similar procedure can be employed in a three-dimensional case, by partitioning the volume of the element according to a three-dimensional numerical

integration scheme. The above approximation is certainly the simplest one and some alternative procedures may be developed for estimating  $\mu$ . It should be stressed however, that the proposed partitioning rule is quite general and can be easily be implemented within the context of any type of discretization.

The value of  $\mu$  estimated by the above approach, should be kept unchanged during the stress calculation process. The stress calculation procedure is based on integration of eq.(2.25). The latter is complicated by the fact that some a priori assumptions have to be made regarding active loading/unloading conditions in both constituents. Once the solution has been obtained, appropriate loading criteria need to be verified. If one of those is violated, the initial assumptions must be revised and the calculation procedure repeated. In general, the alternative formulation provided in Chapter 2 viz, eq.(2.41) results in a simpler and more versatile integration scheme, especially, within the context of complex loading histories. This integration procedure, based on eq.(2.41), is briefly described below.

- (i) Compute the strain increment and then the trial stress increment assuming an elastic behaviour of the composite (use [D] based on eq.(2.35)).
- (ii) Determine the loading state. Four cases should be considered:
  - (a) If  $f^{(1)}(\sigma^{m+1}, \xi) < 0$  and  $f^{(2)}(\sigma^{m+1}, \xi) < 0$  only the elastic deformation occurs and process is ended without further calculations of plastic strain. Go to step (iv).
  - (b) If  $f^{(1)}(\sigma^{m+1}, \xi) > 0$  and  $f^{(2)}(\sigma^{m+1}, \xi) > 0$ , the plastic deformation in both constituents (matrix and interface) occurs.

(c) If  $f^{(1)}(\sigma^{m+1}, \xi^m) > 0$  and  $f^{(2)}(\sigma^{m+1}, \xi^m) < 0$  the active loading is restricted to matrix material whereas the interface undergoes elastic deformation.

(d) If  $f^{(1)}(\sigma^{m+1}, \xi^m) < 0$  and  $f^{(2)}(\sigma^{m+1}, \xi^m) > 0$ , the plastic deformation occurs in the interface only whereas the matrix undergoes elastic deformation.

(iii) Compute the subincrement of strain;

(iv) Integrate numerically from loop subincrement one to mth subincrement. Use an appropriate constitutive matrix corresponding to a given loading state, as identified in (ii).

(v) Update the stiffness matrix, stresses and hardening parameters for both the matrix and interface. The stress correction procedure is similar to that discussed in Section 3.2.1.

#### 3.4 Comments on sensitivity of the solution to discretization

As discussed before, the conventional strain softening model cannot be employed in strain localization analysis. There are two main reasons for this: first, the rate of strain softening cannot be uniquely defined because it is influenced by the size of the sample; second, the global response depends strongly on the discretization of the system. The latter aspect has been discussed by Pietruszczak and Stolle (1985), Schreyer and Chen(1986), de Borst(1987), Bazant(1988), etc.. In the following, a brief discussion is provided pointing out

the differences between conventional and non-standard formulations within the context of sensitivity of the solution to details of discretization.

#### 3.4.1 Conventional strain-softening formulations

As an illustration, consider a simple one-dimensional problem involving a bar of length  $L$  and unit cross-sectional area, subjected to uniaxial tension. Assume that the stress-strain relation is bilinear (Fig. 3.1a). The slopes of the loading and softening segments are  $E$  and  $\chi_E E$ , respectively, where  $E$  is the unloading modulus and  $\chi_E$  is a parameter relating the softening slope to elastic modulus. Divide the bar into  $m$  elements with equal length  $l$  and suppose that one element has a slight imperfection, i.e. the tensile strength is marginally below that of the other  $(m-1)$  elements. Upon reaching the tensile strength in this element, the failure will occur. However, the tensile strength in other elements will not be exceeded and they will undergo an elastic unloading.

Since the stress is continuous, the displacement increment  $\Delta\delta$  could be expressed as

$$\Delta\delta = \sum \Delta\delta_i = \frac{\Delta\sigma}{E} (L-l) - \frac{\Delta\sigma}{\chi_E E} l \quad (3.30)$$

Inverting the above equation, one obtains

$$\Delta\sigma = \frac{\chi_E E}{(L-l) \chi_E - l} \Delta\delta \quad (3.31)$$

It is apparent that the solution response is a function of the displacement characteristics becomes steeper when the number of elements decreases.

The problem of mesh sensitivity in the context of a two/three dimensional formulation, the displacement is strongly affected by the discretization of the finite element solution. This is a well-known foundation problem incorporated in the finite element method.

#### 3.4.2 Solution based on homogenization

Consider the same one-dimensional problem based on homogenization. When strain localization occurs, the strain is concentrated in a region of thickness  $t$  as

$$\Delta\epsilon = \frac{l-t}{l} \Delta\epsilon^0$$

where  $t$  is the thickness of the region of strain discontinuity along the interface.

The relation between the average strain and the strain in the region of strain discontinuity is

the differences between conventional and non-standard formulations within the context of sensitivity of the solution to details of discretization.

### 3.4.1 Conventional strain-softening formulations

As an illustration, consider a simple one-dimensional problem involving a bar of length  $L$  and unit cross-sectional area, subjected to uniaxial tension. Assume that the stress-strain relation is bilinear (Fig. 3.1a). The slopes of the loading and softening segments are  $E$  and  $\chi_E E$ , respectively, where  $E$  is the unloading modulus and  $\chi_E$  is a parameter relating the softening slope to elastic modulus. Divide the bar into  $m$  elements with equal length  $l$  and suppose that one element has a slight imperfection, i.e. the tensile strength is marginally below that of the other  $(m-1)$  elements. Upon reaching the tensile strength in this element, the failure will occur. However, the tensile strength in other elements will not be exceeded and they will undergo an elastic unloading.

Since the stress is continuous, the displacement increment  $\Delta\delta$  could be expressed as

$$\Delta\delta = \sum \Delta\delta_i = \frac{\Delta\sigma}{E} (L-l) - \frac{\Delta\sigma}{\chi_E E} l \quad (3.30)$$

Inverting the above equation, one obtains

$$\Delta\sigma = \frac{\chi_E E}{(L-l) \chi_E - l} \Delta\delta \quad (3.31)$$

It is apparent that the solution depends on the discretization since the global response is a function of the element size  $l$ . Fig. 3.1c shows the normalized load-displacement characteristics. It is evident that the slope of post-peak response becomes steeper when the number of elements increases or the size of the element decreases.

The problem of mesh sensitivity is even more pronounced within the context of a two/three dimensional analysis. For a standard strain softening formulation, the displacement field as well as the prediction of ultimate load are strongly affected by the discretization. This is illustrated in Fig.3.2 which shows the finite element solution (after Pietruszczak and Stolle, 1985) for a strip foundation problem incorporating a classical approach.

#### 3.4.2 Solution based on the homogenization technique

Consider the same one-dimensional tension tests as before and formulate the problem based on homogenization procedure. For the element in which strain localization occurs, the strain decomposition (refer to section 2.5) can be written as

$$\Delta\epsilon = \frac{l-t}{l} \Delta\epsilon^{(1)} + \frac{t}{l} \Delta\epsilon^{(2)} = \Delta\epsilon^{(1)} + \frac{\Delta g}{l} \quad (3.32)$$

where  $t$  is the thickness of the strain localization zone and  $\Delta g$  is the velocity discontinuity along the interface.

The relation between the stress rate and velocity discontinuity for the

interface is assumed in a bilinear form analogous to that used in section 3.4.1. The slopes of the loading and softening segments are  $K$  and  $\chi_K K$ , respectively, where  $K$  is loading modulus and  $\chi_K$  is a constant. Thus,

$$\Delta\sigma^{(2)} = -\chi_K K \Delta g \quad (3.33)$$

The relation between the stress rate and the strain rate in matrix could be written as

$$\Delta\sigma^{(1)} = E \Delta\epsilon^{(1)} \quad (3.34)$$

Considering the continuity condition for stress, eq.(3.33) and eq.(3.34) can be combined to yield the relation between strain rate in the matrix and the velocity discontinuity in the interface

$$\Delta\epsilon^{(1)} = -\frac{\chi_K K}{E} \Delta g \quad (3.35)$$

Substituting eq.(3.35) into eq.(3.32), one obtains the relation between the average strain rate and the velocity discontinuity

$$\Delta g = \frac{l E}{(E - \chi_K l K)} \Delta\epsilon \quad (3.36)$$

The average strain and stress rates can be defined by substituting eq.(3.36) into eq.(3.33),

$$\Delta\epsilon = -\frac{(E - \chi_K l K)}{\chi_K l E K} \Delta\sigma \quad (3.37)$$

Using eq.(3.37), the increment of displacement can now be expressed as

$$\Delta\delta = \sum \Delta\delta_i = \frac{\Delta\sigma}{E} (L-l) - \frac{(E-\chi_K l K)}{\chi_K E K} \Delta\sigma \quad (3.38)$$

Thus the stress-displacement relation takes the form

$$\Delta\sigma = - \frac{\chi_K L E K}{(E - \chi_K L K)} \Delta\delta \quad (3.39)$$

The above solution is clearly independent of  $l$ , so that the response is not influenced by the discretization.

### 3.5 Finite element analysis of concrete fracture in compression

The complete formulation has been applied to the finite element analysis of a class of boundary-valued problems involving compression-shear as a predominant failure mode. The material parameters adopted for simulations are the same as those used in Chapter 2. The main objective is to investigate the qualitative aspects of the response and to compare them, whenever possible, with experimental trends. In particular, special emphasis is placed on issues related to mesh-sensitivity. The simulations have been carried out by employing the 'tangential stiffness' approach, as discussed in the previous section. All problems have been solved using four-noded rectangular elements with isoparametric formulation and 2x2 Gauss quadrature.

The first problem considered is that of a concrete block (2.5x5.0m) with

initial imperfections (compressive strength reduced by 10%) subjected to uniaxial plane strain compression. The geometry of the problem, together with the location of imperfections, is presented in Fig. 3.3a. The loading process consists of applying uniform vertical displacements along the upper surface under conditions of no-friction at the end platens. Numerical analysis has been carried out using three different meshes, 128, 200 and 325 rectangular elements ( grid I, grid II and grid III, respectively). The results of numerical simulations are presented in Fig. 3.3b-3.3d. Fig. 3.3b provides the mechanical characteristics, load against displacement, obtained for different types of discretization. The characteristics, which exhibit a transition from stable to unstable regime, are only marginally sensitive to the grid type. Fig. 3.3c and 3.3d present the deformed meshes for grids I and III. The fracture mode is non-symmetric and involves formation of a single rupture zone. The thickness of the deformed mesh is virtually invariant with respect to discretization, which ensures mesh objectivity. It should be pointed out that the weak dependence on discretization, which is pertinent to the finite element method itself, is still present within the context of the proposed formulation.

Fig. 3.4 presents the results corresponding to symmetrically distributed imperfections. In this case, a symmetric fracture pattern is formed (Fig.3.4a). The ultimate load is nearly the same as in the previous case, the slope of the softening branch however is significantly lower (Fig.3.4b), which is consistent with Bazant's comments on bifurcation of equilibrium path for symmetrical and non-symmetrical crack band propagation (Bazant, 1989).

Fig.3.5 shows the influence of boundary constraints. The same sample,

with non-symmetric imperfections, is compressed under the condition of perfect bonding at the end platens. The results of numerical simulations are generally consistent with experimental observation. The experimental evidence (Kotsovos, 1983) indicates that as the friction at the interface between the specimen and the loading platen is reduced, the slope of softening branch becomes increasingly more steep and the inclination of the macroscopic fracture plane decreases. It is interesting to note that the fracture mechanism is more diffused now as compared to the case with no boundary constraints.

Fig.3.6 shows the influence of initial confining pressure. The same sample, with non-symmetric imperfections, is compressed under the initial confining pressure of 25MPa. The experimental evidence (Fig2.3 and Fig.2.4) indicates that the initial confining pressure increases the ultimate load significantly. The results of numerical simulations are again consistent with experimental observation.

Fig.3.7 examines the effect of the height of the sample on the deformation characteristics. The experimental results, discussed by Van Mier(1984), indicate that the ascending branch of stress-strain curve as well as the ultimate load are not influenced by the height of specimen whereas the slope of the post-peak branch decreases with the increase in the specimen height. However, the difference in post-peak regime disappears almost completely when the same characteristics are replotted in terms of load-displacement. Numerical analysis has been carried out for specimens of fixed width (2.5m) and different heights of 2.5m (Fig.3.7a), 1.25m (Fig.3.7b) and 5m (Fig.3.3a). The deformed meshes are shown in Fig.3.8a, 3.8b and 3.3b, respectively. In general, the displacement

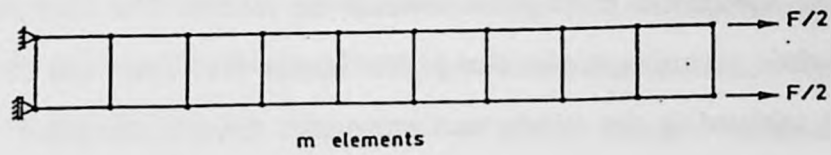
field indicates that the fracture plane takes the form of a zigzag band when specimen height is decreased, which is consistent with the experimental results. Fig.3.7c shows the corresponding load-displacement characteristics. The ultimate load and the slope of the decending branch are almost the same for three different specimens, which again remains consistent with experimental results.

Fig.3.8 shows the results of the analysis of a vertical cut problem, including the study of mesh sensitivity. The geometry and boundary condition are shown in Fig.3.8a. The loading process consisted of applying vertical displacements along the upper boundary. Numerical analysis has been carried out using two different discretization schemes, 280 and 440 rectangular elements. The results are presented in Figs 3.8b-3.8d. Fig. 3.8b shows the load-displacement characteristics for two different discretization schemes, whereas Fig. 3.8c and Fig. 3.8d present the deformed meshes at the end of simulations. The solution, within the context of ultimate load and the fracture mode, is virtually independent of discretization.

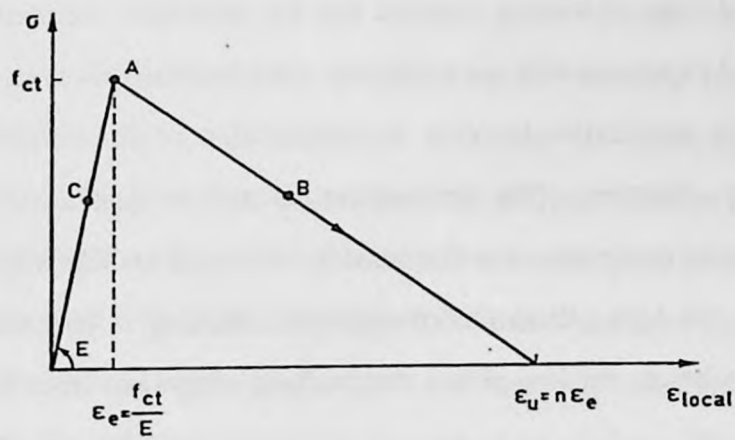
The last problem considered in this section is the analysis of failure mechanism in pillars subjected to compression. The purpose is to study the mode of deformation as a function of the geometry of the pillar. Numerical analysis has been carried out for pillars of fixed width 5.0m and different heights of 5.0m, 7.5m and 10.0m. The loading process consisted of applying uniform vertical displacements along the upper surface under the condition of the perfect bonding at the end platens. The finite element mesh consisted of rectangular elements as shown in Fig. 3.9a. The results of the numerical analysis are shown in Fig. 3.9b and Fig.3.10. Fig.3.9b presents the global load-displacement characteristics.

The response of the shortest (5x5m) block involves the initiation of a crack at the edges and subsequent propagation towards the middle. The load-displacement characteristic remains stable. For higher blocks (5x7.5m) and (5x10m), the crack is initiated in the middle and propagates towards the edges. The load-displacement curve becomes unstable after the formation of a global failure mechanism. Fig. 3.10 shows the deformed meshes for both short and high blocks at the last stage of loading process. For the short one, the predominant mode is the lateral expansion with quite uniform deformation. However, for the high one, the failure mechanism involves the localization of deformation along the two conjugate directions. The present results are in qualitative agreement with experimental observations as discussed in the Jaeger and Cook monograph(1976). Namely, for high pillars the considerable cracking is observed in the central portion, whereas for low pillars the cracking progresses from the exterior.

(a)



(b)



(c)

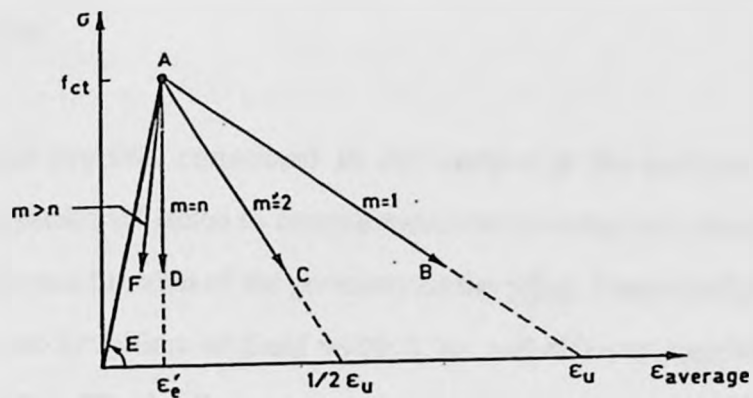
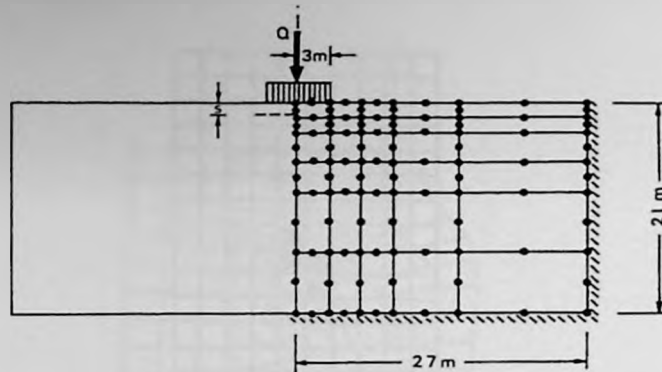


Fig. 3.1 Analysis of in a one-dimensional tension tests (a) discretization; (b) assumed local stress-strain relationship; (c) possible global response with different discretization scheme.

(a)



(b)

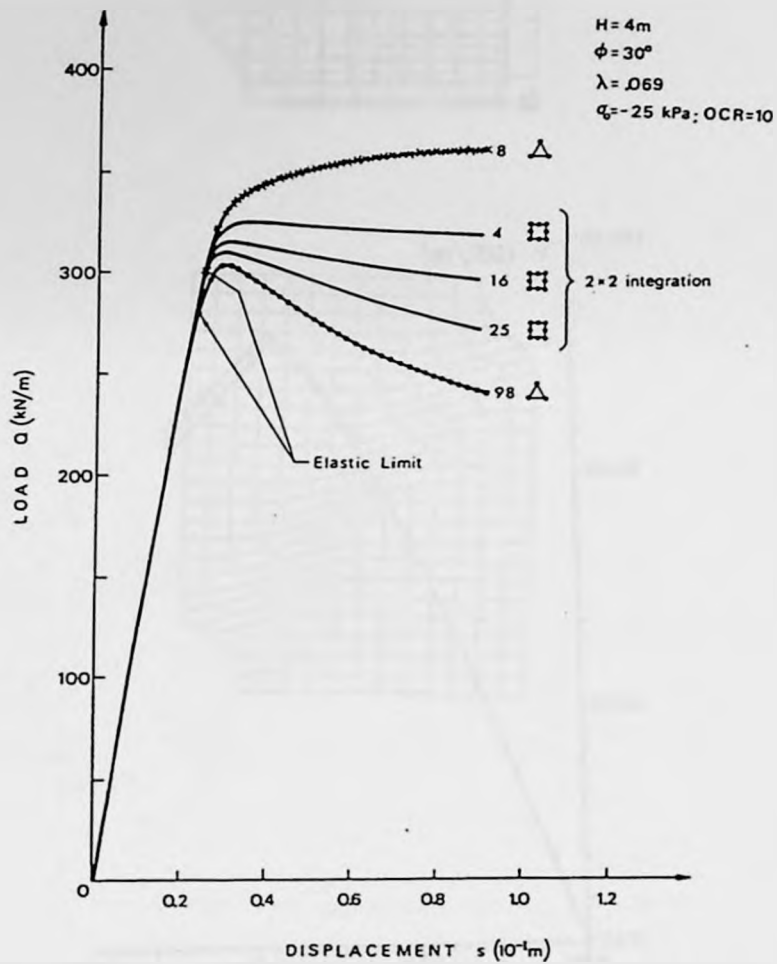
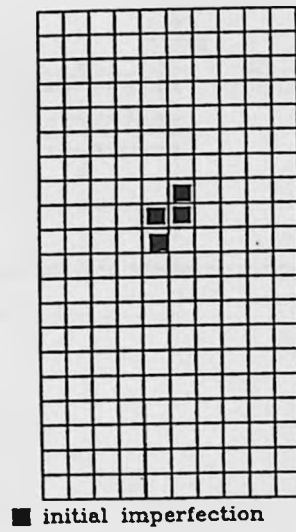
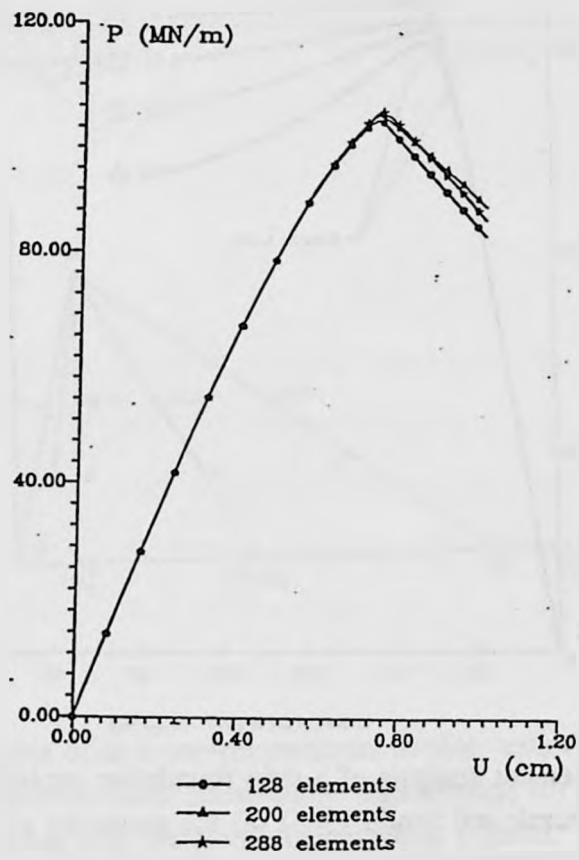


Fig. 3.2 Finite element analysis of a strip foundation problem (after Pietruszczak and Stolle 1985) (a) the geometry of the problem; (b) the influence of discretization on load-displacement characteristics.

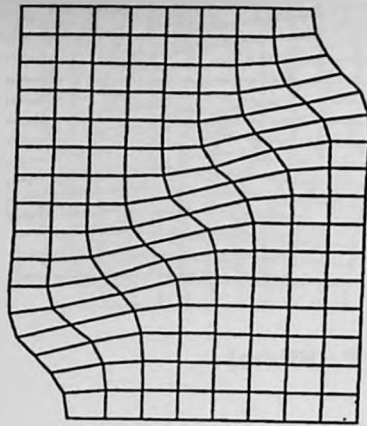
(a)



(b)



(c)



(d)

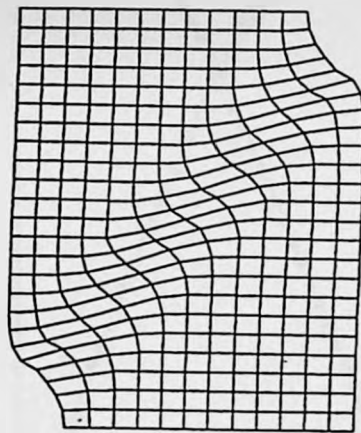
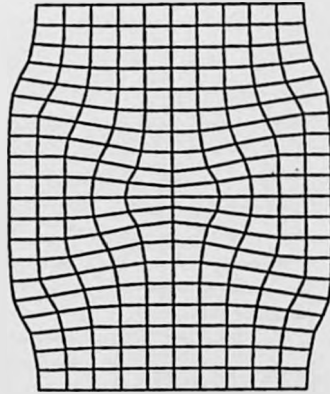


Fig. 3.3 Response of a concrete specimen with initial imperfections, subjected to plane strain uniaxial compression (a) geometry of the problem; (b) load-displacement characteristics; (c) and (d) deformed meshes for grids I and III, respectively.

(a)



(b)

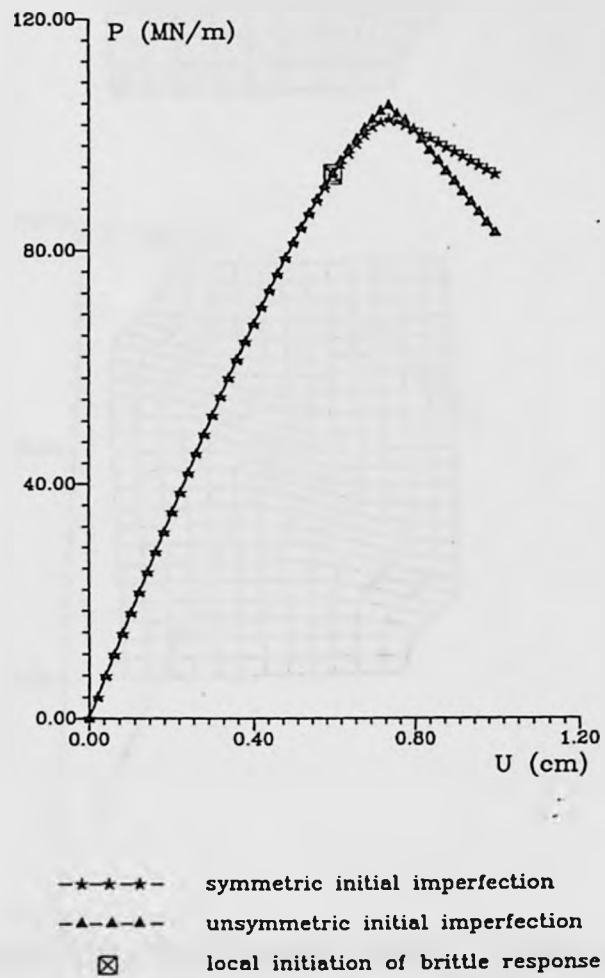
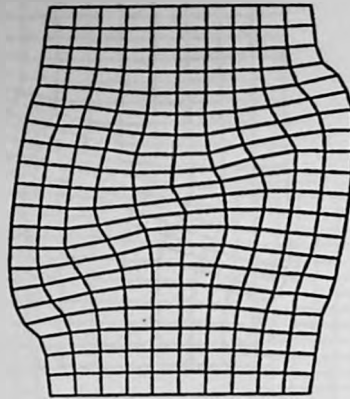


Fig. 3.4 Results for a concrete specimen with symmetrical imperfections (a) deformed mesh; (b) load-displacement characteristics.

(a)



(b)

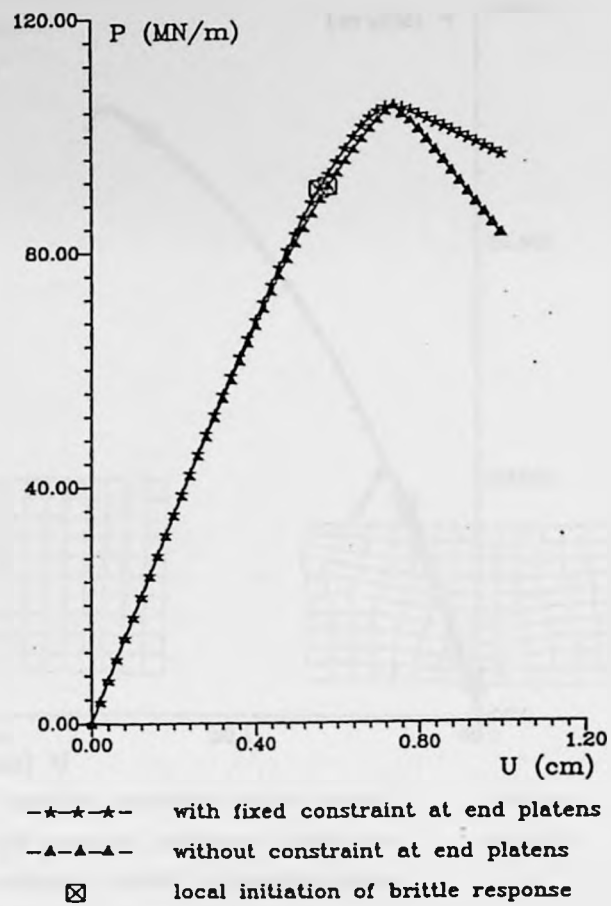
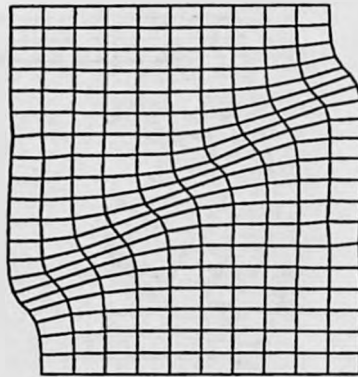


Fig. 3.5 Influence of boundary constraint on deformation characteristics  
 (a) deformed mesh; (b) mechanical characteristics.

(a)



(b)

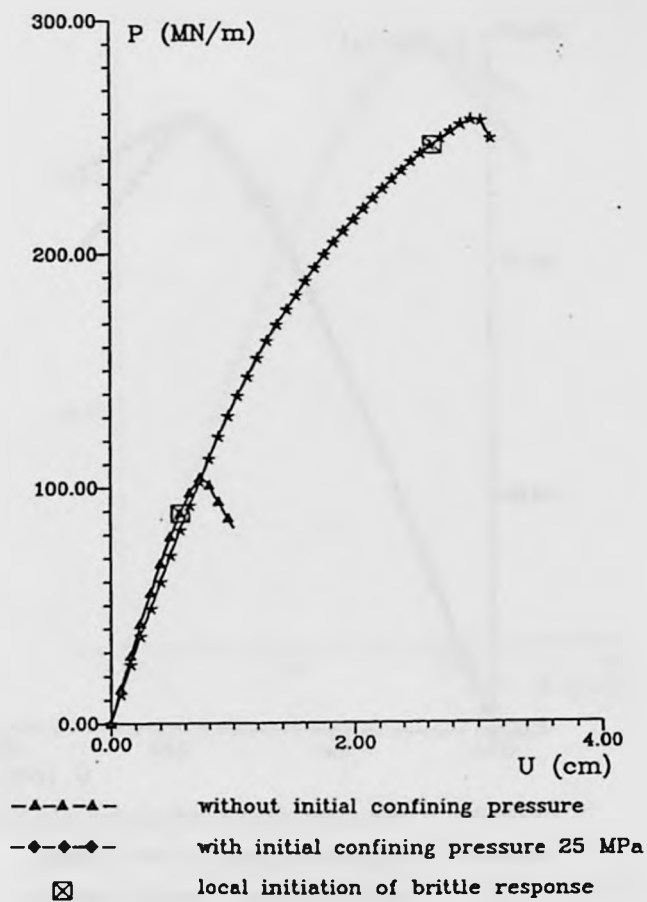
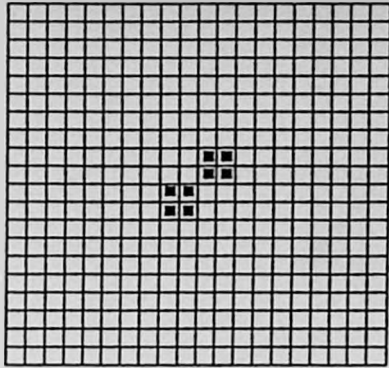
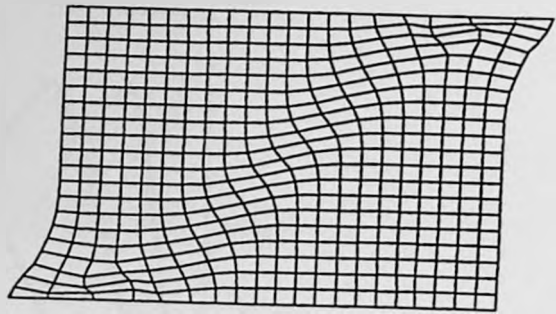


Fig. 3.6 Influence of initial confining pressure on deformation characteristics (a) deformed mesh; (b) load-displacement characteristics.

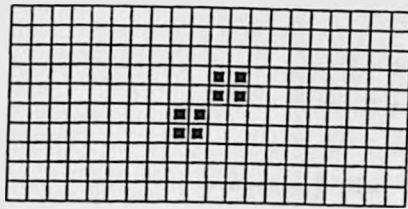
(a)



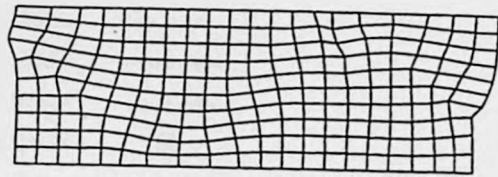
■ initial imperfection



(b)



■ Initial imperfection



(c)

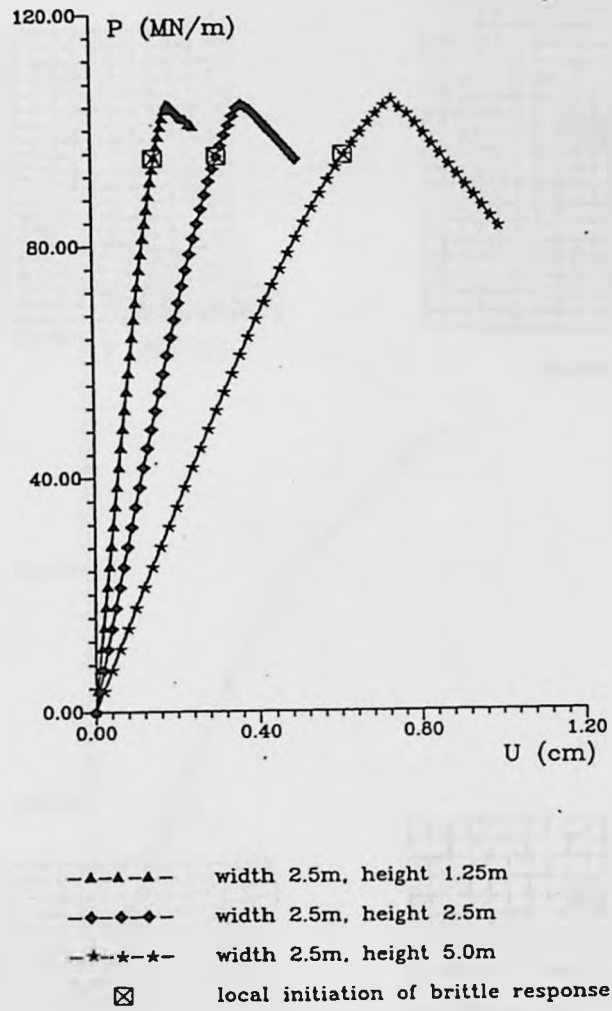
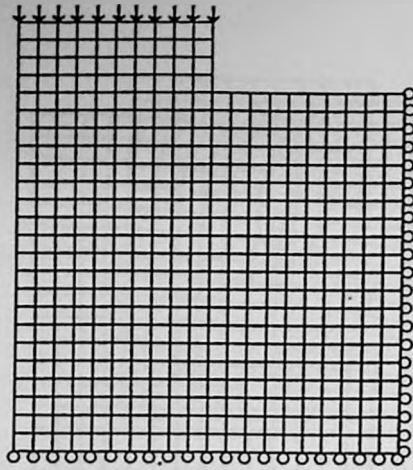
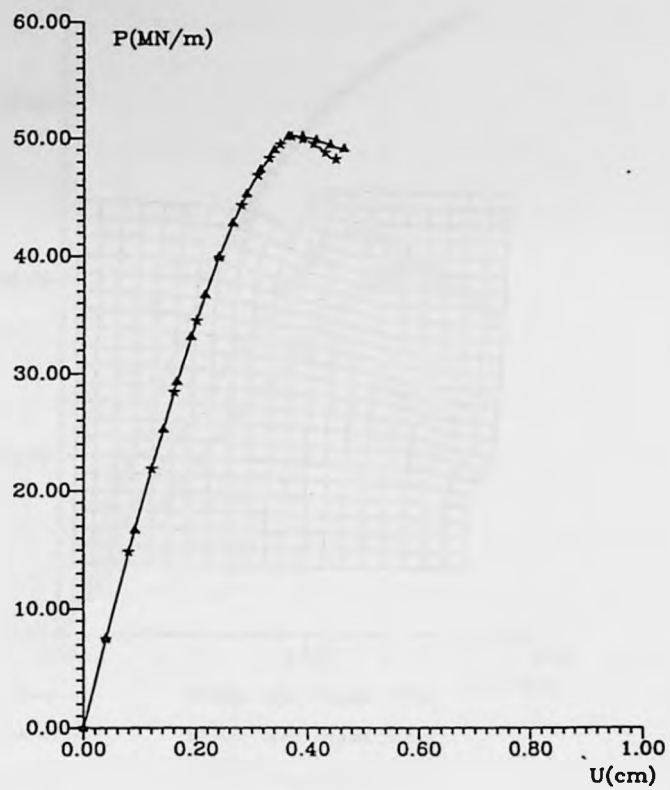


Fig. 3.7 Influence of the height of sample on deformation characteristics  
 (a) geometry and the deformed mesh for sample 2.5x2.5;  
 (b) sample with the height of 1.25m and the width of 2.5m;  
 (c) load-displacement characteristics.

(a)



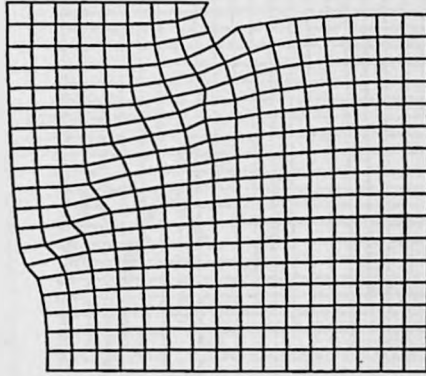
(b)



—▲— 280 elements

—★— 440 elements

(c)



(d)

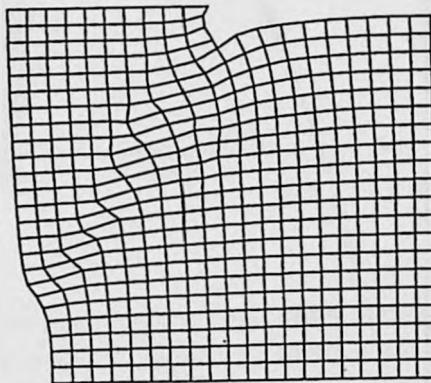


Fig. 3.8 Results of the analysis of a vertical cut problem  
(a) discretization and the boundary conditions;  
(b) load-displacement characteristics; (c) and (d) deformed  
meshes for grid I and grid II, respectively.

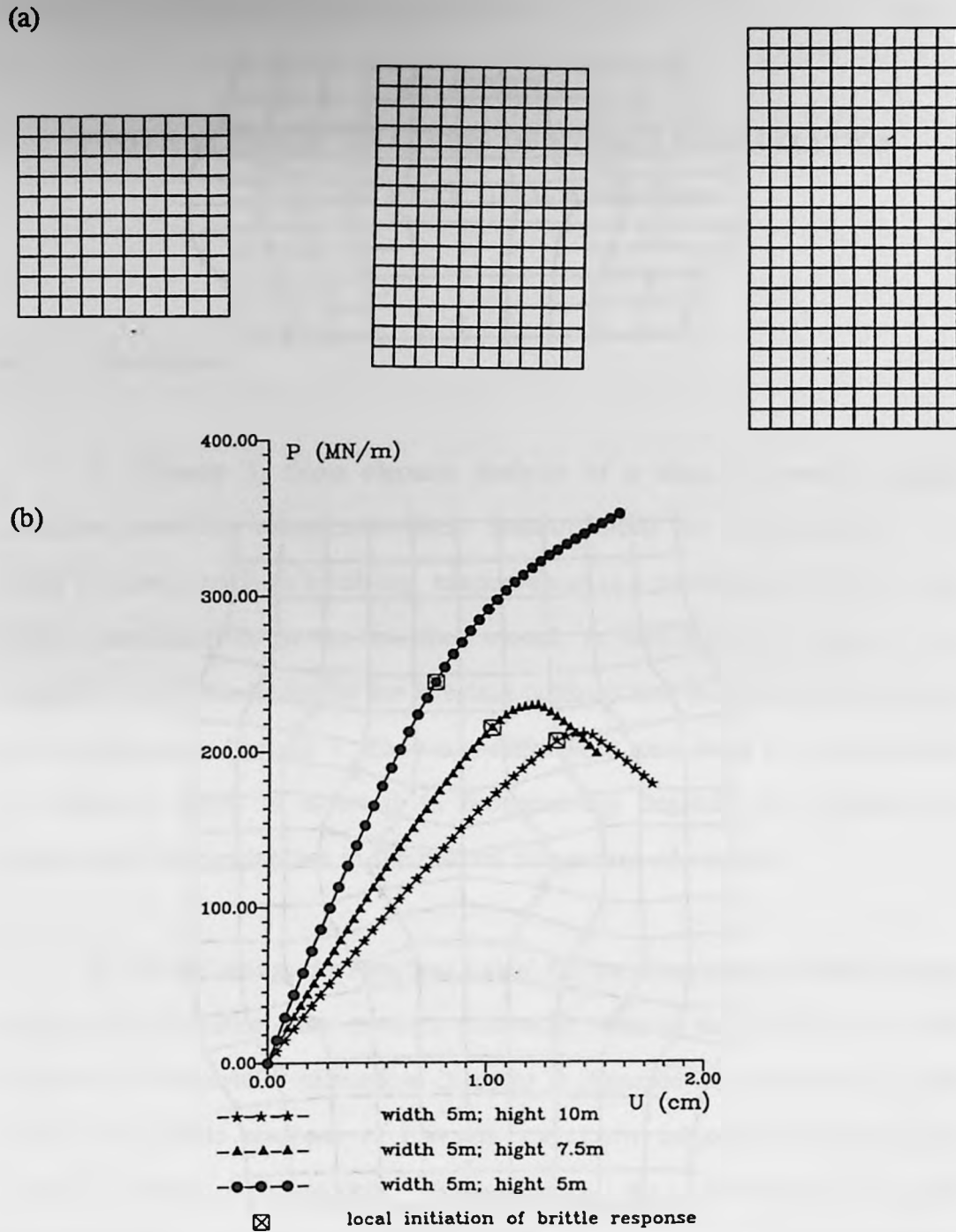
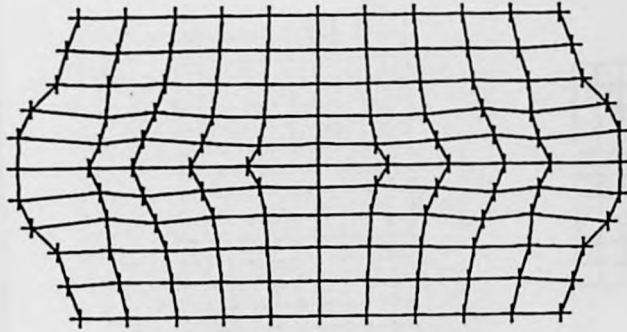


Fig. 3.9 Numerical analysis of failure mechanism of pillars under compression

- (a) geometry, boundary conditions and discretization;  
 (b) load-displacement characteristics.

(a)



(b)

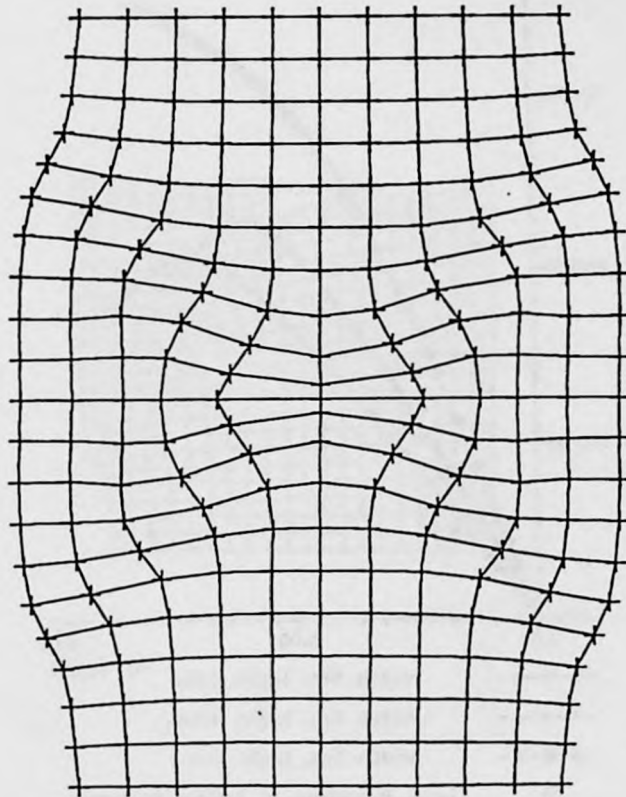


Fig. 3.10 Deformation characteristics of pillars under compression  
(a) Deformed mesh for pillar I at last loading stage;  
(b) Deformed mesh for pillar III at last loading stage.

**CHAPTER 4**  
**FINITE ELEMENT ANALYSIS OF STRAIN LOCALIZATION**  
**IN CONCRETE UNDER TENSION**

4.1 Introduction

In Chapter 3, finite element analysis of a class of boundary-valued problems involving compression-shear fracture mode has been presented. In order to solve problems involving tension-shear as a predominant failure mode, further modifications in the interface model, as discussed in Chapter 2, are required. The formulation for the interface outlined here is a simple extension of that developed in Chapter 2. The main differences stem from the incorporation of cohesion which is assumed to progressively degrade as a function of accumulated discontinuities in the normal component of velocity.

In the following, the interface model for the description of both tension-shear and compression-shear modes is presented, based on the degradation of both cohesion and asperities orientation. In order to illustrate the performance of the model, the brittle response of concrete specimens subjected to plane strain uniaxial tension is simulated. Subsequently, the formulation is again implemented in finite element code to solve some boundary value problems involving tension-shear failure mode. In particular, the finite element analysis of

notched tension and three-point bending specimens is performed. In order to simulate the size effect, geometrically similar specimens with different size are employed in this study.

## 4.2 Constitutive model for the interface

The interface behaviour is, in general, quite different in compression and tension. Under compressive normal stress, the deformation in the neighbourhood of the interface is mainly due to a sliding process, as discussed in Chapter 2. However, under tensile normal stress, the deformation in the interface is the result of a tensile debonding process coupled with sliding along asperities. The constitutive model for the interface presented in Chapter 2 was restricted to compression-shear fracture mode only. The extension to include tension-shear mode is discussed here.

### 4.2.1 Assumptions embedded in the interface model

Assume that the deformation in the neighbourhood of the interface results from both tensile crack opening and sliding along a set of asperities with a predefined orientation. Both opening and sliding processes are coupled by invoking the classical elastic-plastic formulation with the degradation of cohesion (locking of asperities) and asperities orientation (wearing). A non-associated flow rule is employed to account for the dilatancy effects. The degradation of cohesion, attributed to accumulated discontinuities in normal components of velocity, results in an unstable tensile response. The degradation of asperities orientation, attributed to accumulated discontinuities in tangential components of

velocity, results in an unstable shear response.

Similarly, as in Chapter 2, the formulation will be restricted to a two-dimensional case and the interface surface will be idealized as consisting of a set of sawtooth asperities with a uniform inclination  $\alpha$  with respect to the direction of the interface. Thus, only a single representative asperity is considered.

#### 4.2.2 Formulation of the interface model

Given the above assumptions, consider now the deformation process in the neighbourhood of the idealized interface. Introduce again a local frame of reference  $\bar{x}$ , such that  $\bar{x}_2$ -axis is along the normal to the asperity. If  $F = \{F_2, F_1\}^T$  is the resultant force acting at the interface, then

$$F = [T]\bar{F} \quad ; \quad [T] = \begin{bmatrix} \cos\alpha & \sin\alpha \\ -\sin\alpha & \cos\alpha \end{bmatrix} \quad (5.1)$$

where  $\bar{F} = \{\bar{F}_2, \bar{F}_1\}^T$  is the force transmitted through the asperity of orientation  $\alpha$ . A similar transformation rule applies to the displacement discontinuity vector  $g = \{g_2, g_1\}^T$ .

The crack opening and sliding along the asperity are described in terms of an elastic-plastic formulation, in which the yield and plastic potential functions are selected as

$$f(\bar{F}) = |\bar{F}_1| + \eta(\bar{F}_2 - F_1) = 0 \quad ; \quad Q = |\bar{F}_1| + \eta_c \bar{F}_2 = \text{const.} \quad (5.2)$$

with  $\eta = \text{const}$  and  $\eta_c = \text{const}$ . In eq.(5.2),  $F_t$  represents a cohesive force, which undergoes a progressive degradation during the deformation process. The consistency conditions reads

$$\dot{f} = \left(\frac{\partial f}{\partial F}\right)\dot{F} + \left(\frac{\partial f}{\partial F_t}\right)\dot{F}_t \quad ; \quad \dot{F} = [T]^T \dot{F} + \left(\frac{\partial}{\partial \alpha}[T]^T\right)F\dot{\alpha} \quad (5.3)$$

Assume now that the flow rule, the evolution law for the asperities orientation and the degradation law for cohesion take the form

$$\dot{\bar{g}}^p = \lambda \frac{\partial Q}{\partial F} \quad ; \quad \alpha = \alpha(\bar{g}_1^p) \quad ; \quad F_t = F_t(\bar{g}_2^p) \quad (5.4)$$

Since, according to eq. (5.4), the degradation functions are affected only by irreversible deformations, the response in the elastic range can be defined as

$$\dot{F} = [k^e](\dot{g} - \dot{g}^p) \quad ; \quad [k^e] = \begin{bmatrix} k_N & 0 \\ 0 & k_T \end{bmatrix} \quad (5.5)$$

where  $k_N$  and  $k_T$  represent the normal and shear elastic stiffnesses, respectively. Substituting eqs.(5.5) and (5.4) in the consistency condition eq.(5.3) and noting that

$$\dot{\alpha} = \frac{\partial \alpha}{\partial \bar{g}_1^p} \text{sign}(\bar{F}_1)\dot{\lambda}; \quad \dot{\bar{g}}^p = [T]\dot{\bar{g}}_1^p + \left(\frac{\partial}{\partial \alpha}[T]\right)\bar{g}^p\dot{\alpha}; \quad \dot{F}_t = \frac{\partial F_t}{\partial \bar{g}_2^p}\eta_c\dot{\lambda} \quad (5.6)$$

one obtains, after some transformations

$$\dot{\lambda} = \left( \frac{\partial f}{\partial \bar{F}} \right)^T [T]^T [k^e] \dot{g} / H \quad (5.7)$$

where

$$H = H_1 + H_2 + H_3$$

$$H_1 = \left( \frac{\partial f}{\partial \bar{F}} \right)^T [T]^T [k^e] \left[ [T] \frac{\partial Q}{\partial \bar{F}} \right]; \quad H_2 = \eta_c \frac{\partial F_1}{\partial \bar{g}_2^p} \quad (5.8)$$

$$H_3 = \left( \frac{\partial f}{\partial \bar{F}} \right)^T [T]^T [k^e] \left( \frac{\partial}{\partial \alpha} [T] \right) \bar{g}^p \frac{\partial \alpha}{\partial \bar{g}_1^p} \text{sign}(\bar{F}_1) - \left( \frac{\partial f}{\partial \bar{F}} \right)^T \left( \frac{\partial}{\partial \alpha} [T]^T \right) F \frac{\partial \alpha}{\partial \bar{g}_1^p} \text{sign}(\bar{F}_1)$$

It should be noted that since  $\partial F_1 / \partial \bar{g}_2^p < 0 \Rightarrow H_2 < 0$  and  $\partial \alpha / \partial \bar{g}_1^p < 0 \Rightarrow H_3 < 0$  which leads to a locally unstable material response. Following a standard plasticity procedure, i.e. substituting eqs. (5.4), (5.6) and (5.7) into eq. (5.5) and rearranging, one obtains

$$\dot{F} = [K] \dot{g}$$

$$[K] = [K^e] - \frac{[K^e] \left( [T] \frac{\partial Q}{\partial \bar{F}} + \frac{\partial}{\partial \alpha} [T] \bar{g}^p \frac{\partial \alpha}{\partial \bar{g}_1^p} \text{sign}(\bar{F}_1) \right) \left( \frac{\partial f}{\partial \bar{F}} \right)^T [T]^T [K^e]}{H} \quad (5.9)$$

where  $[K]$  is the elastoplastic stiffness ( $\det[K] < 0$ ) whose components are defined, in explicit terms, as

$$k_{11} = k_N - \frac{k_N^2}{H} (\eta \cos \theta \operatorname{sign}(\bar{F}_1) + \sin \alpha) (\sin \alpha + \eta_c \cos \alpha \operatorname{sign}(\bar{F}_1) + g_1^p \frac{\partial \alpha}{\partial \bar{g}_1^p}) \quad (5.10a)$$

$$k_{12} = -\frac{k_N k_T}{H} (-\eta \sin \alpha \operatorname{sign}(\bar{F}_1) + \cos \alpha) (\sin \alpha + \eta_c \cos \alpha \operatorname{sign}(\bar{F}_1) + g_1^p \frac{\partial \alpha}{\partial \bar{g}_1^p}) \quad (5.10b)$$

$$k_{21} = -\frac{k_N k_T}{H} (\eta \cos \alpha \operatorname{sign}(\bar{F}_1) + \sin \alpha) (\cos \alpha - \eta_c \sin \alpha \operatorname{sign}(\bar{F}_1) - g_2^p \frac{\partial \alpha}{\partial \bar{g}_1^p}) \quad (5.10c)$$

$$k_{22} = k_T - \frac{k_T^2}{H} (-\eta \sin \alpha \operatorname{sign}(\bar{F}_1) + \cos \alpha) (\cos \alpha - \eta_c \sin \alpha \operatorname{sign}(\bar{F}_1) - g_2^p \frac{\partial \alpha}{\partial \bar{g}_1^p}) \quad (5.10d)$$

Finally, in order to complete the formulation, the degradation law for cohesion and the orientation of asperities needs to be specified. The degradation law for cohesion is described briefly in the following section. The degradation law for the orientation of asperities may be assumed in the form analogous to that employed in Chapter 2, i.e.

$$\alpha = \alpha_0 \exp(-C \bar{g}_1^p) \quad (5.11)$$

where  $\alpha_0$  is the initial orientation and  $C$  is a material constant.

The constitutive law, presented above, relates the material rates of the resultant force acting at the interface to that of the displacement discontinuity. It should be pointed out here that the material characteristics of the interface are, in general, identifiable from elementary material tests.

#### 4.2.3 Comments on the degradation law for cohesion

The degradation law for cohesion is essentially analogous to the stress-crack opening relation, which is commonly derived from a stress( $\sigma$ )-displacement( $w$ ) characteristics in deformation controlled uniaxial tensile tests. Many forms of such a relationship have been proposed. For example, Cornelissen et. al. (1986) suggested the following expression:

$$\frac{\sigma}{f_t} = [1 + (c_1 \frac{w}{w_o})^3] \exp(-c_2 \frac{w}{w_o}) - \frac{w}{w_o} (1 + c_1^3) \exp(-c_2) \quad (5.12)$$

where  $c_1$ ,  $c_2$  and  $w_o$  are material constants. Gopalaratnam and Shah (1985) proposed the following simple exponential form

$$\frac{\sigma}{f_t} = \exp(-kw^\lambda) \quad (5.13)$$

where  $\lambda$  and  $k$  are material constants.

In general, the stress-crack opening relation is non-linear. In numerical simulations, many simplified expressions, such as linear, bilinear or step-wise

linear, etc., have been widely used. The importance of the shape of the descending branch has been demonstrated by Petersson (1981) and Rots (1986). Here, an exponential relation similar to eq. (5.13) is used for describing the degradation of cohesion

$$F_t = F_0 \exp(-D \bar{g}_2^p) \quad ; \quad F_0 = f_t S \quad (5.14)$$

where  $S$  is the cross-sectional area of the interface and  $D$  is a material constant.

#### 4.3 Modelling of brittle response of concrete specimens subjected to plane strain uniaxial tension

The proceeding formulation has been applied to predict the response of specimens in plane strain uniaxial tension tests. The simulations have been carried out using the following set of interface parameters:

$$k_T = 40,000 \text{ MN/m}^3, \quad k_N = 50,000 \text{ MN/m}^3, \quad \alpha = 10^\circ, \quad \eta_c = 0.5\eta, \\ C = 200 \text{ m}^{-1}, \quad D = 63000 \text{ m}^{-1}.$$

The main objective here was to investigate the influence of the height of the specimen on the post-localized response. It should be noted that the constant  $\eta$  is not explicitly required here since its value is determined from the bifurcation analysis.

The results of numerical analysis are presented in Fig. 4.1. Fig. 4.1a shows the mechanical characteristics for three samples of  $h = 100 \text{ mm}$ ,  $h = 50 \text{ mm}$ , and  $h = 25 \text{ mm}$  subjected to the same loading history. It is evident here that the average rate of strain softening progressively increases with the height of the

specimen, which is consistent with the experimental data (Van Mier, 1986, 1987 and Hordijk et al., 1987). The deformation mode, as observed macroscopically, is strongly anisotropic; i.e. the reduction in the vertical stress is accompanied by significant distortions (Fig.4.1b).

#### 4.4 Finite element analysis of notched specimens

The fracture parameters of cemented brittle materials are commonly determined from tests involving notched specimens. The results of these tests are frequently used to verify the numerical models for concrete fracture analysis. In order to examine the performance of the proposed formulation, the edge-notched tension tests and three-point bending tests have been simulated. The main objective was to investigate the ability of this formulation to model the tension-shear type of fracture mode and the resulting size effect, which has been observed in experimental tests.

The simulations have been carried out by employing the same solution procedure as discussed in Chapter 3. The specimens were discretized using 4-noded elements with isoparametric formulation and 2X2 Gauss quadrature. The material parameters selected for the analysis were identical to those used for numerical simulations discussed in the previous section.

##### 4.4.1 Edge-notched tension tests

Fig. 4.2a gives the specimen geometry and loading conditions typical of edge-notched tension tests. Three specimens, with similar geometry and different

sizes ( $d=38\text{mm}$ ,  $76\text{mm}$  and  $152\text{mm}$ , respectively and the thickness of  $19\text{mm}$ ), subjected to tension under plane stress condition have been analyzed. The loading process consisted of applying uniform vertical displacements along the upper surface.

The results of the numerical simulations are shown in Fig. 4.2b and Fig. 4.3a-4.3c. Fig. 4.2b presents the global load-displacement characteristic obtained for the specimens. For all the cases considered, the initiation of brittle failure takes place at about half the magnitude of the ultimate load and the post-peak response is unstable. The slope of the post-peak response increases with an increase in the size of the specimen. It should be noted that, for the largest specimen the post-peak response cannot be numerically traced. This indicates a likelihood of the snap-back behaviour; i.e. static equilibrium cannot be maintained and a dynamic jump to a new equilibrium position takes place.

The deformed meshes, corresponding to the last loading stage, are given in Fig. 4.3b-4.3c. In general, the brittle failure is initiated around the two notch tips and then propagates towards the middle of the notched section. It is noted that for the smallest specimen, at the ultimate load, the crack propagates through the whole section, whereas for the other two specimens, only a part of this section is damaged.

#### 4.4.2 Three-point bending tests

Fig. 4.4a gives the geometry and loading conditions for three-point bending tests (plane stress). Again, three specimen with similar geometry and

different size ( $d=76\text{mm}$ ,  $152\text{mm}$  and  $304\text{mm}$ , respectively and the thickness of  $38\text{mm}$ ) have been analyzed. The loading process consisted of applying vertical displacements at the upper middle point of the beam.

The results of numerical simulations are shown in Fig.4.4b and Fig.4.5a-4.5c. Fig. 4.4b presents the global load-displacement characteristic obtained for the specimens of different sizes. The main features of these characteristics are similar to those corresponding to tension tests (Fig. 4.2b). The initiation of brittle failure takes place at about half the magnitude of the ultimate load and the slope of the descending branch progressively increases with an increase in the size of the specimen. It should be noted that the snap-back response may take place if the size of the specimen is further increased.

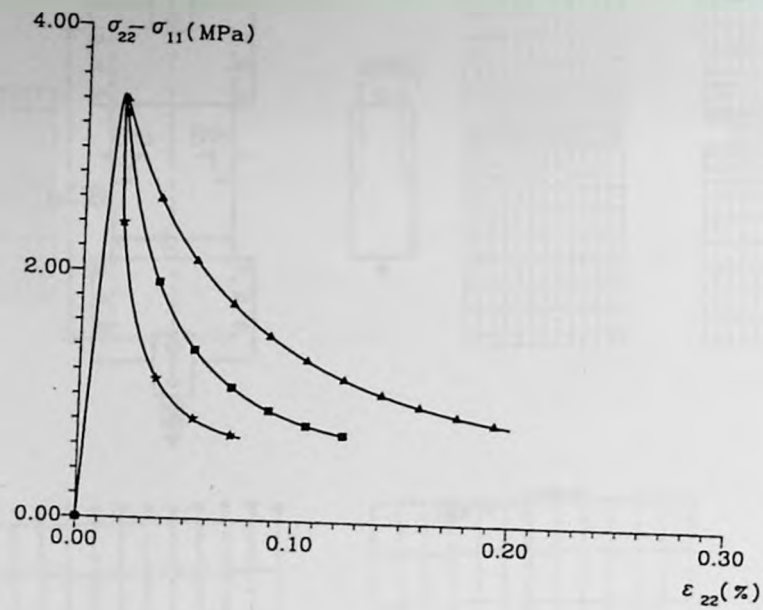
The deformed meshes, corresponding to the last loading stage, are given in Fig. 4.5a-4.5c. For all cases considered, the brittle failure initiates around the notch tip and then propagates upwards along the notched section. For the smallest specimen, at the ultimate load, the crack propagates through a relative large part of section, whereas for the other two specimens, the propagation zone is much smaller.

#### 4.4.3 Simulation of size effect

In order to illustrate the ability of the model to simulate the size effect, the plot of nominal strength at failure ( $\sigma_N = P/bd$ , where  $P$  is the maximum load,  $b$  is the thickness of the specimen) against the characteristic dimension of the specimen is provided in Fig. 4.6. The results are based on numerical results

given in Fig. 4.2b and Fig. 4.4b. The predicted trend, i.e. progressive reduction in nominal strength with increasing size of specimen, is consistent with the experimental evidence (Bazant and Pfeiffer, 1987).

(a)



(b)

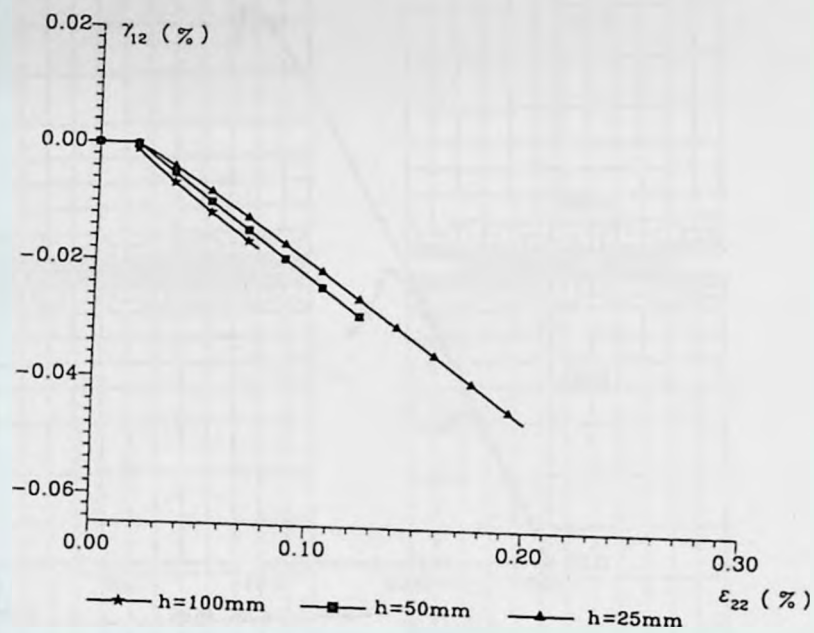
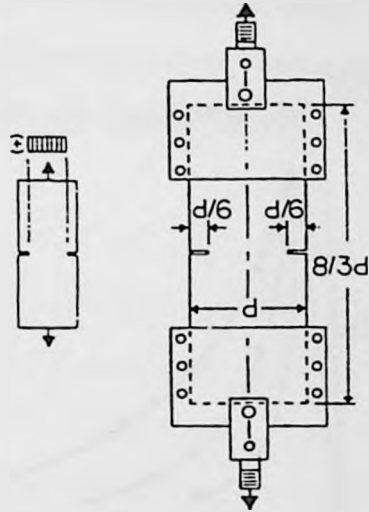


Fig. 4.1 Numerical simulation of height effect in plane strain uniaxial tension  
 (a) stress-strain characteristics; (b) distortion characteristics.

(a)



(b)

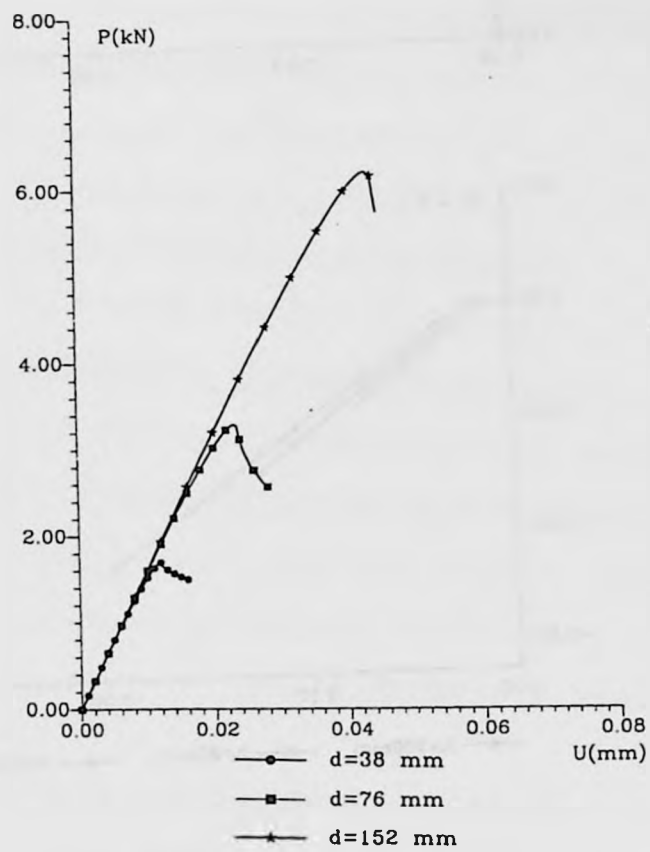


Fig. 4.2 Simulations of edge-notched tension tests  
 (a) geometry and the boundary conditions;  
 (b) load-displacement characteristics.

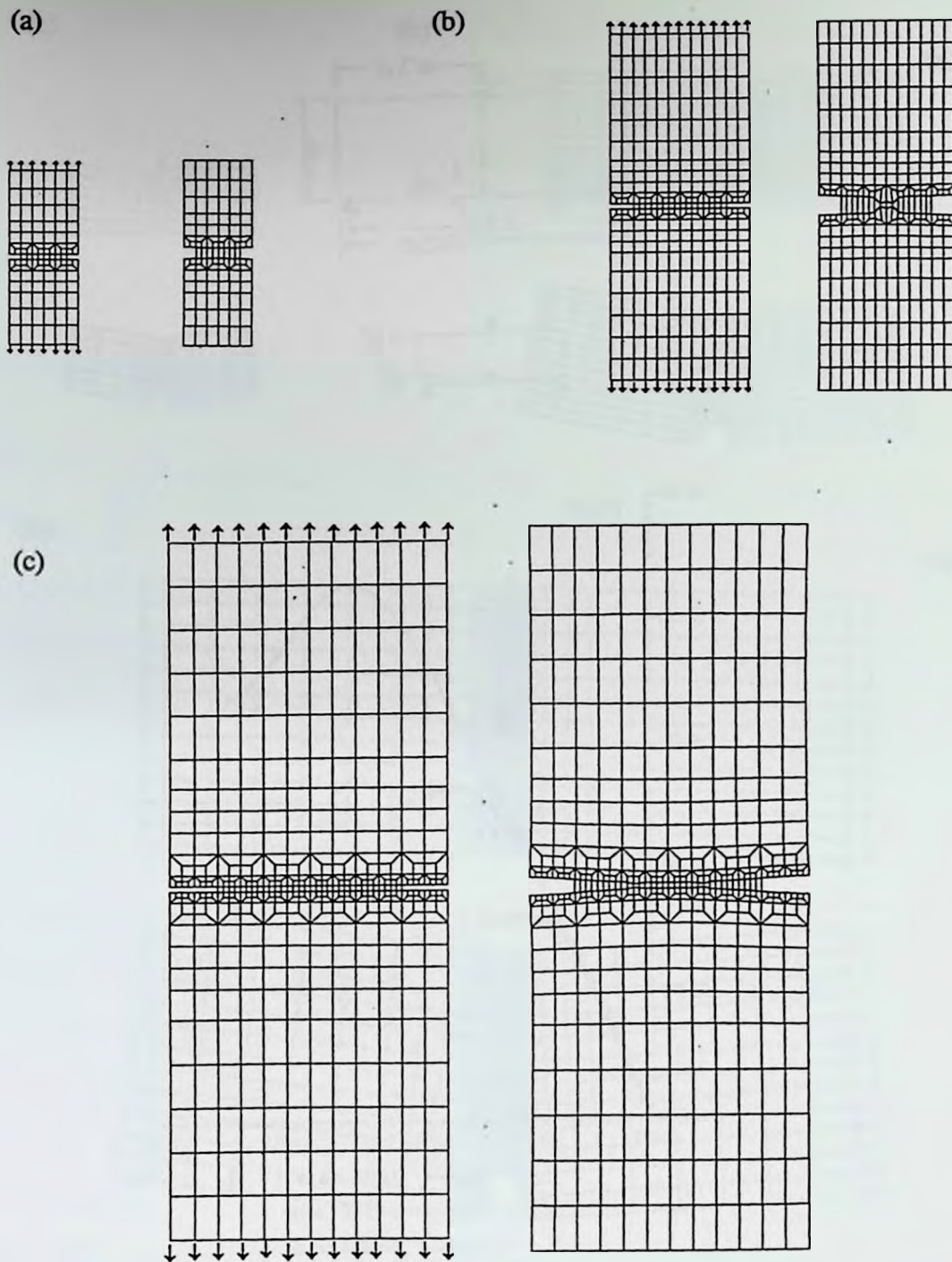
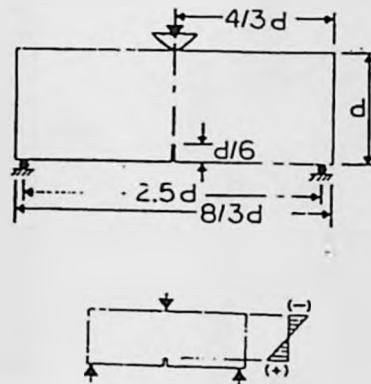


Fig. 4.3 Deformed meshes corresponding to simulations in Fig.4.2  
(a)-(c) samples with  $d=38\text{mm}$ ,  $76\text{mm}$ , and  $152\text{mm}$ , respectively

(a)



(b)

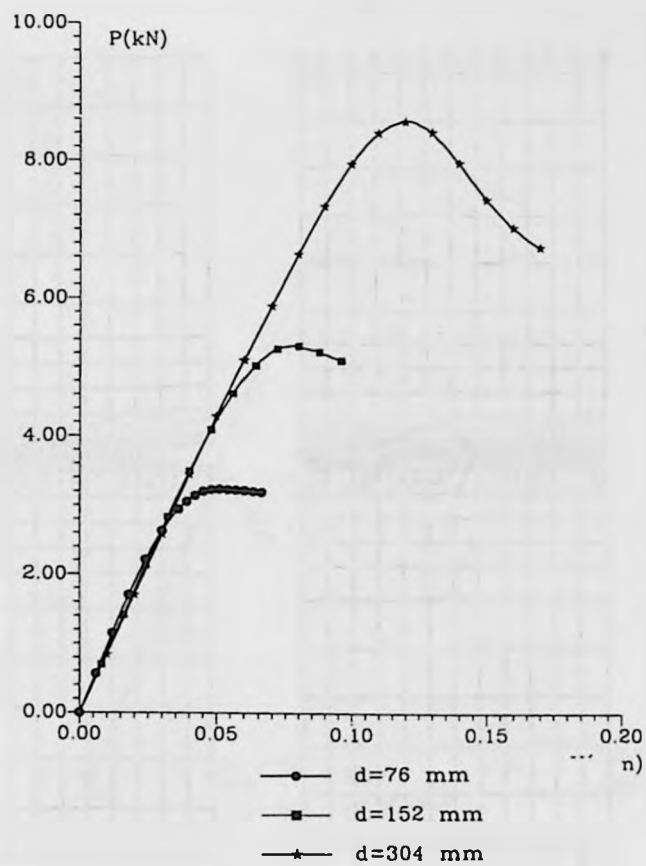


Fig. 4.4 Simulations of three-point bending tests  
 (a) geometry and the boundary conditions;  
 (b) load-displacement characteristics.

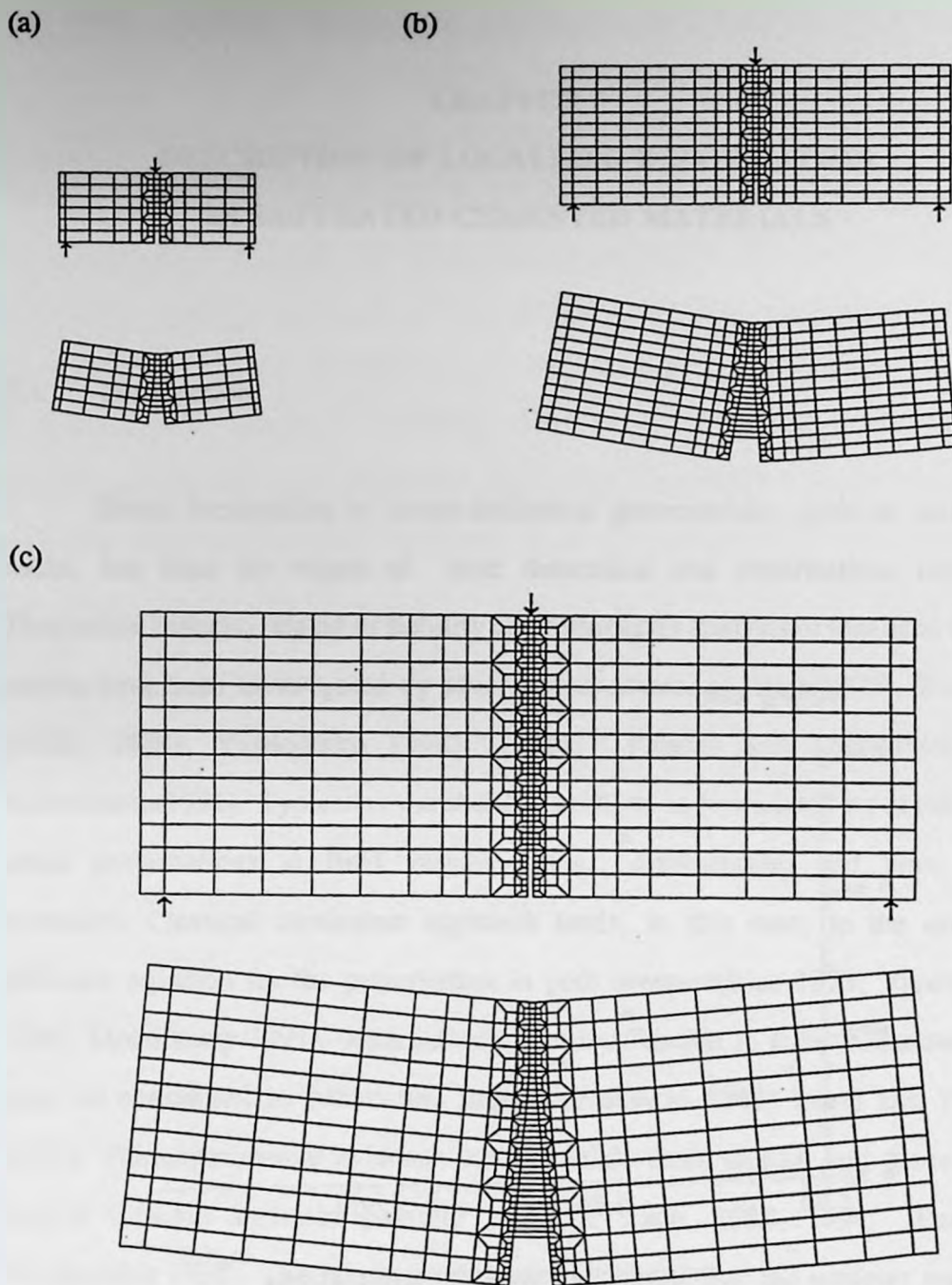


Fig. 4.5 Deformed meshes corresponding to simulations in Fig.4.4  
(a)-(c) samples with  $d=76\text{mm}$ ,  $152\text{mm}$ , and  $308\text{mm}$ , respectively

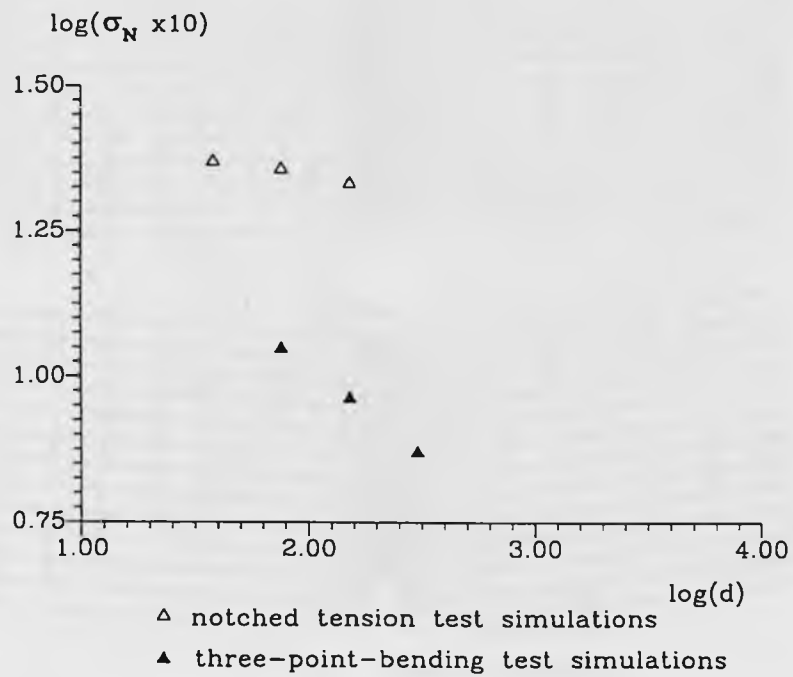


Fig. 4.6 Plots of nominal strength at failure against the dimension  $d$

**CHAPTER 5**  
**DESCRIPTION OF LOCALIZED DEFORMATION**  
**IN SATURATED CEMENTED MATERIALS**

**5.1 Introduction**

Strain localization in water-infiltrated geomaterials, such as soils and rocks, has been the object of both theoretical and experimental research. Theoretical aspects, related to stability and bifurcation analysis of localized failure modes have been investigated by several researchers, cf. Rice(1975), Rudnicki (1982, 1984), Vardoulakis (1985, 1986), Prevost and Loret(1991) and Molenkamp(1991). Typically, the stability problem is formulated by considering small perturbations in field variables (e.g., displacement and pore water pressure). Classical continuum approach leads, in this case, to the ordinary diffusion equation for the perturbation in pore pressure(Rice 1975; Vardoulakis 1985; Molenkamp 1991). Alternatively, the localization in fluid-infiltrated soils may be considered as bifurcation problem(Rudnicki 1982; Loret and Prevost 1991). The experimental evidence comes mainly from triaxial and plane strain biaxial tests on saturated granular soil(e.g., Lade, 1988, 1994; Han and Vardoulakis 1991). The results of those tests indicate that the uniform response is often followed by the formation of distinct shear bands. The latter are typically observed during the stage of progressive decrease in pore pressure, i.e. when the

specimen is dense enough to behave in a dilatant manner. There is no comprehensive experimental study on formation of shear bands (macrocracks) in saturated cemented materials. Moreover, the theoretical considerations are commonly based on Terzaghi's effective stress principle which has its origins in Soil Mechanics. There are serious reservations with regard to applicability of this principle within the context of cemented aggregate mixtures. These arise from the fact that in such materials the skeleton is a continuous body, in contrast to soils which are assemblages of discrete particles. Recently, Pietruszczak and Pande(1995) have employed a new stress decomposition to describe the undrained homogeneous deformation process in saturated cemented materials. It has been shown that the proposed stress decomposition is more appropriate for cemented materials than Terzaghi's effective stress principle.

In this chapter, a mathematical framework for the description of the localized deformation in saturated cemented material is proposed. The onset of localized deformation is considered again as a bifurcation problem. In the localized mode, a finite volume of a saturated cemented material adjacent to localization zone is considered and the macroscopic response is estimated based on the properties of constituents and the kinematic constraints of undrained deformation. In general, pore pressure development is assumed to be affected by the internal transient fluid flow. The proposed approach (Pietruszczak and Xu, 1995a) is, in general sense, similar to that adopted by Pietruszczak (1995) for the description of localized deformation in saturated granular soils.

In the following, the stress decomposition applicable to homogenous deformation of saturated cemented materials is reviewed first. Subsequently, the

criterion for transition to localized deformation is derived, followed by the mathematical description of undrained localized deformation based on a homogenization technique. Finally, the proposed formulation is employed to analyze three limited cases, including (i) undrained response of both constituents, (ii) instantaneous dissipation of pore pressure gradient in both constituents under the global constraint of undrained deformation and (iii) drained response of the interface.

## 5.2 Homogenous deformation of saturated concrete

In cemented materials, the solid skeleton is a continuous, rather than a discrete body. Consequently, Terzaghi's effective stress principle, as commonly adopted in Soil Mechanics, may no longer be applicable. In the following, an alternative formulation, as recently discussed by Pietruszczak and Pande(1995) is briefly reviewed. This will provide the basis for the later studies of both bifurcation criterion and localized deformation.

Consider a sample of saturated cemented material of volume  $V$ . The sample consists of a solid matrix occupying volume  $V_s$  and the voids, of volume  $V_v$ , which are filled with water. It is assumed that all voids are interconnected and open to the atmosphere, i.e. the existence of isolated voids filled with air, which may be present in a typical microstructure, is ignored. Let the sample be under an average homogenous state of stress  $\sigma_{ij}$  defined as

$$\sigma_{ij} = \frac{1}{V} \left( \int_{V_s} \bar{\sigma}_{ij}^s dV_s + \int_{V_v} \bar{p}_w \delta_{ij} dV_v \right) \quad (5.1)$$

where  $\sigma_{ij}^s$  is the stress field in the solids and  $p_w$  is the pore water pressure field referred to a threshold value (atmosphere pressure). The integrals in eq.(5.1) are proportional to the respective averages of both these fields, i.e.

$$\sigma_{ij}^s = \frac{1}{V_s} \int_{V_s} \bar{\sigma}_{ij}^s dV_s \quad ; \quad p_w = \frac{1}{V_v} \int_{V_v} \bar{p}_w \delta_{ij} dV_s \quad (5.2)$$

where  $\sigma_{ij}^s$  represents the average stress in the solid matrix, whereas  $p_w$  is the average excess of pore pressure.

Substitution of eq.(5.2) into eq.(5.1) leads to

$$\sigma_{ij} = \sigma'_{ij} + n p_w \delta_{ij} \quad ; \quad \sigma'_{ij} = (1-n) \sigma_{ij}^s \quad (5.3)$$

where  $\sigma'_{ij}$  represents the average stress in the solid matrix referred to the unit area of the sample. Thus, the total stress  $\sigma_{ij}$  is the weighted average of  $\sigma_{ij}^s$  and  $p_w$ . The weighting factor  $n = V_v/V$  (i.e. the porosity) is, in general, a variable. It should be noted that the matrix is conceptually treated as a continuum and its mechanical properties are described in terms of macroscopic average  $\sigma_{ij}^s$ . The volume averaging adopted here, eq.(5.1), is commonly used in mechanics of composite materials, e.g. Mura(1987).

Given the above definitions, let us examine now the behaviour under undrained conditions. In the absence of pore pressure, the mechanical response is defined by

$$\dot{\sigma}_{ij} = \dot{\sigma}'_{ij} = D_{ijkl} \dot{\epsilon}_{kl} \quad (5.4)$$

where  $D_{ijkl}$  is the constitutive tensor describing the drained properties of the material. In the saturated state a change in pore pressure leads to a corresponding change in  $\sigma'_{ij}$  of the magnitude equal to  $\sigma'_{ij} = \{(1-n)p_w\} \delta_{ij}$ . This is in accordance with eq.(5.3). Apparently, the mechanical response expressed in terms of net stress transmitted by the matrix, must be consistent with that of the dry material. Thus, for a saturated material, eq.(5.4) is revised to

$$[\sigma'_{ij} - (1-n)p_w \delta_{ij}]' = D_{ijkl} \dot{\epsilon}_{kl} \quad (5.5)$$

Eq.(5.5) should be supplemented by the constitutive relation for the pore fluid(water) and kinematic constraint of undrained deformation. Assuming that the water is linearly compressible, the volumetric response is defined as

$$\dot{p}_w = K_w \dot{\epsilon}_{ii}^w \quad ; \quad \dot{\epsilon}^w = \frac{\dot{\epsilon}_{ii}}{n} \quad (5.6)$$

where  $K_w$  is the bulk modulus and the index w refers to the water phase.

### 5.2.1 Application to elastoplastic material

Consider the solid matrix to be an elastoplastic material for which the yield and plastic potential functions are of the form

$$f(\sigma'_{ij}, k) = 0 \quad ; \quad Q(\sigma'_{ij}) = 0 \rightarrow \dot{\epsilon}^p_{ij} = \lambda \frac{\partial Q}{\partial \sigma'_{ij}} \quad (5.7)$$

where  $k = k(\epsilon^p_{ij})$  is a hardening parameter. The consistency condition reads

$$\dot{f} = \frac{\partial f}{\partial \sigma'_{ij}} \dot{\sigma}'_{ij} + H_p \dot{\lambda} = 0 \quad ; \quad H_p = \frac{\partial f}{\partial k} \frac{\partial k}{\partial e^p_{ij}} \frac{\partial Q}{\partial \sigma'_{ij}} \quad (5.8)$$

with  $H_p$  represents the plastic hardening modulus. It is convenient now to express the constitutive relation eq.(5.5) in the form

$$(\sigma'_{ij} - (1-n)p_w \delta_{ij})^* = D_{ijkl}^e (\dot{\epsilon}_{kl} - \dot{\epsilon}_{ij}^p) \quad (5.9)$$

where  $D_{ijkl}^e$  describes the elastic properties under drained conditions.

Differentiating the left-hand side of eq.(5.9) and substituting eq.(5.6) results in

$$\dot{\sigma}'_{ij} - (1-n)C_{ijkl} \dot{\epsilon}_{kl} = D_{ijkl}^e (\dot{\epsilon}_{kl} - \dot{\epsilon}_{ij}^p) \quad ; \quad C_{ijkl} = \frac{K_w}{n} \delta_{ij} \delta_{kl} \quad (5.10)$$

It should be noted that in arriving at eq.(5.10) the term  $\dot{n}p_w$  has been neglected as small compared to  $n\dot{p}_w$ . Substituting now eq.(5.10) in the consistency conditions eq.(5.8) leads to

$$\dot{\lambda} = \frac{[\frac{\partial f}{\partial \sigma'_{ij}}(1-n)C_{ijkl} + \frac{\partial f}{\partial \sigma'_{ij}}D_{ijkl}^e] \dot{\epsilon}_{kl}}{H_e + H_p} \quad ; \quad H_e = \frac{\partial f}{\partial \sigma'_{ij}} D_{ijkl}^e \frac{\partial Q}{\partial \sigma'_{ij}} \quad (5.11)$$

Thus, given eq.(5.10) and the flow rule eq.(5.7), one can write

$$\dot{\sigma}'_{ij} = [D_{ijkl} + (1-n)C_{ijkl}] \dot{\epsilon}_{kl}$$

$$D_{ijkl} = D_{ijkl}^e - \frac{D_{ijpq}^e \frac{\partial Q}{\partial \sigma'_{pq}} \left[ \frac{\partial f}{\partial \sigma'_{rs}} (1-n) C_{rskl} + \frac{\partial f}{\partial \sigma'_{rs}} D_{rskl}^e \right]}{H_e + H_p} \quad (5.12)$$

Finally, differentiating eq.(5.3) and neglecting again the term  $\dot{n}p_w$  gives

$$\dot{\sigma}_{ij} = \bar{D}_{ijkl} \dot{\epsilon}_{kl} = (D_{ijkl} + C_{ijkl}) \dot{\epsilon}_{kl} \quad (5.13)$$

Eq.(5.13) represents the constitutive relation between the total stress and strain rates for a saturated cemented material subjected to an undrained homogeneous deformation process.

### 5.3 Transition to localized deformation as a bifurcation problem

The conditions for the onset of localized deformation in a fluid-infiltrated solid were described by Rice(1982) and Rudnicki(1982, 1984). In their analysis, the deformation of a solid containing an initial imperfection (in the form of a planar band of weakened material) was considered and localization criterion was derived incorporating the effect of coupling between deformation and pore fluid diffusion. In the present study, the above formulation is simplified, since only a homogenous material is considered at the inception of localization. In fact, the formulation is similar to the bifurcation criterion discussed in Section 2.3, it is

expressed however in terms of total stress, which includes the influence of pore fluid pressure.

### 5.3.1 Localization in fluid-infiltrated elastoplastic cemented materials

Based on the stress decomposition described in Section 5.2, the constitutive relation for an elastoplastic fluid-infiltrated cemented material subjected to an undrained deformation process is given by

$$\dot{\sigma}_{ij} = \bar{D}_{ijkl} \dot{\epsilon}_{kl} = (D_{ijkl} + C_{ijkl}) \dot{\epsilon}_{kl} \quad (5.14)$$

where  $\dot{\sigma}_{ij}$  are components of total stress rates,  $\dot{\epsilon}_{ij}$  the components of strain rate,  $D_{ijkl}$  is the tangential stiffness operator.

Now consider the possibility of localization of deformation into a planar band. Denote the band orientation by its unit normal,  $n_j$ . Compatibility requires

$$\epsilon_{ij}^b = \epsilon_{ij}^o + \frac{1}{2}(q_j n_i + q_i n_j) \quad (5.15)$$

for some vector  $q_i$ . In eq.(5.15),  $\epsilon_{ij}^o$  is the strain outside the band,  $\epsilon_{ij}^b$  is the strain within the band. Continuity of traction along the band interface requires

$$n_i (\dot{\sigma}_{ij}^b - \dot{\sigma}_{ij}^o) = 0 \quad (5.16)$$

Combining eqs. (5.14), (5.15) and (5.16) yields

$$(n_i \bar{D}_{ijkl}^b n_j) \dot{q}_k = n_i (\bar{D}_{ijkl}^o - \bar{D}_{ijkl}^b) \dot{\epsilon}_{kl}^o \quad (5.17)$$

Considering that the instantaneous tangent moduli outside and within the band are the same at the initiation of localization, the criterion for strain localization in fluid-infiltrated cemented materials could be defined as

$$\det \bar{B}_{jk} = 0 \quad , \quad \bar{B}_{jk} = n_i \bar{D}_{ijk} n_l \quad (5.18)$$

Thus, the necessary condition for localization is that eq. (5.18) has unique solution for  $n_i$ . In numerical terms, the problem reduces once again to a constrained minimization problem for  $f(n_i) = \det B_{jk}$  under  $n_i n_i = 1$  (Appendix A), where  $n_i$  can be expressed in terms of two spherical angles defining the orientation of the strain discontinuity plane.

### 5.3.2 Bifurcation analysis of localization in saturated concrete

In order to illustrate the above framework consider the response of saturated concrete subjected to some undrained deformation histories. Assume that the drained response can be described by the phenomenological elasto-plasticity framework summarized in Section 2.2. In particular, consider a series of plane strain uniaxial compression tests and assume the following parameters:

$$E = 35,000 \text{ MPa}, \quad \nu = 0.20, \quad f_c = 50 \text{ MPa}, \quad f_t = 5 \text{ MPa}, \quad A = 0.000085, \quad B = 0.95$$

The main objective here is to investigate the sensitivity of the inception of localized damage to the initial confining pressure. The constitutive relation for saturated concrete has been integrated using forward-Euler's explicit algorithm and imposing mixed boundary conditions, i.e.  $\epsilon_{22} < 0$  ( $e_{33} = 0$ ,  $i = 1, 2, 3$ ) under  $\sigma_{11} = 0$ . At each integration step the constitutive matrix  $D_{ijkl}$  was computed and the localization condition eq.(5.18) checked.

The results are presented in Fig.5.1. For comparison, the curves corresponding to different initial confining pressures ranging from 0 to 25 MPa are arranged in the same figure. Fig. 5.1a provides the deviatoric characteristics and Fig. 5.1b presents the history of the evolution of excess pore water pressure. It is clear that the inception of localized mode is delayed by increasing the initial confining pressure. The initial conditions also affect the orientation of the failure plane. In particular, the inclination of the plane with respect to the major principle stress progressively decreases with the increasing initial confining pressure, i.e.  $\beta=56^\circ$ ,  $54^\circ$ , and  $49^\circ$ , respectively. It should be noted that the influence of confining pressure for a saturated sample under undrained conditions is similar to that for a dry sample, c.f. Fig. 2.10.

#### 5.4 Mathematical description of undrained localized deformation in saturated cemented materials

In a localized mode, the deformation in saturated cemented materials is no longer uniform. This results in generation of an excess pore pressure gradient, which prompts a transient fluid flow between the matrix and the interface. In general, this transient fluid flow is affected by many factors, such as the loading rate, permeability of the matrix, the properties of the localized zone, etc.. In the following, a mathematical formulation for the description of localization phenomenon is discussed first. In order to illustrate the proposed formulation, three limited cases are analyzed and the relevant numerical simulations are provided.

##### 5.4.1 Formulation for undrained localized deformation

Consider a volume of saturated material adjacent to a localization zone (interface) which intercepts this region. Let  $\dot{\sigma}^{(i)}$ ,  $\dot{\epsilon}^{(i)}$  ( $i=1,2$ ) denote the average total stress/strain rates in the constituents involved, i.e. the intact material and the medium confined to the localization zone. According to the homogenization technique as discussed in Chapter 2, the volume averages of total stress/strain rates  $\dot{\sigma}$ ,  $\dot{\epsilon}$  in this element could be defined through the averaging procedure

$$\dot{\sigma} = \mu_1 \dot{\sigma}^{(1)} + \mu_2 \dot{\sigma}^{(2)} \quad ; \quad \dot{\epsilon} = \mu_1 \dot{\epsilon}^{(1)} + \mu_2 \dot{\epsilon}^{(2)} \quad (5.19)$$

In eq.(5.19)  $\mu$ 's are the respective volume fractions, which for a two dimensional case can be defined as  $\mu_1 = 1-lt/A$  ;  $\mu_2 = lt/A$ , where  $l$  is the length of the localization zone and  $A$  is the total area of the representative element. Eq.(5.19) can now be supplemented by a set of kinematic and static constraints

$$k_j(\dot{\epsilon}^{(1)}, \dot{\epsilon}^{(2)}) = 0 \quad ; \quad s_j(\dot{\sigma}^{(1)}, \dot{\sigma}^{(2)}) = 0 \quad (5.20)$$

where  $k$ 's and  $s$ 's are scalar-value functions and  $j$  specifies the number of constraints. It should be noted that the static constraints are expressed in terms of total stress components.

The thickness of the localization zone may be considered as negligible when compared to other physical dimensions involved. Thus, it can be formally eliminated from macroscopic considerations by expressing the local deformation field in terms of velocity discontinuities  $\dot{g}$  rather than strain rates  $\dot{\epsilon}^{(2)}$ . Then the strain decomposition in eq.(5.19), combined with the kinematic constraint in eq.(5.20), reduces to

$$[\delta]\dot{\epsilon} = \mu_1[\delta]\dot{\epsilon}^{(1)} + \mu\dot{g} \quad (5.21)$$

where  $\mu = \mu_2/t = 1/A$  defines the ratio of the cross-sectional area of the failure plane to the volume of the representative element. In general,  $\mu$  may be considered as an internal length parameter.

Because of the inhomogeneity of the deformation process, the excess pore pressure in the intact material and interface, denoted as  $p^{(1)}$  and  $p^{(2)}$  respectively, will be different. For the intact material, the constitutive relation, based on stress decomposition eq.(5.4), takes the form

$$\dot{\sigma}^{(1)} = [D]\dot{\epsilon}^{(1)} + \dot{p}^{(1)}\delta \quad ; \quad \dot{p}^{(1)} = \frac{K_f}{n^{(1)}}\delta^T(\dot{\epsilon}^{(1)} - \dot{\epsilon}^{*(1)}) \quad (5.22)$$

where  $\delta^T \dot{\epsilon}^{*(1)}$  is volumetric strain rate in the matrix due to the exchange of fluid between the matrix and the interface. The mass exchange of fluid can be expressed as

$$\dot{m}_f^{(1)} = (\rho^{(1)}V_f^{(1)}) \dot{V}_f^{(1)} = \dot{\rho}^{(1)}V_f^{(1)} + \rho^{(1)}\dot{V}_f^{(1)} \quad (5.23a)$$

where  $V_f^{(1)}$  and  $\rho^{(1)}$  are the fluid volume and density, respectively in the matrix material. The density change in fluid can be expressed as

$$\dot{\rho}^{(1)} = \rho^{(1)} \frac{\dot{p}^{(1)}}{K_f} \quad (5.23b)$$

Substituting eq. (5.23b) into eq.(5.23a) results in

$$\dot{p}^{(1)} = K_f \left( \frac{\dot{m}_f}{\rho^{(1)} V_f^{(1)}} - \frac{\dot{V}_f^{(1)}}{V_f^{(1)}} \right) = \frac{K_f}{n^{(1)}} \left( \frac{\dot{m}_f}{\rho^{(1)} \mu_r A} - \delta^T \dot{\epsilon}^{(1)} \right) \quad (5.24)$$

Comparing eq.(5.22) with eq.(5.24), one obtains the relation between the mass exchange and the volumetric strain rate in the matrix

$$\dot{m}_f^{(1)} = \rho^{(1)} \mu_r A \delta^T \dot{\epsilon} \quad (5.25)$$

For the interface material, the Terzaghi's principle is used because of the nature of the internal structure of the material. Thus the behaviour of the interface material may be defined by

$$\dot{\sigma}^{(2)} = [K] \dot{g} + \dot{p}^{(2)} \delta \quad ; \quad p^{(2)} = \frac{K_f}{n^{(2)} t} (\delta^*)^T (\dot{g} - \dot{\bar{g}}) \quad (5.26)$$

where  $(\delta^*)^T \dot{\bar{g}} / t$  is volumetric strain rate in the interface due to the exchange of fluid between the matrix and the interface. The mass exchange of fluid can be expressed as

$$\dot{m}_f^{(2)} = (\rho^{(2)} \dot{V}_f^{(2)}) = \dot{\rho}^{(2)} V_f^{(2)} + \rho^{(2)} \dot{V}_f^{(2)} \quad (5.27a)$$

where  $V_f^{(2)}$  and  $\rho^{(2)}$  are the fluid volume and density, respectively, in the intact material. The density change can be expressed as

$$\dot{\rho}^{(2)} = \rho^{(2)} \frac{\dot{p}^{(2)}}{K_f} \quad (5.27b)$$

Substituting eq. (5.27b) into eq.(5.27a) results in

$$\dot{p}^{(2)} = K_f \left( \frac{\dot{m}_f}{\rho^{(2)} V_f^{(2)}} - \frac{V_f^{(2)}}{V_f^{(2)}} \right) = \frac{K_f}{n^{(2)} t} \left( \frac{\dot{m}_f}{\rho^{(2)} \mu A} - \delta^* T \dot{g} \right) \quad (5.28)$$

Comparing eq.(5.28) and eq.(5.26), one obtains the relation between the mass exchange of fluid and the volumetric strain rate in the interface

$$\dot{m}_f^{(2)} = \rho^{(2)} \mu A \delta^* T \dot{g} \quad (5.29)$$

Since globally the conditions remain undrained, the mass conservation requires  $\dot{m}_f^{(1)} + \dot{m}_f^{(2)} = 0$ , thus,

$$\mu_1 \rho^{(1)} \delta T \dot{\epsilon}^{(1)} + \mu \rho^{(2)} (\delta^*) T \dot{g} = 0 \quad (5.30a)$$

It is noted that, if the compressibility of fluid is neglected, we have  $\delta \dot{\epsilon} \rightarrow 0$ , which in view of the decomposition eq.(5.21) becomes

$$\mu_1 \delta T \dot{\epsilon}^{(1)} + \mu (\delta^*) T \dot{g} = 0 \quad (5.30b)$$

The above equation is a special case of eq. (5.30a), which corresponds to  $\dot{\rho}^{(1)} = \dot{\rho}^{(2)}$ .

In order to complete the formulation, the relation defining the rate of fluid transfer between the intact material and the interface, has to be specified. Following Rudnicki(1982), assume that the fluid flux between the intact material and the interface is proportional to the difference in pore fluid pressure. This

assumption, together with the assumption of homogeneous deformation in the interface, requires that the rate of exchange of fluid has the following form

$$C_d(p_f^{(1)} - p_f^{(2)}) = \dot{m}_f \quad (5.31)$$

where  $C_d$  is an empirical constant, which can be interpreted as the reciprocal of the time scale for fluid mass exchange between the interface and the matrix. In the following, two limited cases, which correspond to (i) undrained response of both constituents and (ii) instantaneous dissipation of excess pore pressure gradient are studied.

#### 5.4.2 Limited case I ( $C_d = 0$ )

In this case, no exchange of fluid between the interface and the matrix is considered. Therefore, both constituents involved respond in an undrained manner. The change in excess pore pressure in both constituents could be derived directly from eqs. (5.22) and (5.26)

$$\dot{p}^{(1)} = \frac{K_f}{n^{(1)}} \delta^T \dot{\epsilon}^{(1)} \quad ; \quad \dot{p}^{(2)} = \frac{K_f}{n^{(2)t}} (\delta^*)^T \dot{g} \quad (5.33)$$

The behaviour of the intact material can be defined based on stress decomposition eq.(5.4),

$$\dot{\sigma}^{(1)} = [\bar{D}] \dot{\epsilon}^{(1)} \quad ; \quad [\bar{D}] = [D] + [C] \quad (5.34)$$

Given the fact that the microstructure of the interface is discrete in nature, its

undrained response can be described by invoking Terzaghi's decomposition, i.e.

$$\dot{\sigma}^{(2)} = [\bar{K}] \dot{g} \quad ; \quad [\bar{K}] = [K] + \delta \frac{K_f}{n^{(2)} t} (\delta^*)^T \quad (5.35)$$

It is apparent that the problem is similar to the formulation discussed in section 2.3. Combining the above equations results, after some algebraic manipulations, in relation between the overall strain rate and the strain rate in the matrix as well as the velocity discontinuity (see Appendix D for details)

$$\dot{\epsilon}^{(1)} = [\bar{S}_1] \dot{\epsilon} \quad ; \quad \dot{g} = [\bar{S}_2] \dot{\epsilon} \quad (5.36)$$

Considering that the components of the stress rates in both constituents are comparable, the following approximation may be employed

$$\dot{\sigma} \approx \dot{\sigma}^{(1)} = [\bar{D}] [\bar{S}_1] \dot{\epsilon} \quad (5.37)$$

Eq. (5.37), supplemented by relations (5.36), provide a complete mathematical solution, i.e. define the overall response as well as the stress/strain rates in both constituents under undrained condition.

#### 5.4.3 Limited case II ( $C_d \rightarrow \infty$ )

In this case, an instantaneous dissipation of the excess pore pressure gradient between the interface and the matrix takes place. Thus, the global undrained response is constrained by  $p^{(1)} = p^{(2)}$ , which results in

$$\delta^T(\dot{\epsilon}^{(1)} - \dot{\bar{\epsilon}}^{(1)}) = \frac{1}{t}(\delta^*)^T(\dot{g} - \dot{\bar{g}}) \quad (5.38)$$

Since the pore pressures in both constituents remain the same,  $\rho^{(1)} = \rho^{(2)} = \rho$ , so that the mass balance equation becomes

$$\rho \{ \mu_1 \delta^T \dot{\bar{\epsilon}}^{(1)} + \mu (\delta^*)^T \dot{\bar{g}} \} = 0 \quad (5.39)$$

Combining both eqs. (5.38) and (5.39), and noting that  $(\mu_1 + \mu_2 = 1)$  and  $\mu = \mu_2/t$ , one obtains

$$\delta^T \dot{\bar{\epsilon}}^{(1)} = \mu_2 \delta^T \dot{\epsilon}^{(1)} - \mu (\delta^*)^T \dot{g} \quad (5.40)$$

Now substituting eq.(5.40) in eq.(5.22), results in

$$\dot{p}^{(1)} = \frac{K_f}{n} [\mu_1 \delta^T \dot{\epsilon}^{(1)} + \mu (\delta^*)^T \dot{g}] \quad (5.41)$$

which in view of eq.(5.21)

$$\delta^T \dot{\bar{\epsilon}} = \mu_1 \delta^T \dot{\bar{\epsilon}}^{(1)} + \mu (\delta^*)^T \dot{g} \quad (5.42)$$

becomes

$$\dot{p}^{(1)} = \frac{K_f}{n} \delta^T \dot{\bar{\epsilon}} = \dot{p}^{(2)} \quad (5.43)$$

The constitutive relation for the intact material can be derived (see Appendix E for details) using stress decomposition eq.(5.4)

$$\dot{\sigma}^{(1)} = [\bar{D}] \dot{\epsilon}^{(1)} + [G] \dot{g} \quad ; \quad [\bar{D}] = [D] + [C] \quad (5.44)$$

On the other hand, the constitutive relations for the interface material can be established based on Terzaghi's decomposition

$$\dot{\sigma}^{(2)} = [\bar{K}] \dot{g} + \frac{K_f}{n} \delta^T \dot{\epsilon}^{(1)} \quad ; \quad [\bar{K}] = [K] + \mu \delta \frac{K_f}{n} (\delta^*)^T \quad (5.45)$$

The global constitutive relation can now be derived following the homogenization procedure adopted before. The relation between the overall strain rates and the strain rates in the constituents can be written as

$$\dot{\epsilon}^{(1)} = [\tilde{S}_1] \dot{\epsilon} \quad ; \quad \dot{g} = [\tilde{S}_2] \dot{\epsilon} \quad (5.46)$$

where  $[\tilde{S}_1]$  and  $[\tilde{S}_2]$  are defined in Appendix F. Considering that the components of the stress rates in both constituents are comparable,

$$\dot{\sigma} \approx \dot{\sigma}^{(1)} = ([\bar{D}][\tilde{S}_1] + [G][\tilde{S}_2]) \dot{\epsilon} \quad (5.47)$$

Eqs. (5.46) and (5.47) represent the constitutive relations governing the undrained deformation coupled with the instantaneous dissipation of the excess pore pressure gradient.

#### 5.4.4 Numerical simulations and discussions

The preceding formulation has been applied to extend the predictions of plane strain compression tests under undrained condition (Fig. 5.1) to the post-localized regime. Here, only the results corresponding to the confining pressure

of 5MPa are provided. The simulations have been carried out assuming the following set of parameters:

$$K_T = 15000 \text{ MN/m}^3; K_N = 15000 \text{ MN/m}^3; \alpha = 10^\circ; C = 200 \text{ m}^{-1}$$

The above choice is rather arbitrary as no adequate experimental data is available. The objective here is to investigate the qualitative trends and to compare the response as predicted by the formulations corresponding to  $C_d = 0$  and  $C_d \rightarrow \infty$ .

The numerical results, Fig. 5.2, indicate that the onset of localized deformation affects both the deformation characteristics and the evolution of the excess pore pressure. The deviatoric stress strain curve, Fig 5.2a, remains stable, in spite of the strain softening characteristics of the interface materials. The formation of a macrocrack results in an abrupt reduction in the stiffness of the material, which has been observed experimentally (Han and Vardoulakis, 1990). The deviatoric stress-strain characteristics, corresponding to  $C_d = 0$  and  $C_d \rightarrow \infty$  are very similar. However, it should be noted that the deformation modes corresponding to fully undrained and coupled formulation are different. In the former case, both constituents undergo an active loading process, whereas in the coupled formulation the intact material unloads at the inception of localization and remains elastic throughout. The formation of a macrocrack also affects the evolution of the excess pore water pressure. It is evident from Fig. 5.2b that the rate of pore pressure generation abruptly decreases at the onset of localization. Fully undrained formulation predicts generation of an excess pore pressure gradient, which prompts the internal flow of water towards the interface ( $p^{(1)} > p^{(2)}$ ). The prediction for the coupled formulation ( $p^{(1)} = p^{(2)}$ ) falls slightly below that corresponding to eq.(5.40), which is largely due to instantaneous unloading of the intact material.

In many practical situations, the interface may come into a direct contact with the atmosphere, resulting in an instantaneous dissipation of the excess pore pressure. This can be mathematically expressed by imposing the following constraint

$$\dot{p}^{(1)} = \frac{K_f}{n} \delta T \dot{\epsilon}^{(1)} \quad ; \quad \dot{p}^{(2)} = 0 \quad , \quad p^{(2)} = 0 \quad (5.48)$$

The formulation for this case may be derived directly from the formulation corresponding to  $C_d = 0$  by changing the interface properties from undrained to drained. The results of numerical simulations are provided in Fig. 5.3. The deviatoric stress strain characteristics, Fig. 5.3a, become unstable, which is consistent with the experimental results (Pietruszczak et al., 1995). In this case, the intact material undergoes an unloading process, which results in a progressive decrease in the excess pore pressure. For comparison, the deviatoric characteristics for both saturated and dry samples are presented in Fig. 5.4. As shown in this figure, the strength of a dry material is higher than that of saturated one, which is consistent with the experimental evidence (Pietruszczak et al., 1995).

Finally, Fig. 5.5, 5.6 and 5.7 illustrate the influence of the height of the sample on the mechanical response for the three cases. The numerical simulations were carried out for two samples of  $h=0.1\text{m}$  and  $h=0.2\text{m}$ . For both cases of  $C_d = 0$  and  $C_d \rightarrow \infty$ , the deviatoric stress strain characteristics and the evolution of the excess pore pressure are affected by the height of the specimen (Fig. 5.5, 5.6); however, the influence is only marginal. This is in contrast to the case corresponding to drained conditions in the interface (Fig. 5.7). For the latter case,

the characteristics show the same trends as those for dry samples (Fig.2.13).

#### 5.4.5 Comparison with the response of granular soil involving localized deformation

In the above section, the main characteristics of localized deformation in saturated cemented materials under different drainage constraints have been simulated. It may be of interest to compare the basic trends with those corresponding to granular soil (Pietruszczak, 1995). It should be noted that the formulation for cohesionless soil can be derived directly from the above formulation by employing Terzaghi's effective principle instead of stress decomposition eq.(5.3) (Pietruszczak and Xu, 1995a).

Figs. 5.8a and 5.8b (after Pietruszczak 1995) show the undrained characteristics of a cohesionless granular soil in the presence of shear band. The specimen (dense sand) was tested in plane strain uniaxial compression under the initial confining pressure of 200kPa. The numerical analysis was based on a deviatoric hardening model and all relevant details are provided in the original reference. The predictions regarding the onset of localization, based on classical bifurcation analysis as used in this study, were inadequate in this case. Thus, the numerical simulations, corresponding to inhomogeneous deformation mode, have been completed based on the initial conditions consistent with the experimental data (Han and Vardoulakis 1991). It is interesting to note, that the deviatoric characteristics past the onset of localization, Fig. 5.8a, are qualitatively similar to those obtained for concrete (Fig.5.2a). The predictions based on fully drained response and the formulation coupled with dissipation of excess pore

pressure gradient are again fairly close, inspite of invoking different deformation mechanism(viz. active loading and unloading of the intact material). The formation of shear band also affects the evolution of excess pore pressure. It is evident from Fig.5.8b, that the rate of pore pressure generation abruptly decreases at the onset of localization. Again, the qualitative trends are similar to those obtained for concrete, Fig.5.2b and are consistent with experimental observation (Han and Vardoulakis, 1991).

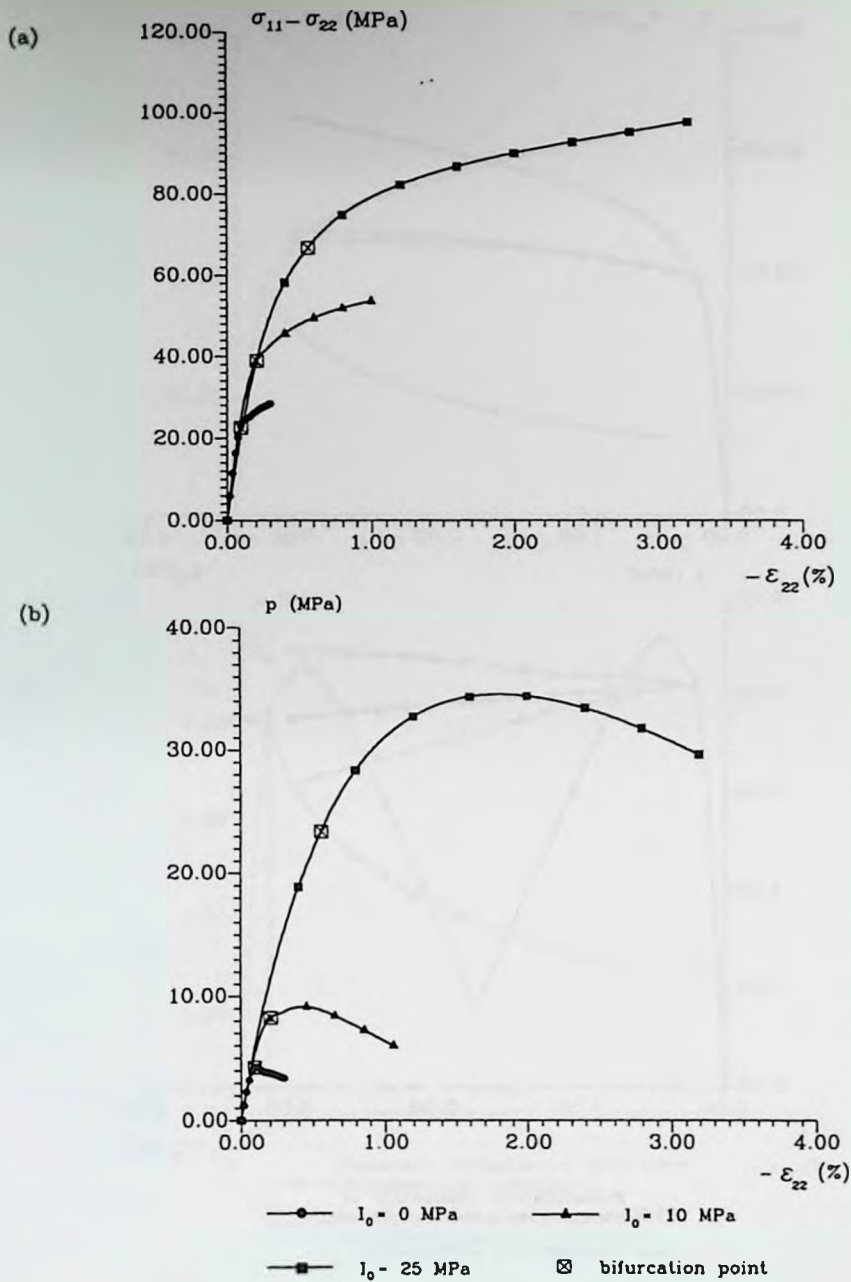


Fig. 5.1 Numerical simulations of a transition to localized deformation in saturated cemented material (a) deviatoric characteristics; (b) evolution of the excess pore pressure.

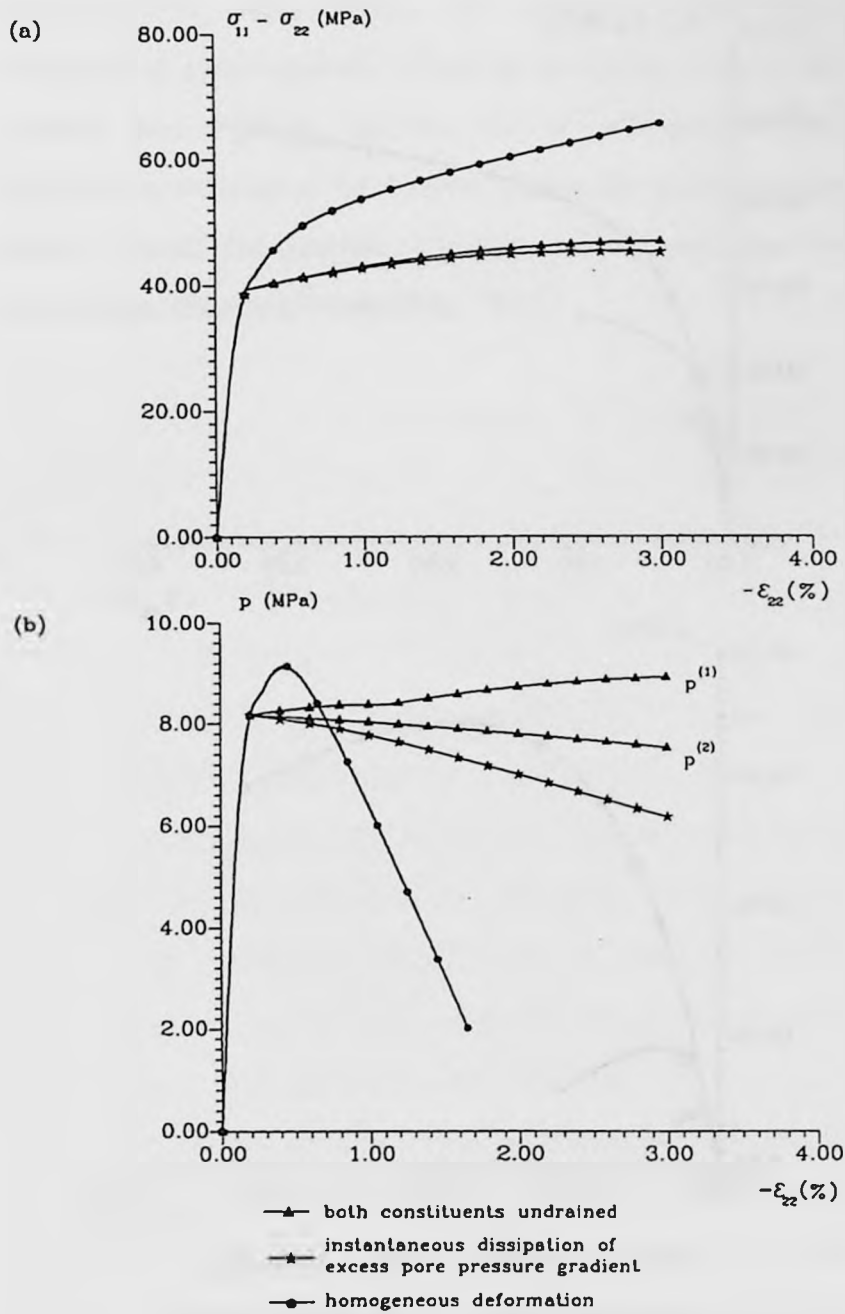


Fig. 5.2 Comparison of localized response corresponding to  $C_d=0$  and  $C_d \rightarrow \infty$  (a) deviatoric characteristics; (b) evolution of excess pore pressure.

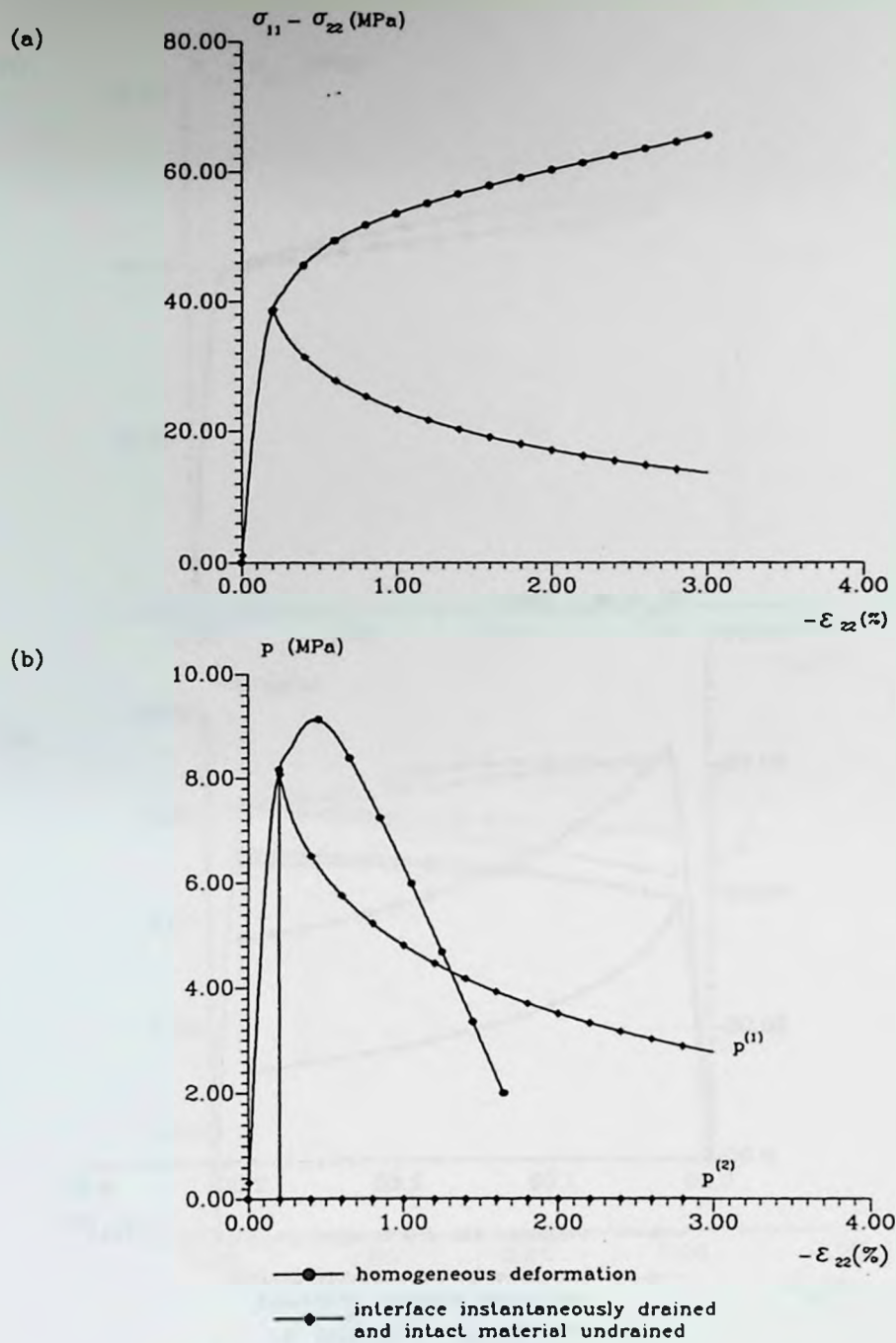


Fig. 5.3 Localized response corresponding to drained condition in the interface (a) deviatoric characteristics; (b) evolution of excess pore pressure.

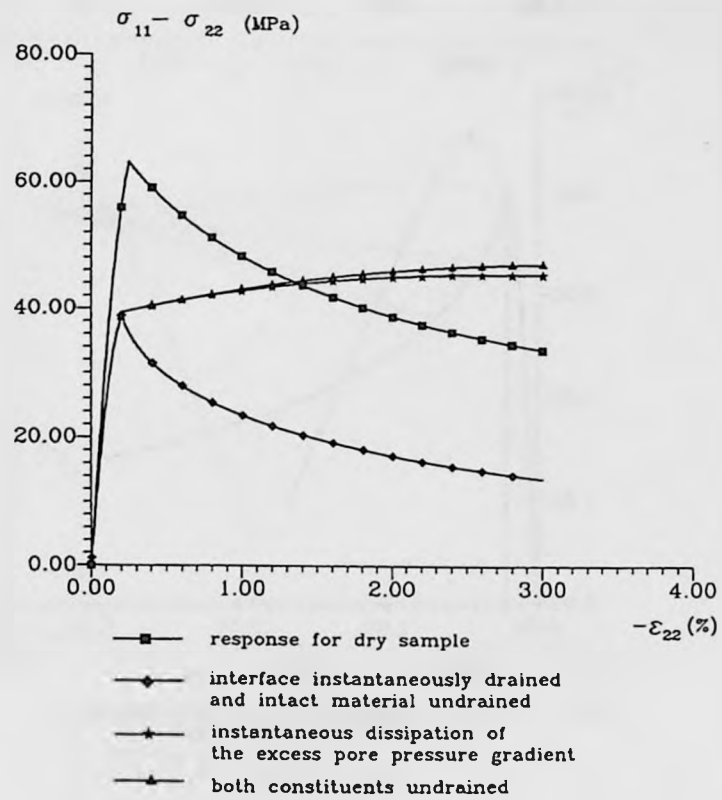


Fig. 5.4 Comparison of deviatoric characteristics for both saturated and dry samples

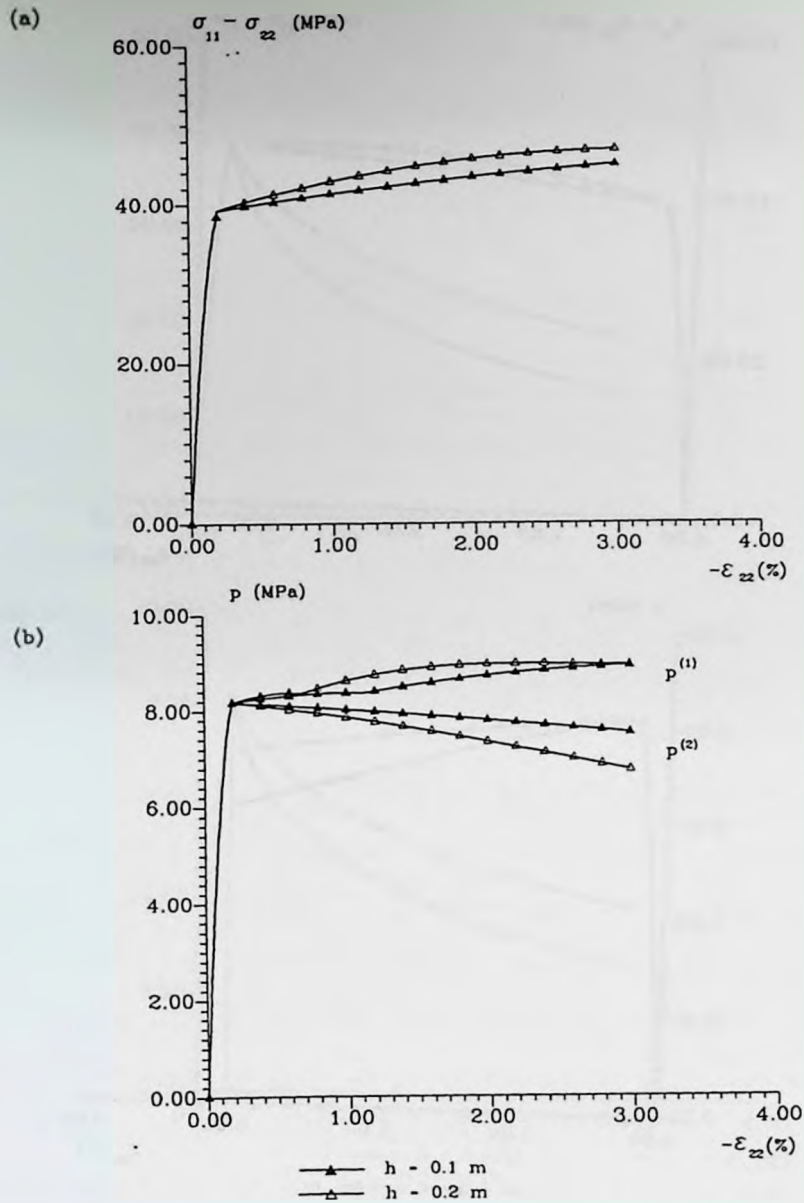


Fig. 5.5 The influence of the height of the sample on the mechanical response ( $C_d=0$ ) (a) deviatoric characteristics;  
(b) evolution of excess pore pressure.

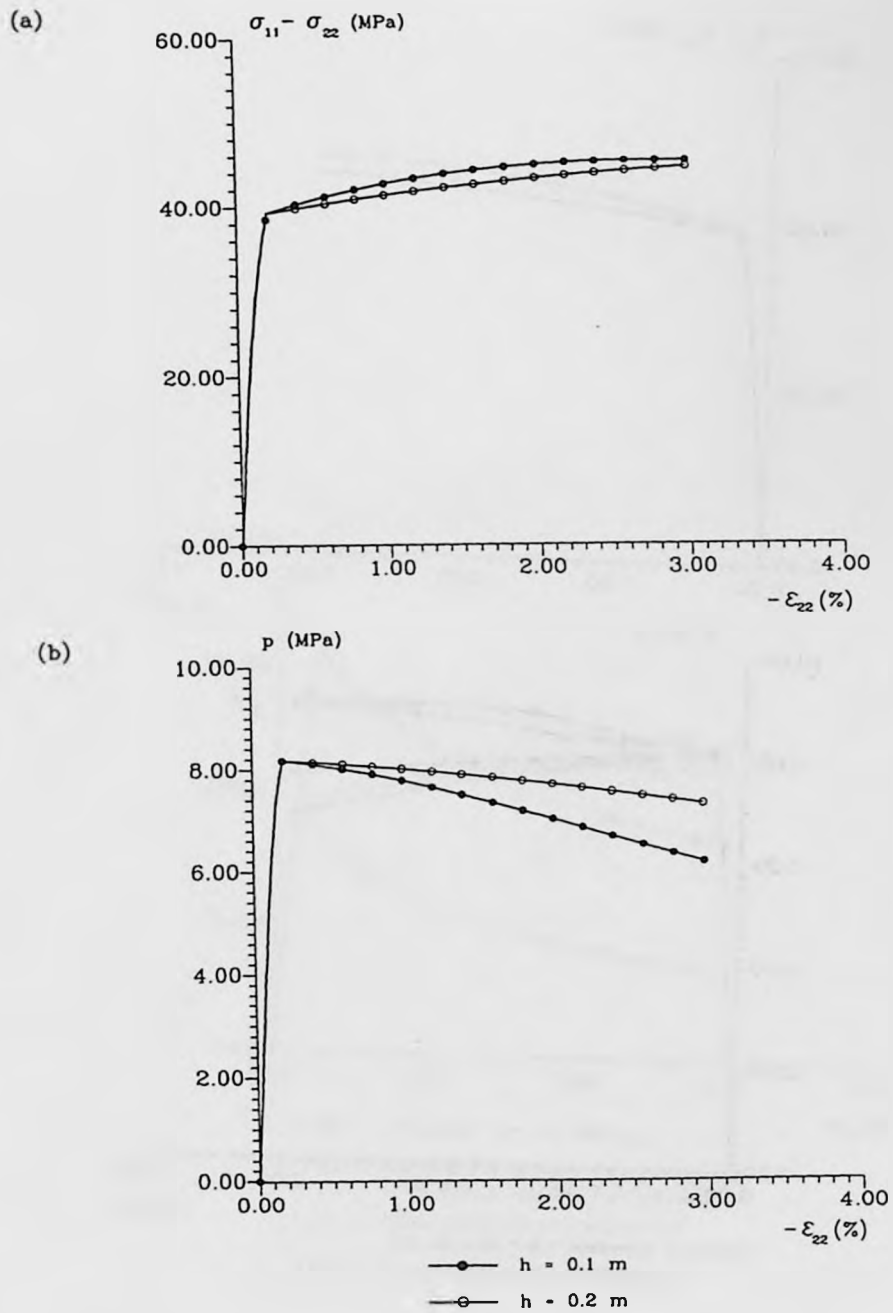


Fig. 5.6 The influence of the height of the sample on mechanical response ( $C_d \rightarrow \infty$ ) (a) deviatoric characteristics;  
(b) evolution of excess pore pressure.

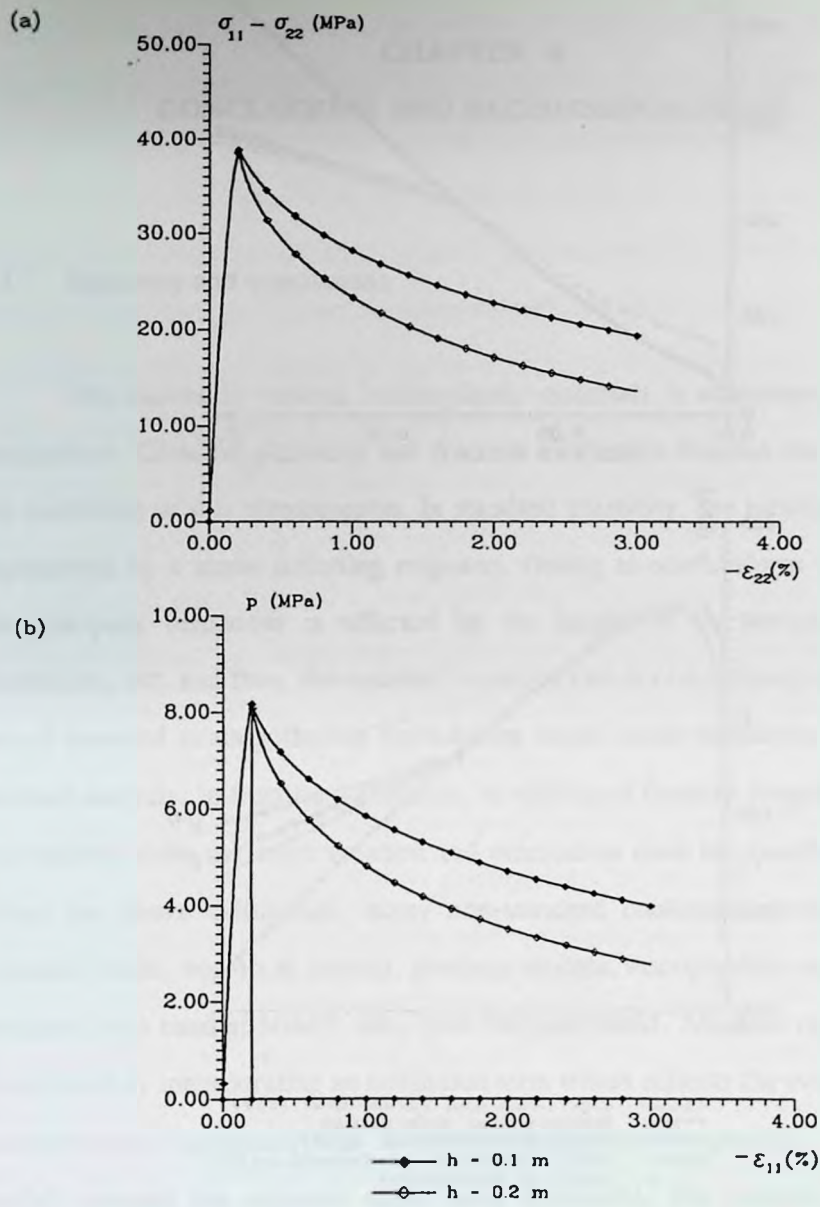


Fig. 5.7 Influence of the height of the sample on mechanical response corresponding to drained condition in the interface (a) deviatoric characteristics; (b) evolution of excess pore pressure.

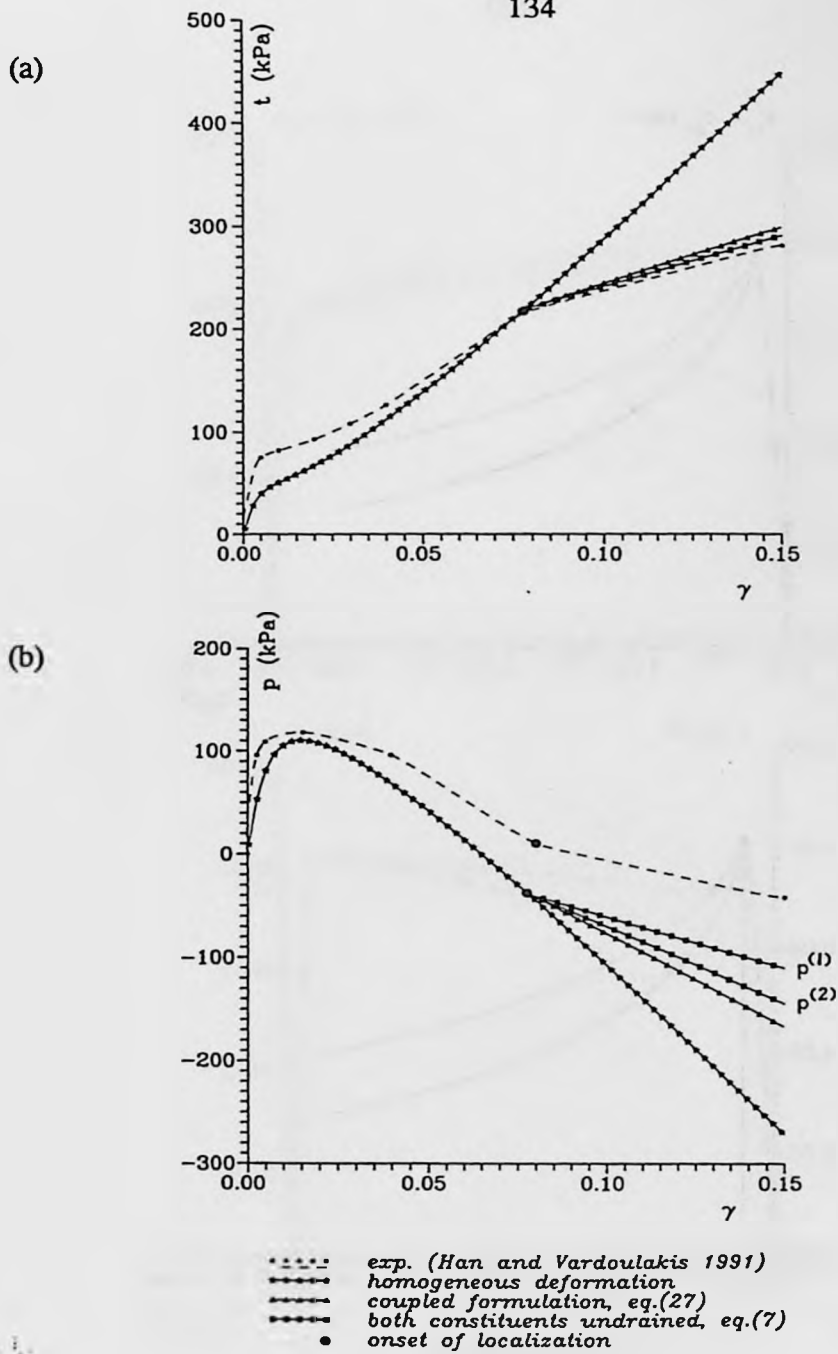


Fig. 5.8 The undrained characteristics of a cohesionless granular soil in the presence of shear band (after Pietruszczak 1995)  
 (a) deviatoric characteristics;  
 (b) evolution of excess pore pressure.

## CHAPTER 6

### CONCLUSIONS AND RECOMMENDATIONS

#### 6.1 Summary and conclusions

The failure in various brittle-plastic materials is associated with strain localization. Classical plasticity and fracture mechanics theories are not suitable for modelling of this phenomenon. In standard plasticity, the localized failure is represented by a strain-softening response. Owing to non-uniform deformation, the post-peak behaviour is affected by the height of the sample, boundary constraints, etc. and thus, the material functions can not be uniquely defined. The use of standard strain-softening formulation causes mesh-sensitivity in the finite element analysis. In fracture mechanics, modelling of fracture propagation is also not realistic since the crack location and orientation must be specified, *a priori*. Given the above difficulties, many non-standard continuum models, such as Cosserat media, non-local models, gradient models, viscoplasticity regularization, smeared shear band approach, etc., have been proposed. All these approaches are formulated by incorporating an additional term which reflects the evolution of the microstructure associated with the localized damage. In general, in all these models (except the smeared shear band approach), the material parameters associated with localized damage cannot be measured or derived from the elementary tests. In the smeared shear band approach, the formulation is based

on by estimating the average mechanical properties of a medium intercepted by a shear band. Therefore, the mechanical response of the homogenized system is a function of properties of the constituents (matrix and interface), which can be determined from experiments.

This thesis has dealt with numerical analysis of strain localization in cemented aggregate mixtures. The emphasis in this study has been placed on investigating the fracture characteristics of concrete and establishing a constitutive model for the description of strain localization. The model was implemented in the finite element algorithm to solve a number of boundary-valued problems involving both compression-shear and tension-shear as predominant failure modes. Finally, a mathematical formulation based on the homogenization technique was derived for description of the localized deformation in saturated cemented materials.

The objective of the first part of this study was to employ the bifurcation criterion for the detection of the inception of the localized mode and to establish a framework for the description of homogeneous and localized deformation process. For distributed damage, the non-associated strain hardening plasticity framework was employed. The localized damage was introduced into the constitutive law via a homogenization technique. The standard formulation was derived by estimating the average mechanical properties of the medium intercepted by a strain localization zone (shear band). The mechanical response was shown to depend on the properties of the constituents (matrix and interface) and the respective volume fractions. An alternative formulation, which is more appropriate for numerical integration (especially under complex loading

conditions) was also proposed. A constitutive model for the interface has also been developed incorporating degradation of both asperities orientation and cohesion. The homogenization technique was then employed to study the post-peak response. The latter proved to be quite sensitive to the geometry of the sample. In particular, the average rate of strain softening was shown to progressively increase with the height of the sample. The deformation mode, as observed macroscopically, remained strongly anisotropic, i.e., the reduction of vertical stress was accompanied by a significant distortion. Based on these studies, it is evident that the present framework can describe the basic characteristics of localized response.

The second part of this study was aimed at implementing the proposed constitutive model in a finite element algorithm for the analysis of compression-shear and tension-shear fracture of concrete. The main features of the implementation procedure have been discussed. The studies on mesh-sensitivity have been performed including a one-dimensional formulation and two-dimensional numerical analyses. In particular, a series of problems involving specimens with initial imperfections were analyzed. The results proved to be virtually independent of the discretization. Furthermore, the compression-shear fracture analyses of concrete structures with different geometries and boundary conditions were carried out. In tension-shear analysis, the edge-notched specimens subjected to tension and three-point bending were analyzed. The results of the simulations were consistent with the experimental observations, addressing the failure mechanism and the size effect.

The third part of this study was aimed at extending the proposed

framework to describe localization phenomenon in saturated cemented materials. The non-homogeneous deformation process was assumed to be coupled with the generation of pore pressure gradient, which prompted a transient fluid flow under the global constraint of undrained response. The formulation was derived by combining constitutive relations for the matrix and the interface, mass conservation and the equations describing the transient fluid flow. This formulation was then used to demonstrate that the onset of localization affects the deformation gradient as well as the rate of pore pressure generation and that the kinematic constraint of undrained deformation ensures that global characteristics remain stable (strain hardening).

On the basis of this study, the following major conclusions can be restated:

- Concrete fracture invokes three different failure modes. (a) tensile fracture, which is characterized by a single fracture plane perpendicular to the tensile direction; (b) distributed fracture in regions near compressive meridian; (c) localized shear mode for a specimen failing under the formation of an inclined fracture surface. With increasing confinement, there exists a brittle-ductile transition. The mechanical response associated with localized deformation should be regarded as a structural property.
- Classical plasticity theory is not appropriate for concrete fracture analysis. The material parameters cannot be uniquely defined and the numerical analysis suffers from spurious mesh sensitivity.

- The constitutive model developed in the present study was based on a homogenization technique. This approach has several advantages over other non-standard formulations which include the following: (i) all material parameters and functions can be determined from elementary tests; (ii) the framework can be implemented in finite element algorithms using standard plasticity procedures for deriving the tangent operator; and (iii) the analysis of different fracture modes can be performed within the same conceptual framework.

## 6.2 Recommendations for future research

In the present research, some fundamental aspects for localization analysis based on a homogenization technique have been studied. Although the proposed approach shows great potential to be applied in practice, further research is still required to verify its performance, especially for structures under complex loading and boundary conditions. In the following, some recommendations for future research are given based on the present study.

- (1) An experimental study is required for investigating the transition from the homogeneous to localized mode as well as the response involving localized deformation itself, in order to verify the validity of the bifurcation criterion and the performance of homogenization technique.
- (2) The analysis could be extended to reinforced concrete structures. This requires an experimental investigation and numerical modelling of the

bond-slip behaviour. The latter could be modelled by either the smeared or the discrete interface approach.

- (3) In order to consider complex loading histories, such as cyclic loading, creep, thermal loading, etc., an appropriate extension of the proposed formulation is required.
- (4) In order to analyze localization phenomenon in saturated cemented media, an experimental study is required. The proposed framework could be eventually extended to include a coupled formulation for the description of transient flow.

The above recommendations, together with several other points suggested throughout this study, appear to be a logical continuation of the present research. Upon completion of these studies, the proposed theory may provide an efficient tool for failure analysis of a variety of structures.

**APPENDIX A**  
**COMPUTATION OF THE ORIENTATION**  
**OF DISCONTINUITY PLANE**

In numerical terms, the necessary condition for localization reduces to a constrained minimization problem for  $f(n_i) = \det B_{jk}$  under  $n_i n_i = 1$ . In two dimensions,  $\det B_{jk}$  can be written explicitly as

$$\det B_{jk} = a_0 n_1^4 + a_1 n_1^3 n_2 + a_2 n_1^2 n_2^2 + a_3 n_1 n_2^3 + a_4 n_2^4 \quad (A1)$$

where  $a_0 = D_{1111} D_{1212} - D_{1112} D_{1211}$

$$a_1 = D_{1111} D_{1222} + D_{1111} D_{2212} - D_{1112} D_{2211} - D_{1122} D_{1211}$$

$$a_2 = D_{1111} D_{2222} + D_{1112} D_{1222} + D_{1211} D_{2212} - D_{1122} D_{1212} - D_{1122} D_{2211} - D_{1212} D_{2211}$$

$$a_3 = D_{1112} D_{2222} + D_{1211} D_{2222} - D_{1122} D_{2212} - D_{1222} D_{2211}$$

$$a_4 = D_{1212} D_{2222} - D_{2212} D_{1222}$$

and  $D_{ijkl}$  is the constitutive tensor governing the homogeneous deformation. If the constitutive relation is expressed in the matrix form  $\dot{\sigma} = [D]\dot{\epsilon}$ , then

$$a_0 = D_{11} D_{44} - D_{14} D_{41}$$

$$a_1 = D_{11} D_{24} + D_{11} D_{42} - D_{12} D_{41} - D_{21} D_{14}$$

$$a_2 = D_{11} D_{22} + D_{14} D_{42} + D_{41} D_{24} - D_{12} D_{21} - D_{12} D_{44} - D_{21} D_{44}$$

$$a_3 = D_{14} D_{22} + D_{41} D_{22} - D_{42} D_{21} - D_{24} D_{12}$$

$$a_4 = D_{44} D_{22} - D_{24} D_{42}$$

The minima of  $f(n_i)$  may be computed by letting  $n_1 = \cos \beta$ ;  $n_2 = \sin \beta$ , where  $\beta$  is the orientation of discontinuity plane.

**APPENDIX B**  
**FORMULATION OF MATRICES [S<sub>1</sub>] AND [S<sub>2</sub>]**

Assume that both constituents involved, i.e. the matrix (1) and the interface (2) represent elastoplastic media and their mechanical response can be defined by incremental relations

$$\dot{\sigma}^{(1)} = [D] \dot{\epsilon}^{(1)} \quad ; \quad \dot{\sigma}^{(2)} = [K] \dot{g} \quad (\text{B1})$$

Consider the equilibrium constraints

$$\dot{\sigma}_{11} = \dot{\sigma}_{11}^{(1)} = \dot{\sigma}_{11}^{(2)} \quad ; \quad \dot{\sigma}_{12} = \dot{\sigma}_{12}^{(1)} = \dot{\sigma}_{12}^{(2)} \quad (\text{B2})$$

The substitution of eq.(B1) in eq.(B2) results, after some algebraic manipulations, in

$$[\delta] \dot{\epsilon}^{(1)} = [A] \dot{\epsilon} + [B] \dot{g} \quad (\text{B3})$$

where the matrices [A] and [B] are defined as

$$[A] = \begin{bmatrix} -D_{21}/C_1 & K_{11}/(\mu_1 C_1) & -D_{24}/C_1 \\ -D_{41}/C_2 & -D_{42}/C_2 & K_{22}/(\mu C_2) \end{bmatrix} \quad (\text{B4})$$

$$[B] = \begin{bmatrix} 0 & (K_{12} + \mu D_{24})/C_1 \\ (K_{21} + \mu D_{42})/C_2 & 0 \end{bmatrix}$$

with  $C_1 = D_{22} + K_{11}/\mu$  and  $C_2 = D_{44} + K_{22}/\mu$ .

The strain decomposition may be written as,

$$[\delta]\dot{\epsilon} = [\delta]\dot{\epsilon}^{(1)} + \mu\dot{g} \quad (\text{B5})$$

Solving now the set of simultaneous equations (B4) and (B5), one obtains

$$[\delta]\dot{\epsilon}^{(1)} = [S]\dot{\epsilon} ; [S] = ([I] + \frac{1}{\mu}[B])^{-1}([A] + \frac{1}{\mu}[B][\delta]) \quad (\text{B6})$$

and  $[I]$  is a (2x2) unit matrix.

However, taking into account the identity  $\dot{\epsilon}_{11} = \dot{\epsilon}_{11}^{(1)}$  (kinematic constraint), the average strain rates in the matrix can be directly defined in terms of  $\epsilon$ ,

$$\dot{\epsilon}^{(1)} = [S_1]\dot{\epsilon} ; [S_1] = \begin{bmatrix} 1 & 0 & 0 \\ S_{11} & S_{12} & S_{13} \\ S_{21} & S_{22} & S_{23} \end{bmatrix} \quad (\text{B7})$$

The components of the velocity discontinuity  $\dot{g}$  can also be expressed in a functional form similar to the preceding equation. Writing

$$\dot{g} = [S_2]\dot{\epsilon} \quad (\text{B8})$$

and combining this with eqs (B6) and (B7), one obtains

$$[S_2] = \frac{1}{\mu}([[\delta]] - [S_1]) \quad (\text{B9})$$

Note that under undrained conditions, (B1) is replaced by

$$\dot{\sigma}^{(1)} = [ \bar{D} ] \dot{\epsilon}^{(1)} \quad ; \quad \dot{\sigma}^{(2)} = [ \bar{K} ] \dot{g}^{(1)} \quad (\text{B10})$$

with  $[\bar{D}]$  and  $[\bar{K}]$  are defined in section 5.3. In this case the problem is formulated in terms of  $[\bar{S}_1]$  and  $[\bar{S}_2]$  which are identical to  $[S_1]$  and  $[S_2]$  provided the drained moduli are replaced by their undrained counterparts.

## APPENDIX C

### TRANSFORMATION MATRICES

Using the vector representation, the transformation law for stress takes the form

$$\sigma = [T]\sigma^* \quad (C1)$$

where  $\sigma = \{\sigma_x, \sigma_y, \sigma_{xy}, \sigma_z\}^T$ ,  $\sigma^* = \{\sigma_t, \sigma_n, \sigma_{nt}, \sigma_s\}^T$ ,  $[T]$  represents the transformation matrix ( $c = \cos \beta$ ,  $s = \sin \beta$ ).

$$[T] = \begin{bmatrix} c^2 & s^2 & -2cs & 0 \\ s^2 & c^2 & 2cs & 0 \\ cs & -cs & (c^2 - s^2) & 0 \\ 0 & 0 & 0 & 1 \end{bmatrix} \quad (C2)$$

A similar rule can be used to define the transformation of strain rate vector, i.e.

$$\dot{\epsilon}^* = [T]^T \dot{\epsilon} \quad (C3)$$

where  $\epsilon = \{\epsilon_x, \epsilon_y, \gamma_{xy}, \epsilon_z\}^T$ ,  $\epsilon^* = \{\epsilon_t, \epsilon_n, \gamma_{nt}, \epsilon_s\}^T$ .

The transformation matrix  $[N]$  appearing in eq.(2.26) is defined as

$$[N] = \begin{bmatrix} s^2 & c^2 & 2cs \\ cs & -cs & (c^2 - s^2) \end{bmatrix} \quad (C4)$$

**APPENDIX D**  
**CONSTITUTIVE RELATION FOR THE MATRIX IN THE**  
**COUPLED FORMULATION(SECTION 5.4.3)**

Based on the stress decomposition eq.(5.4), the constitutive relation for the matrix is defined as

$$[\sigma'_{ij} - (1-n)p_w \delta_{ij}] = D_{ijkl} \dot{\epsilon}_{kl} \quad (D1)$$

Eq.(D1) should be supplemented by the expression for pore pressure generation

$$\dot{p}_w = \frac{K_w}{n} (\dot{\epsilon}_{ii}^{(1)} + \mu \dot{g}_2) \quad (D2)$$

where  $K_w$  is the bulk modulus and the index w refers to the water phase. Consider the solid matrix to be an elastoplastic material for which the yield and plastic potential functions are of the form

$$f(\sigma'_{ij}, k) = 0 \quad ; \quad Q(\sigma'_{ij}) = 0 \rightarrow \dot{\epsilon}^p_{ij} = \dot{\lambda} \frac{\partial Q}{\partial \sigma'_{ij}} \quad (D3)$$

where  $k = k(\epsilon^p_{ij})$  is a hardening parameter. The consistency condition reads

$$\dot{f} = \frac{\partial f}{\partial \sigma'_{ij}} \dot{\sigma}'_{ij} + H_p \dot{\lambda} = 0 \quad ; \quad H_p = \frac{\partial f}{\partial k} \frac{\partial k}{\partial \epsilon^p_{ij}} \frac{\partial Q}{\partial \sigma'_{ij}} \quad (D4)$$

with  $H_p$  representing the plastic hardening modulus. It is convenient now to express the constitutive relation eq.(D1) in the form

$$(\sigma'_{ij} - (1-n)p_w \delta_{ij})' = D_{ijkl}^e (\dot{\epsilon}_{kl} - \dot{\epsilon}_{ij}^p) \quad (D5)$$

where  $D_{ijkl}^e$  describes the elastic properties under drained conditions.

Differentiating the left-hand side of eq.(D5) and substituting eq.(D2) results in

$$\dot{\sigma}'_{ij} - (1-n)C_{ijkl} \dot{\epsilon}_{kl} - (1-n)\dot{C}_{ij} \mu \dot{g}_2 = D_{ijkl}^e (\dot{\epsilon}_{kl} - \dot{\epsilon}_{ij}^p) ; C_{ijkl} = \frac{K_w}{n} \delta_{ij} \delta_{kl} , \dot{C}_{ij} = \frac{K_w}{n} \dot{\delta}_{ij} \quad (D6)$$

It should be noted that in arriving at eq.(D6) the term  $\dot{n}p_w$  has been neglected as small compared to  $\dot{n}p_w$ . Substituting now eq.(D6) in the consistency conditions eq.(D4) leads to

$$\dot{\lambda} = \frac{[\frac{\partial f}{\partial \sigma'_{ij}} (1-n)C_{ijkl} + \frac{\partial f}{\partial \sigma'_{ij}} D_{ijkl}^e] \dot{\epsilon}_{kl} + \frac{\partial f}{\partial \sigma'_{ij}} (1-n)\dot{C}_{ij} \mu \dot{g}_2}{H_e + H_p} ; H_e = \frac{\partial f}{\partial \sigma'_{ij}} D_{ijkl}^e \frac{\partial Q}{\partial \sigma'_{ij}} \quad (D7)$$

Thus, given eq.(D7) and the flow rule eq.(D3), one can write

$$\dot{\sigma}'_{ij} = [D_{ijkl} + (1-n)C_{ijkl}] \dot{\epsilon}_{kl} + [\dot{D}_{ij} + (1-n)\dot{C}_{ij}] \dot{\xi}_2$$

$$D_{ijkl} = D_{ijkl}^e - \frac{D_{ijpq}^e \frac{\partial Q}{\partial \sigma'_{pq}} \left[ \frac{\partial f}{\partial \sigma'_{rs}} (1-n) C_{rskl} + \frac{\partial f}{\partial \sigma'_{rs}} D_{rskl}^e \right]}{H_e + H_p} \quad (\text{E8})$$

$$\dot{D}_{ij} = - \frac{D_{ijpq}^e \frac{\partial Q}{\partial \sigma'_{pq}} \frac{\partial f}{\partial \sigma'_{rs}} (1-n) \mu \dot{C}_{rs}}{H_e + H_p}$$

Finally, differentiating eq.(D3) and neglecting again the term  $\dot{n} p_w$  gives

$$\dot{\sigma}_{ij} = \bar{D}_{ijkl} \dot{\epsilon}_{kl} + G_{ij} \dot{\xi}_2 = (D_{ijkl} + C_{ijkl}) \dot{\epsilon}_{kl} + (\dot{D}_{ij} + \dot{C}_{ij}) \dot{\xi}_2 \quad (\text{D9})$$

Eq.(D9) represents the relation between the total stress and strain rates for the matrix in the deformation process constrained by  $p_w^{(1)} = p_w^{(2)} = p_w$ .

**APPENDIX E**  
**DEFINITION OF MATRICES  $[\tilde{S}_1]$  AND  $[\tilde{S}_2]$**

Consider again the deformation coupled with dissipation of the differential pressure gradient, i.e.  $p_w^{(1)} = p_w^{(2)} = p_w$  (section 5.4). Assume that the response of the matrix (1) and the interface material (2) can be defined by incremental relations

$$\dot{\sigma}^{(1)} = [\bar{D}] \dot{\epsilon}^{(1)} + [G] \dot{g} \quad ; \quad \dot{\sigma}^{(2)} = [\bar{K}] \dot{g}^{(1)} + [\hat{K}] \dot{\epsilon}_{ii} \quad (E1)$$

where  $[\hat{G}]$  and  $[\hat{K}]$  are defined in eqs.(D6) and (5.45), respectively. Impose the equilibrium constraints

$$\dot{\sigma}_{11} = \dot{\sigma}_{11}^{(1)} = \dot{\sigma}_{11}^{(2)} \quad ; \quad \dot{\sigma}_{12} = \dot{\sigma}_{12}^{(1)} = \dot{\sigma}_{12}^{(2)} \quad (E2)$$

The substitution of eq. (E1) in eq.(E2) results, after some algebraic manipulations, in

$$[\delta] \dot{\epsilon}^{(1)} = [\hat{A}] \dot{\epsilon} + [\hat{B}] \dot{g} \quad (E3)$$

where the matrices  $[\hat{A}]$  and  $[\hat{B}]$  are defined as

$$\begin{aligned}
 [\bar{A}] &= \begin{bmatrix} -\bar{D}_{21}/\bar{C}_1 & \bar{K}_{11}/(\mu_1\bar{C}_1) & -\bar{D}_{41}/\bar{C}_1 \\ -\bar{D}_{41}/\bar{C}_2 & -\bar{D}_{42}/\bar{C}_2 & \bar{K}_{22}/(\mu\bar{C}_2) \end{bmatrix} \\
 [\bar{B}] &= \begin{bmatrix} 0 & (\bar{K}_{12} + \mu\bar{D}_{24})/\bar{C}_1 \\ (\bar{K}_{21} + \mu\bar{D}_{42})/\bar{C}_2 \end{bmatrix}
 \end{aligned} \tag{E4}$$

with  $\tilde{C}_1 = \bar{D}_{22} + \bar{K}_{11}/\mu$ ;  $\tilde{C}_2 = \bar{D}_{44} + \bar{K}_{22}/\mu$ ;  $\tilde{D}_{21} = \bar{D}_{21} - K_w/n$ ;  $\tilde{D}_{22} = \bar{D}_{22} - K_w/n$ ;  $\tilde{K}_{11} = \bar{K}_{11} - K_w/n - G_2$  and  $\tilde{K}_{21} = \bar{K}_{21} - G_4$ .

The strain decomposition, takes the form

$$[\delta]\dot{\epsilon} = [\delta]\dot{\epsilon}^{(1)} + \mu\dot{g} \tag{E5}$$

Solving now the set of simultaneous equations (E4) and (E5), one obtains

$$[\delta]\dot{\epsilon}^{(1)} = [\mathcal{S}]\dot{\epsilon} ; [\mathcal{S}] = ([\Gamma] + \frac{1}{\mu}[\bar{B}])^{-1}([\bar{A}] + \frac{1}{\mu}[\bar{B}][\delta]) \tag{E6}$$

and  $[\Gamma]$  is a (2x2) unit matrix. Thus, taking into account the identity  $\dot{\epsilon}_{11} = \dot{\epsilon}_{11}^{(1)}$  (kinematic constraint), the average strain rates in the matrix can be directly defined in terms of  $\dot{\epsilon}$ ,

$$\dot{\epsilon}^{(1)} = [\mathcal{S}_1]\dot{\epsilon} ; [\mathcal{S}_1] = \begin{bmatrix} 1 & 0 & 0 \\ \mathcal{S}_{11} & \mathcal{S}_{12} & \mathcal{S}_{13} \\ \mathcal{S}_{21} & \mathcal{S}_{22} & \mathcal{S}_{23} \end{bmatrix} \tag{E7}$$

Whereas the components of the velocity discontinuity  $\dot{g}$  can be expressed

$$\dot{g} = [S_2] \dot{\epsilon} \quad ; \quad [S_2] = \frac{1}{\mu} ([\delta] - [S_1]) \quad (E8)$$

## BIBLIOGRAPHY

- Bathe, K.J.(1982), *Finite Element Procedures in Engineering Analysis*, Prentice-Hall, Englewood Cliffs, New Jersey.
- Bazant, Z.P. and Oh, B.H.(1983), Crack band theory for fracture of concrete, *RILEM Materials and Structures*, **16**, 155-177.
- Bazant, Z.P. and Pfeiffer, P.A.(1987), Determination of fracture energy from size effect and brittleness number, *ACI Materials Journal*, 463-480.
- Bazant, Z.P. and Pijaudier-Cabot, G.(1988), Non-local continuum damage, localization instability and convergence, *Journ. Appl. Mech.* **55**, 287-293.
- Bazant, Z.P.(1989), Stable states and stable paths of propagation of damage zones and interactive fractures, in: *Crack and Damage: Strain Localization and Size Effect*, Eds. J. Mazars and Z.P. Bazant, 183-206.
- Belytschko S., Fish J. and Englemann B.E.(1988), A finite element with embedded localization zones, *Comp. Meth. in Appl. Mech. & Eng.*, **70**, 59-89.
- Borja, R.I. and Lee, S.R.(1990), Cam-clay plasticity, Part I: Implicit integration of elastoplastic constitutive relations, *Comp. Meth. Appl. Mech. Eng.*, **78**, 49-72.
- Borja, R.I. (1991), Cam-clay plasticity, Part I: Implicit integration of constitutive relation based on a non-linear elastic stress predictor, *Comp. Meth. Appl. Mech. Eng.*, **88**, 225-240.
- Chen, W.F.(1988), *Plasticity for Structure Engineers*, McGraw-Hill.
- Chen, Z. and Schreyer, H.L. (1990), A numerical solution scheme for softening

problems involving total strain control, *Computers & Structures*, **37**, 1043-1050.

Cornelissen, H.A.W., Hordijk, D.A. and Reinhardt, H.W.(1986), Experiments and theory for the application of fracture mechanics to normal and lightweight concrete, in: *Fracture Toughness and Fracture Energy*, ed. F.H.Wittmann, Elsevier, 565-575.

Crisfield, M.A.(1983), An arc-length method including line search and accelerations, *Int. Journ. Num. Meth. Eng.*, **19**, 1269-1289.

de Borst, R.(1987), Computation of post-bifurcation and post-failure behaviour of strain-softening solids, *Comput. and Struct.*, **25**, 211-224.

de Borst, R.(1991), Simulation of strain localization: A reappraisal of the Cosserat continuum, *Eng. Comput.*, **8**, 317-332.

de Borst, R. and Muhlhaus H.B.(1992), Gradient-dependent plasticity: formulation and algorithmic aspects, *Int. Journ. Num. Meth. Eng.*, **35**, 521-539.

de Borst, R.(1993), A generalization of  $J_2$  -flow theory for polar continua, *Comp. Meth. Appl.Mech. Eng.*, **103**, 347-362.

Dowding C.H., Zubelewicz A., O'Connor K.M. and Belytschko T.B.(1991), Explicit modelling of dilation, asperity degradation and cyclic seating of rock joints, *Computers and Geotechnics*, **11**, 209-228.

Dvorak, G.J. and Bahei-El-Din, Y.A.(1982), Plasticity analysis of fibrous composites, *Journ. Appl. Mech.*, **49**, 327-335.

Gopalaratnam, V.S. and Shah, S.P.(1985), Softening response of plain concrete in direct tension, *ACI Journal*, **82**(3), 310-324.

Han, C. and Vardoulakis, I. (1991), Plane-strain compression experiments on water saturated fine-grained sand, *Geotechnique*, **41**, 49-78

Hill, R. (1958), A general theory of uniqueness and stability in elastic-plastic

solids, *Journ. Mech. Phys. Solids*, **6**, 236-252.

Hill, R. (1963), Elastic properties of reinforced solids: some theoretical principles, *Journ. Mech. Phys. Solids*, **11**, 357-372.

Hordijk, D.A., Reinhardt, H.W. and Cornelissen, H.A.W. (1987), Fracture mechanics parameters of concrete from uniaxial tensile tests as influenced by specimen length, in: *Fracture of Concrete and Rock, RILEM-SEM Int. Conf.*, Houston(ed. S.P.Shah and S.E.Swartz), 138-149.

Horri, H., Shi, Z. and Gong, S.(1989), Models of fracture process zone in concrete, rock and ceramics, in: *Crack and Damage: Strain Localization and Size Effect*, Eds. J. Mazars and Z.P. Bazant, 104-115.

Jaeger, J.C. and Cook, N.G.W.(1976), *Fundamentals of Rock Mechanics*, Chapman & Hall, London.

Jamet, P., Millard, A. and Nahas, G.(1984), Triaxial behaviour of a microconcrete complete stress-strain curves for confining pressures ranging from 0 to 100MPa, in: *RILEM-CEB Symp. Concrete under Multiaxial Conditions*, **1** 259-266.

Jiang, J. and Pietruszczak, S. (1988), Convexity of yield loci for pressure sensitive materials, *Computers and Geotechnics*, **5**, 51-63.

Kotsovos, M.D.(1983), Effect of testing techniques on the post-ultimate behaviour of concrete under compression, *RILEM Materials and Structures*, **16(91)**, 3-12.

Krajcinovic, D.(1989), A mesomechanical model of concrete and its application to the size effect phenomenon, in: *Crack and Damage: Strain Localization and Size Effect*, Eds. J. Mazars and Z.P. Bazant, 164-180.

Lade, P.V., Nelson R.B. and Ito, Y.M. (1988), Instability of gradular materials with non-associated flow, *J. Engrg. Mechanics, ASCE*, **114**, 2173-2191.

Lade, P.V., (1994), Instability and liquefaction of granular materials, *Computers*

& *Geotechnics*, 16(2), 123-151.

Loret, B. and Prevost, J.H. (1990) , Dynamic strain localization in elasto-(visco-) plastic solids, Part 1. General formulation and one-dimensional examples", *Comp. Meth. in Appl. Mech. & Eng.*, 83, 247-273.

Loret, B. and Prevost, J.H. (1991), Dynamic strain localization in fluid-saturated porous media, *J. of Eng. Mech., ASCE*, 11, 907-922.

Mazars, J and Bazant, Z.P.(1989)(editor), *Crack and Damage: Strain Localization and Size Effect*, Elsevier.

Molenkamp, F.(1991), Material instability for drained and undrained behavior. Part 1: Shear band generation, Part 2: Combined uniform deformation and shear band generation, *Int. Journ.Num. and Anal. Meth. in Geomech.*, 15, 147-180.

Muhlhaus H.B. and Aifantis E.C.(1991), A variational principle for gradient plasticity, *Int. Journ. Solids Struct.*, 28, 845-858.

Mura, T.(1987), *Micromechanics of defects in solids*, Martinus Nijhoff Publ., Dordrecht.

Nayak, G.C. and Zienkiewicz, O.C.(1972), Elastoplastic stress analysis, A generalization for various constitutive relations including strain softening, *Int. Journ. Numer. Meth. Eng.*, 5, 75-100.

Nemat-Nasser, S. and Obata, M.(1988), A microcrack model of dilatancy in brittle materials, *Journal of Applied Mechanics*, 55, 24-35.

Needleman, A.(1988), Material rate dependence and mesh sensitivity in localization problems, *Comp. Meth. in App. mech. and Eng.*, 67, 19-85.

Ortiz, M.(1987), An analytical study of the localized failure modes of concrete, *Mechanics of Materials*, 6, 159-174.

Ortiz, M., Leroy, Y. and Needleman, A.(1987), A finite element method for

localized failure analysis, *Comput. Meth. Appl. Mech. Eng.*, **61**, 189-214.

Owen, D.R.J. and Hinton E.(1980), *Finite Element in Plasticity: Theory and Practice*, Pineridge Press Ltd., U.K..

Palaniswamy, R. and Shah, S.P.(1974), Fracture and stress-strain relationship of concrete under triaxial compression, *Journ. Struc. Div., ASCE*, **100**, 901-916.

Pastor, M., Zienkiewicz, O.C., Xu G. and Peraire J.(1992), Modelling of sand behaviour: cyclic loading, anisotropy and localization, *Modern Approaches to Plasticity*, ed. Kolymbas D. and Gudehus G., Springer Verlag.

Pastor, M., Peraire, J. and Zienkiewicz, O.C.,(1991), Adaptive remeshing for shear band localization problems, *Arch. Appl. Mech.*, **61**, 30-39.

Petersson, P.E.(1981), Crack growth and development of fracture zones in plain concrete and similar materials, *Report TVBM-1006*, Lund, Sweden.

Pietruszczak S. and Mroz Z.(1981), Finite element analysis of deformation of strain softening materials, *Int. Journ. Num. Meth. Eng.*, **17**, 327-334.

Pietruszczak S. and Stolle, D.F.E. (1985), Deformation of strain softening materials, Part I: Objectivity of finite element solutions based on conventional strain softening formulations, *Computers and Geotechnics*, **1**, 99-115.

Pietruszczak, S., Jiang, J. and Mirza, F.A.(1988), An elastoplastic constitutive model for concrete, *Int. Journ. Solids Struct.*, **24**, 705-722.

Pietruszczak, S. and Krucinski, S.(1989), Description of anisotropic response of clay using a tensorial measure of structural disorder, *Mech. Material*, **8**, 237-249.

Pietruszczak S.(1991), On the mechanics of jointed media: masonry and related problems, in: *Computer Methods and Advances in Geomechanics*, Eds. G. Beer, J.R.Booker & J.P.Carter, Balkema Publ., 403-413.

Pietruszczak S. and Niu X.(1993), On the description of localized deformation,

*Int. Journ. Num. Anal. Meth. Geomech.*, **17**, 791-805.

Pietruszczak, S. and Xu, G.(1995), Brittle response of concrete as a localization problem, *Int. Journ. Solids Struct.*, **32**, 1517-1533.

Pietruszczak, S. and Xu, G.(1995a), Description of localized deformation in saturated cemented materials, in: *Int. Symp. on Numer. Models in Geomechanics- NUMOG V*, Davos, Switzerland, 181-186.

Pietruszczak, S. & Pande, G.N.(1995), On the mechanical response of saturated cemented materials, *Int. Journ. Num. Anal. Meth. Geomech.*, **19**, 555-575.

Pietruszczak, S. (1995), On the undrained response of granular soil involving localized deformation, *Journ. Eng. Mech.*, **121**(12).

Prevost, J.H. and Loret, B. (1990), Dynamic strain localization in elasto-(visco-) plastic solids, Part 1. Plane strain examples, *Comp. Meth. in Appl. Mech. & Eng.*, **83**, 275-294.

Rice, J.R.(1975), On the stability of dilatant hardening of saturated rock mass, *J. Geophys.Res.*, **80**, 1531-1536.

Roefstra, P.E.(1989), Simulation of strain localization processes with numerical concrete, in: *Crack and Damage: Strain Localization and Size Effect*, Eds. J. Mazars and Z.P. Bazant, 79-90.

Rots, J.G.(1986), Strain-softening analysis of concrete fracture specimens, in: *Fracture Toughness & Fracture Energy*, ed. F.H. Wittmann, Elsevier, 137-148.

Rudnicki, J.W. and Rice J.R.(1975), Conditions for the localization of deformation in pressure sensitive dilatant materials, *J. Mech. Phys. Solids*, **23**, 371-394.

Rudnicki, J.W.(1982), A formulation for studying coupled deformation-pore fluid diffusion effects on localization, *ASME AMD-57 Geimechanics*, ed. S.Nemat-Nasser.

- Rudnicki, J.W.(1984), Effects of dilatant hardening on the development of concentrated shear deformation in fissured rock masses, *J. of Geoph. Research*, **89**,9259-9270.
- Sawicki A.(1983), Engineering mechanics of elastoplastic composites, *Mechanics of Materials*, **2**, 217-231.
- Schneider, H.J.(1976), The friction and deformation behaviour of rock joints, *Rock Mechanics*, **8**, 170-184.
- Thomas, T.Y.(1961), *Plastic Flow and Fracture in Solids*, Academic Press, New York.
- Vardoulakis, I (1985), Stability and bifurcation of undrained, plane rectilinear defromations on water-saturated granular soils, *Int. J. Num. and Analy. Meth. in Geomech.*, **9**, 399-414.
- Vardoulakis, I (1986), Dynamic stability of undrained simple shear on water-saturated granular soils, *Int. J. Num. Analy. Meth. in Geomech.*, **10**, 177-190.
- Schreyer, H.L. and Chen, Z.(1986), One-dimensional softening with localization, *Journ. Appl. Mech.*, **53**, 791-797.
- Van Mier, J.G.M.(1984), Strain-softening of concrete under multiaxial loading conditions, *Ph.D. Thesis*, Eindhoven University of Technology, The Netherlands.
- Van Mier, J.G.M.(1986), Fracture of concrete under complex stress, *HERON*, **31**(3).
- Van Mier, J.G.M.(1987), Fracture propagation of concrete under complex stress, in: *Fracture of ocncrete and rock, RILEM-SEM Int. Conf.*, Houston(ed. S.P.Shah and S.E.Swartz), 597-610.
- Zienkiewicz, O.C. and Taylor, R.L.(1989), *The Finite Element Methods*, 4th edition, McGraw-Hill, New York.